THE DEVELOPMENT OF MANGANESE OXIDE ELECTRODES FOR ELECTROCHEMICAL SUPERCAPACITORS

THE DEVELOPMENT OF MANGANESE OXIDE ELECTRODES FOR ELECTROCHEMICAL SUPERCAPACITORS

By

Jianmei Wei, B. Eng.

A Thesis

Submitted to the School of Graduate Studies

in Partial Fulfillment of the Requirements

For the Degree

Master of Applied Science

McMaster University

MASTER OF APPLIED SCIENCE (2007) McMaster University

(Materials Science & Engineering) Hamilton, Ontario

TITLE: The development of manganese oxide electrodes for electrochemical supercapacitors

AUTHOR: Jianmei Wei, B. Eng., (Imperial College London, UK)

SUPERVISOR: Dr. Igor Zhitomirsky

NUMBER OF PAGES: XIII, 109

ABSTRACT

Cathodic electrodeposition method has been developed for the fabrication of manganese oxide films for application in electrochemical supercapacitors (ES). The manganese oxide films prepared from $KMnO_4$ and $NaMnO_4$ aqueous solution showed an increasing deposition yield with the deposition time. The deposition rate decreases with increasing the concentration of deposition precursor. The obtained films were characterized using scanning electron microscopy (SEM), energy dispersive spectroscopy (EDS), X-ray diffraction analysis (XRD), thermogravimetric and differential thermal analysis (TGA/DTA). The SEM observations revealed uniform films of highly porous nanostructure on different substrates. The capacitive behavior of the deposits was investigated by cyclic voltammetry and chronopotentiometry method in 0.1M $NaSO_4$ aqueous solutions. As prepared deposits exhibited pseudocapacitive behavior in the potential window of 0-1.0 V versus SCE with excellent cyclability. A maximum specific capacitance (SC) of 353 F/g was obtained for the 45 $\mu g/cm^2$ film deposited from $KMnO_4$ solution on stainless steel foil, at a scan rate of 2 mV/s in the 0.1 M Na_2SO_4 solution. It was found that the SC decreased with increasing deposit thickness and scan rate. No significant effect was obtained on the films prepared from 20 mM $KMnO_4$ on stainless steel after heat treatment at various temperatures. The capacitance of as-prepared electrode did not change by changing the electrolyte from Na_2SO_4 to K_2SO_4 solutions. However, higher

capacitance values were observed by using electrolyte with higher concentration. Different structures of manganese oxides were obtained when different deposition precursors were used. No significant difference in capacitive behavior was found between the films prepared from different deposition precursor. However it was concluded that conductivity of the film is key in determining the performance of the electrodes. The effect of substrates on the electrochemical behavior has also been investigated by using stainless steel and nickel foils.

ACKNOWLEDGEMENTS

I would like to express my sincere appreciation to my supervisor, Dr. Igor Zhitomirsky for his valuable guidance and support throughout this research work. Their kind encouragement and patience are priceless to me during the course of my study in McMaster University. The financial support INCO and the Natural Science and Engineering Research Council (NSERC) is greatly acknowledged.

My appreciation is also extended to Steve Koprich for his assistance in the SEM operation and advice on sample preparation in my experiments. I am very grateful to Wen-He Gong and Frank Gibbs for their friendly assistance in the work with XRD and DTA/TGA.

Many thanks to all members of Dr. Zhitomirsky's teams and to my friends in our department, Nanda Nagarajan, Marco Cheong, Xin Pang, and Jun Cao for their kind help and friendship.

At last but not the least, special gratitude goes to my parents. Their love and encouragement greatly support my life and study.

TABLE OF CONTENTS

LIST OF FIGURES

LIST OF TABLES

1 INTRODUCTION

With the limitations of natural oil, improvement of energy storage devices has become the biggest challenge in power supply. The growing interest in electrochemical capacitors (EC) has been stimulated by their potential application as alternative energy / power sources due to the unique characteristics of the pulse-power property, the excellent reversibility and the longer cyclic life in comparison with batteries[1]. There are two main catalogues of EC depending on different energy storage principles: (1) double layer capacitors and (2) redox supercapacitors. The double layer capacitors store energy based on the charge separation at the interface of electrode and electrolyte. The energy storage in a redox supercapacitor arises from reversible Faradaic reactions in a finite layer on the surface of electrode in parallel with the double layer. Much effort has been focused on the development of electrode materials, which have high specific capacitance in various electrolytes. To realize a high capacitance, electrode materials are fabricated in a three-dimensional matrix form to achieve a high surface area. High surface carbon materials such as activated carbon, activated carbon fiber cloth, carbon aerogels, foams and nanotubes are important electrode materials for double layer capacitors. The specific capacitance (SC) of these kinds of carbon materials typically ranges from 40 to 200 F/g[1, 2]. Carbon nanotubes (CNT) are attractive materials for electrodes of ES due to their high conductivity, chemical stability, low mass density and large surface area. Nanostructured metal

oxides and hydroxides are promising materials for redox supercapacitors and exhibit high pseudocapacitance. High surface area nanostructured oxides and hydroxides of Ru, Mn, Ni, Sn, Fe exhibit significantly higher SC compared to carbon materials. The ability to achieve high specific capacitance with oxide electrode materials has generated a growing research activity in this field. There is increasing interest in the development of advanced electrode materials based on MnO_2. Manganese oxides in their various forms have received attention due to the low cost, environmentally friendly character and high SC.

2 LITERATURE REVIEW

2.1 History of supercapacitor technology

The first supercapacitor was developed by General Electric in 1957 using a porous carbon electrode and an aqueous electrolyte[3]. The energy storage arises from the charge held in the interfacial double layer between the electrode and electrolyte. Later in 1969, SOHIO also utilized the double-layer capacitance of high-area carbon materials, but in a nonaqueous solvent which provides higher operating voltage, resulting in a higher energy density[4]. A different principle was utilized and developed in 1975 onward to 1981 by Conway. The capacitance associated with the potential dependence of extents of electrochemical adsorption of H or some base metals (Pb, Bi, Cu) at Pt or Au was used as a basis for an energy-storing capacitor. Another type of

pseudocapacitor has been developed using RuO_2 films in aqueous H_2SO_4 solution, based on solid oxide redox systems[5-8]. Almost ideal capacitative behavior was obtained with large degree of reversibility between charge and discharge, about 10^5 cycles. However the Ru materials are very expensive which prevents their extensive application for large -scale supercapacitors. Therefore other metal oxides, such as manganese oxides and nickel oxides, have attracted more attention in the supercapacitor industry.

The commercial products of supercapacitors were initially designed to provide backup power for volatile computer and appliance memories. In 2001, the annual market for electrochemical capacitors was somewhat greater than $100 million[9]. Today several companies such as Maxwell Technologies, Siemens Matsushita (now EPCOS), NEC, Panasonic, ELNA, TOKIN, and several others invest in electrochemical capacitor development. Recent opportunities for the use and development of larger scale capacitors arise from the possibility of using them in hybrid configurations with secondary batteries in electric vehicle power systems[1].

2.2 Principles of energy storage

Electrical energy can be stored in two fundamentally different ways: (1) as chemical energy requiring Faradaic oxidation and reduction, such as in batteries. (2) as electrostatic energy not involving Faradaic reactions, but as negative and positive

electric charges on the plates of a capacitor[1]. The difference in principles of energy storage of batteries and EC will be discussed and compared later in this chapter.

2.2.1 Energy storage mechanisms

The electrochemical double layer capacitors (EDLC) store energy in an electrochemical double layer (Helmholtz layer) formed at the electrode/electrolyte interface, which is in the similar way as traditional capacitors. Figure 2-1 demonstrates the operating principle of a carbon capacitor. When the voltage is applied between the two electrodes, the organic electrolyte supplies and conducts the ions from one electrode to the other. During the charging process, the anions and cations are located close to the electrodes and balance the excess charge in the activated carbon. Therefore, two charged layers of opposed polarity are formed across the boundary between activated carbon and electrolyte.

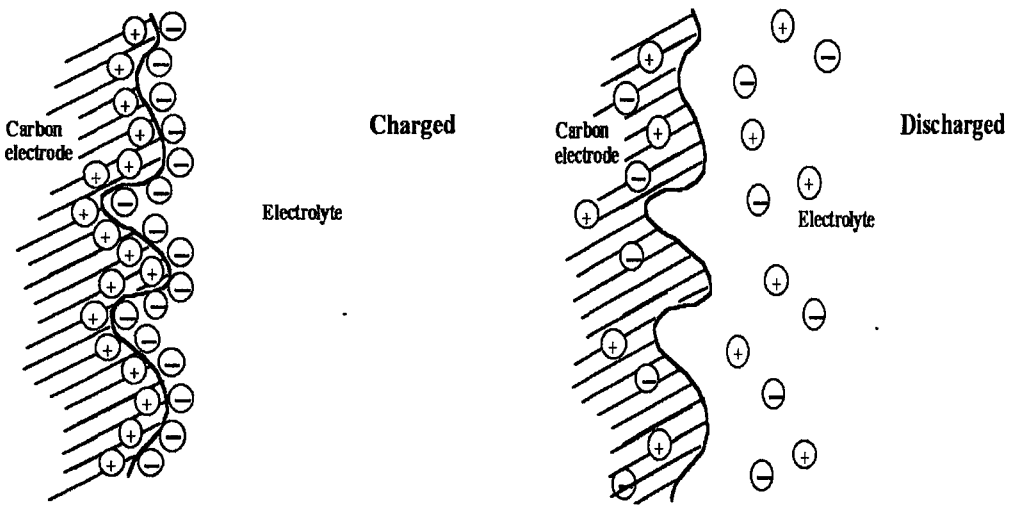

Figure 2-1 Function of carbon electrode in an electrochemical capacitor.

The double layer capacitance can be estimated according to equation (2-1).

$$C/A = \varepsilon_o^* \varepsilon_r / d \qquad (2\text{-}1)$$

assuming a relative dielectric constant ε_r of 10 for water in double layer[10]. d is the thickness of the double layer, which depends on the size of the ions and the concentration of the electrolyte. A is the corresponding surface area of the double layer. Therefore, in order to improve the capacitance value, porous electrodes with large internal effective surface can be used to provide higher surface area A. With the comparison to traditional capacitors, EDLC possesses substantially more energy (per unit mass or volume) because: (1) the thickness of the double layer containing charge separation is very small; (2) total amount of stored charge can be increased on the highly porous electrode since higher surface area is beneficial for ion exchange. Without the additional steps of charge-transfer and chemical phase change as in batteries, the mechanism of energy storage in EDLC is inherently fast and high degree of reversibility has been achieved to be in excess of 500,000 cycles[2].

During the course of development of double-layer capacitors based on high-area carbon powder or fiber materials, it has come to be recognized that some fraction of the capacitance exhibited is Faradaic pseudocapacitance component.

In redox supercapacitors, the capacitance is based on an electrochemical charge-transfer process in active materials at the surface of the electrode. The energy is stored when the oxidation state of the metal oxide is changed due to the potential change at

the electrode surface. Faradaic reactions are involved in the charging mechanism for pseudocapacitors. Such capacitance can be 10 to 100 times the double-layer capacitance of the same electrode area since the ions / cations actually diffuse into the surface of the electrode rather than forming a double layer on the surface. Transition metal oxides are usually used for the pseudocapacitor applications. The factors that will influence the performance include the particle size, surface area, porosity, conductivity of active material, nature of electrolyte and cell design. Given that charge storage is based on the redox reaction, this type of supercapacitor is somewhat battery-like in its behavior. However, the redox reaction is only restricted in a very thin layer on the electrode surface, which gives the advantage of fast charge/discharge rate, good reversibility and longer lifetime of pseudocapacitors, compared with batteries.

2.2.2 Power density and energy density

Energy density and power density are two very important parameters for energy storage devices. Energy density describes the ability of energy storage of a supercapacitor while power density describes how fast the stored energy can be released. Figure 2-2 is a typical 'Ragone plot' of different energy storage and conversion devices, representing the promising properties of electrochemical capacitors[2]. As can be seen from the graph, both batteries and fuel cells are low power

density devices whereas conventional capacitors may have a high power density at very low energy density The electrochemical supercapacitors fill in the gap between batteries and conventional capacitors. Thus with the combination of supercapacitors, the performance of batteries and fuel cells can be substantially improved in terms of power density

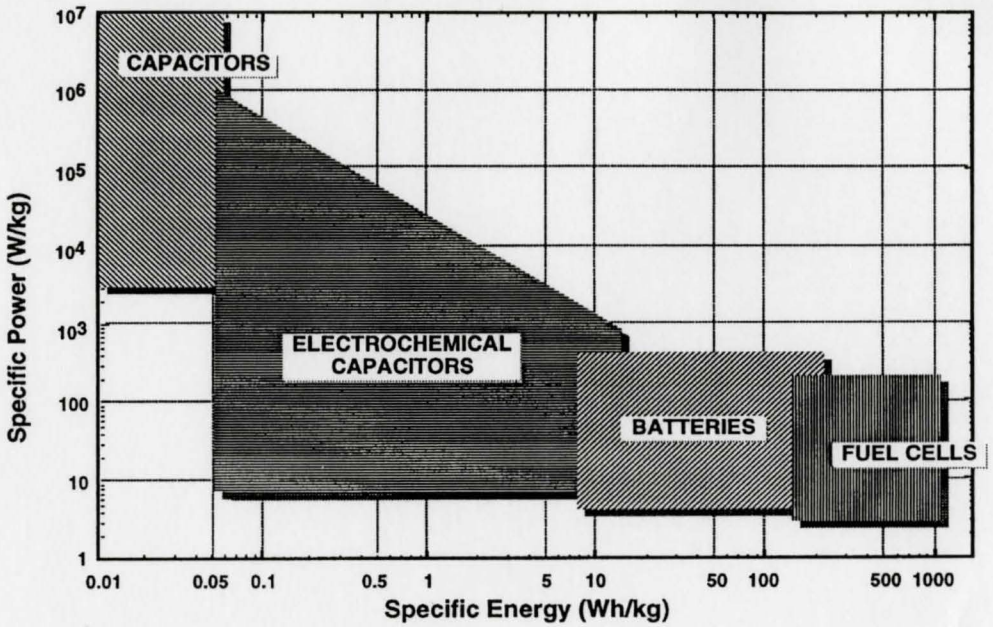

Figure 2-2 Sketch of Ragone plot for various energy storage and conversion devices. The indicated areas are rough guide lines

The energy density and power density can be calculated as below

$$W = 1/2\ CV^2 \qquad (2\text{-}2)$$

$$P = V^2/4R \qquad (2\text{-}3)$$

Where C is the specific capacitance, V is the voltage, and R is the equivalent series resistance. The energy densities of supercapacitors are usually substantially smaller than those of batteries, but this disadvantage is compensated by much better power

density and longer life time. Because the energy density of a capacitor increases with the square of the voltage, a substantial improvement in energy density can be attained by using nonaqueous electrolytes instead of aqueous ones. A higher operating voltage of 3.5 to 4.0 V has been achieved in non-aqueous electrolyte, rather than 1 to 1.2 V in aqueous electrolyte, which results in higher energy density[1]. However, the high resistivity and degradability of non-aqueous electrolyte have limited the power density and hence the capacitive properties. Figure 2-3 compares the energy density and power density in aqueous and nonaqueous electrolyte[2]. The thickness of the active layer is the parameter along the curve with a thickness of 1μm at the left end and 1000 μm at the right end of the curves. The conductance of the aqueous electrolyte is 0.8 S/ cm while for the organic electrolyte a conductance of 0.02 S/cm was assumed. A maximum energy density of 20Wh/l is achieved for the organic electrolyte and a maximum power density of $2x10^6$ W/l is obtained for the aqueous electrolyte. It also can be seen from the graph that the energy density decreases with film thickness (< 10μm) at almost constant power density. This can be attributed to the internal resistance which is determined by the electrolyte. A similar phenomenon is attained for thick films (> 100μm) where the power density decreases with a constant energy density. This can be explained as that the internal resistance is determined by the resistance of porous layer instead of electrolyte.

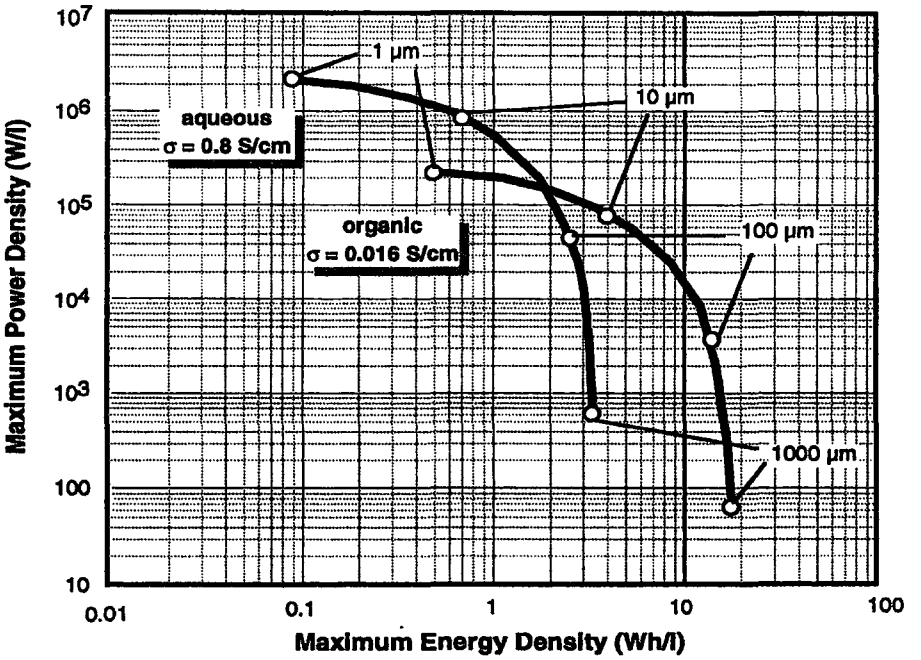

Figure 2-3 Calculated maximum achievable power density and maximum achievable energy density for two capacitors with aqueous (1 V) and organic electrolyte (2.3 V). The parameter on the curves is the active porous layer thickness. Assumptions: separator thickness: 25 µm, separator porosity: 50%, volumetric capacitance of porous layer: 100 F/ cm^2.

The voltage window achieved for electrochemical capacitors so far is in the range of 1 V (aqueous) to 3.5 V (organic electrolyte) which is relatively low compared to the required voltage of 42 V for electric vehicle battery-capacitor hybrid systems. Therefore, series stacks of several capacitor units would be required. Nevertheless, attention should be paid to the conditions for cell-unit matching in device fabrication to avoid overcharge or overdischarge in one or more elements of the series stack. A high-voltage series stack of low-voltage rated capacitors has the disadvantage related to reduction in the overall capacitance C_n compared to the capacitance C of each unit in the stack of n capacitors, and increasing total resistance R_n of the stack compared to the resistance R for each cell:

$$C_n = C/n \quad (2\text{-}4)$$

$$R_n = nR \quad (2\text{-}5)$$

2.2.3 Charge and discharge behavior

It is well known that the charge and discharge process in batteries are subject to polarization effects, as with all electrochemical reactions in the three-dimensional phases[11]. The maximum Gibbs energy is the product of charge Q and the difference of potential, ΔE , i.e., $G_{Batt} = Q \cdot \Delta E$. As the potential difference arises from the conversion from one oxidation state to another (e.g PbO_2 to Pb, NiOOH to $Ni(OH)_2$ etc al.), the thermodynamic potential (ideally) exists independent of the extent of charge Q added, so long as the two components (reduced and oxidized forms) of the electroactive material remain coexisting. Thus the potential difference (electromotive force, emf) of the battery cell is ideally constant throughout the discharge or recharge half-cycles as shown in Figure 2-4[1]. Due to the internal or solution resistance, there will be an ohmic IR potential drop depending on the charge and discharge rate, resulting in the separation of discharge curve from the recharge curve[2].

For capacitor, a linear relationship is obtained between voltage and charge withdrawn or added to the electrode system. The energy of the charging of a capacitor to a plate voltage difference of V is $(1/2)CV^2$. Since the total charge accumulated Q can be presented as CV, the total Gibbs energy stored in a capacitor can be expressed as

$G_{Cap} = \frac{1}{2}QV$, which is half that storable in a corresponding battery system for passage of the same charge. This difference has been explained by B. E. Conway in the following way: as a double-layer capacitor is charged, every additional element of charge that is added has to do electrical work (Gibbs energy) against the charge density already accumulated on the plates, progressively increasing the potential difference.

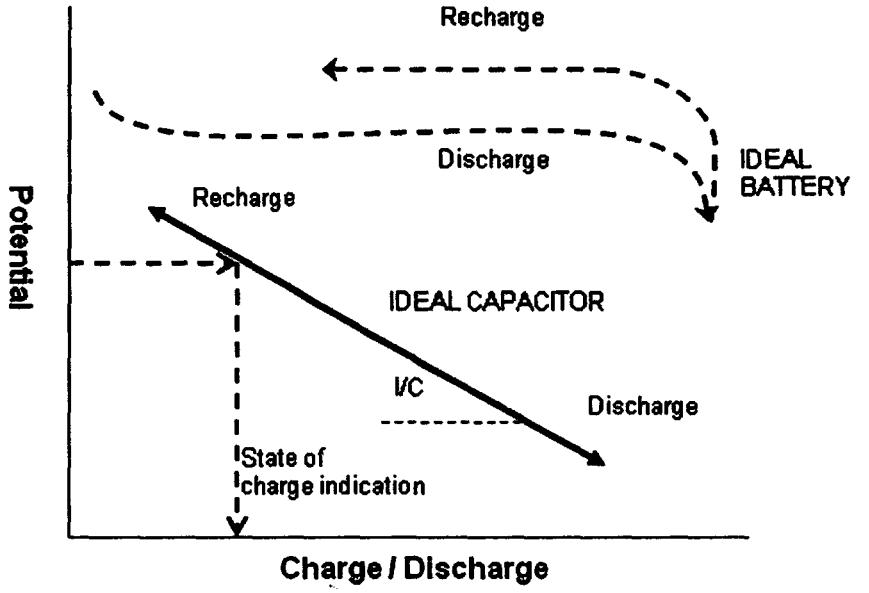

Figure 2-4 Difference of discharge and recharge relationships for a capacitor and a battery: potential as a function of state of charge, Q.

Although the energy density of electrochemical capacitors is lower than that of batteries, it is normally compensated by its great power density and reversibility. Ordinary battery materials always exhibit complete irreversibility between anode and cathodic sweeps. Figure 2-5 (a) shows the current response with potential changes for

$Pb/PbCl_2$ and indicates that the irreversibility increases as the scan rate increases. Figure 2-5 (b) demonstrates the capacitive behavior of RuO_2 in terms of the cyclic voltammogram. Almost a 'rectangular' current response is obtained to linear modulation of potential in time (dv/dt = constant) with great reversibility, which indicates an ideal capacitive behavior of the RuO_2 films.

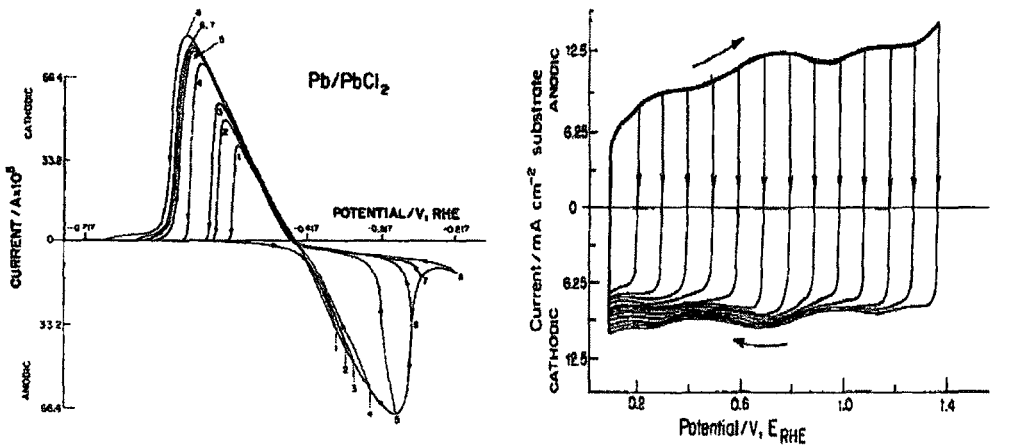

(a) (b)

Figure 2-5 Cyclic-voltammetry I vs. V profiles for (a) $Pb/PbCl_2$ battery electrode and (b) RuO_2 in 1 M aqueous H_2SO_4 (298K).

2.2.4 Advantages of supercapacitors compared with batteries

As mentioned in previous chapter, one of the biggest advantages of ES is its high power density due to the difference in energy storage mechanism and charge / discharge behavior of ES compared to batteries. It provides the possibility of ES with load leveling when combined with batteries and therefore reduce the battery size. The

fast recharging rate will help with improving the energy efficiency. Also, cycle life of up to 10^6 cycles at high depth of charge and discharge and good reversibility makes sure that the ES can be working under high performance with very long life time.

2.2.5 Applications of supercapacitors

Dedicated for energy storage, ES[1, 12] offer new solution for many other applications. Significant interest has been generated in high power ES for railway and subway type applications. ES have been utilized for door actuation applications in new aircrafts. ES are important for the development of photovoltaic generation systems, which need to be connected to the grid that acts as a pool of energy. In such systems ES can be used to store energy, which can be delivered with high power efficiency. The development of advanced ES is expected to enable radical innovation in the area of consumer electronics and communication devices. ES have been utilized for cellular phones, CD players, cameras, power sources for lasers and computers. An extensive application in hybrid vehicles of low cost ES with large capacitance has been introduced to recent market. Since high power is only required for engine start up and acceleration, by combining ES with batteries for load leveling, the lifetime of battery can be significantly prolonged. Also the fast charge/discharge rate enables the ES to regenerate the energy during braking and deceleration, thus improve the fuel consumption and optimize the operation of engine.

ES are important for the commercialization of fuel cells. Engineering and economic problems related to the development of fuel cells could be minimized if cars could be built without having excessive power. Instead of designing the high power primary system, low power system can be used, with ES acting as power reserves to deliver peak power during a limited time. ES support batteries or replace batteries in electric vehicles. The power densities of ES (~10 kW/kg) are two-three orders of magnitude better than batteries and fuel cells.

2.3 Electrode materials

As discussed earlier, the electrochemical capacitors can be divided into two groups as double-layer capacitors and supercapacitors, depending on the energy storage mechanism. From other criteria with respect to electrode materials, there are mainly three categories of electrochemical capacitors: carbon based, metal oxides and polymeric materials.

2.3.1 Carbon supercapacitors

The application of carbon as a double layer capacitor electrode material arises from a unique combination of chemical and physical properties as listed below:

- High conductivity
- High surface area

- Good corrosion resistance
- High temperature stability
- Controlled pore structure
- Processability and compatibility in composite materials
- Relatively low cost

The first two of these properties are the most important factor for the construction of a electrode for double layer capacitors. Low conductivity limits the maximum power density of the capacitor and, ultimately, its application. The main contributors to the internal resistance have been referred to as the equivalent series resistance (ESR), which includes the electronic resistance of the electrode materials; the interfacial resistance between the electrode and electrolyte; the electrolyte resistance; the ionic (diffusion) resistance of ions moving in small pores and through the separator[11, 13]. The resistance of the carbon materials is influenced not only by the chemical and structural morphology, but also by the contact resistance (inter-particle resistance)[14, 15]. Particle contact resistance is a major contributor to the resistance of carbon powders which highly depend on both the physical morphology of the carbon particle (e.g., size, shape, aggregation, etc.) and the pressure that is applied to compact the particles[14, 15].

Besides the conductivity, the performance of an EDLC, such as the capacitance and d.c. resistance are strongly effecting by the specific surface area and pore size distribution[16]. In order to achieve a high capacitance the electrode surface area is

additionally increased by using porous electrodes with an extremely large internal effective surface. There are mainly three classes of pores classified by IUPAC[17]: micropores (diameters less than 2 nm), mesopores (diameters between 2 nm and 50 nm) and macropores (diameters greater than 50nm).

Micropore sizes are in the molecular dimensions and influence the selectivity of adsorption-based processes, through restricted diffusion and molecular sieve effects[18]. Adsorption in such fine pores can occur via a pore filling mechanism rather than solely by surface coverage which may lead to a wrong estimation of accessible surface area for adsorption. Also in narrow micropores, the electrolyte diffusion will be restricted through the solution resistance and the ionic resistance, which will result in poor frequency response and a low rate capability. Therefore, the micropores only can make a minor contribution to charge-storage capacity under high-rate, or short duration, power pulse discharge / recharge[1].

Mesopores allows better adsorbate accessibility because of their relatively larger size. However the mesopores act as transport avenues into the interior of carbon particles rather than a main contributor to the surface area.

For macropores, each pore can be considered as an equivalent circuit of a line of R and C elements representing the double layer capacitance and the corresponding electrolyte resistance at a particular depth of the pore (Figure 2-6)[2]. The resistance of bulk electrode is assumed to be much smaller than the electrolyte resistance. At low frequency, electrolyte ions have time to penetrate into the depth of the pores and

additional surface area is accessed. As the frequency increases, the current flow predominantly through R1 and C1 into the bulk material and almost no current flows deep down the pore. In this case, the electrolyte penetration becomes poorer and less surface area is accessed. Larger pores result in lower distributed electrolyte resistance and greater electrolyte penetration which will optimize the surface area, ultimately, the utilizing the capacitance[2] Considerable research is presently being directed towards the development of carbon materials with a tailored pore-size distribution to yield high capacitance and low resistance electrodes.

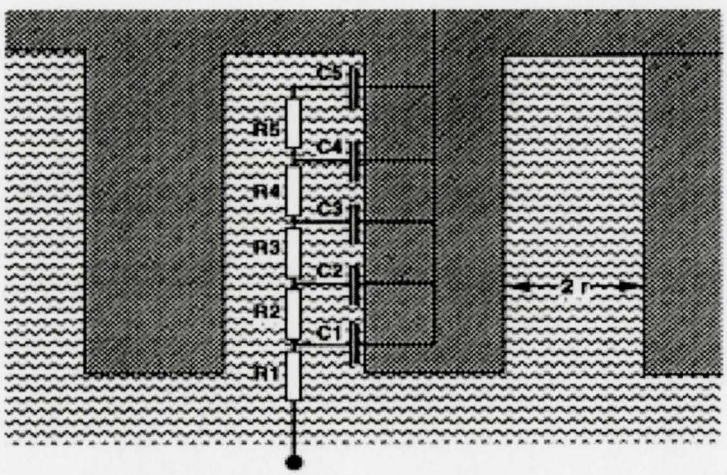

Figure 2-6 Equivalent circuit representation of the distributed resistance and capacitance within a pore.

2.3.2 Metal oxide supercapacitors

In contrast to carbon, which relies on the double layer formation to provide capacitance, other materials such as transition metal oxides, nitrides, and some

conducting polymers produce a reversible redox reaction, which provide pseudocapacitive behavior. Various approaches have been taken to develop suitable metal oxides for capacitor development.

Manganese oxide

Manganese oxides have attracted a lot of interests for supercapacitor applications due to its low cost, environmentally friendly character and high SC. Figure 2-7 shows the comparison of the cyclic voltammetry (CV) curves of manganese oxide with other oxide materials. It can be seen that the manganese oxides show the most ideal rectangular shape of CV curves compared to the other materials. The absence of redox peaks on the CV curve indicates a very good capacitive behavior. Also the voltage window of manganese oxides can be as high as 1 V vs SCE while it is only 0.5 V for nickel oxides and cobalt oxides. As mentioned earlier, according to equation (2-2) and (2-3), the energy density is strongly dependent on the voltage. Therefore, higher energy density and power density are expected for manganese oxides.

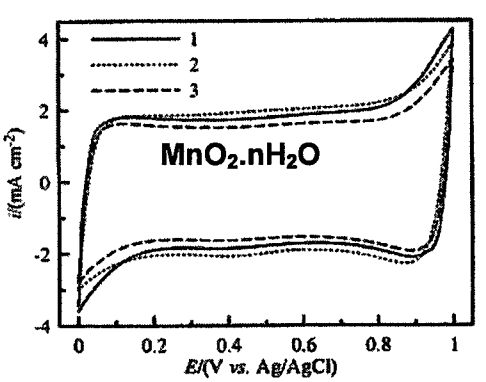

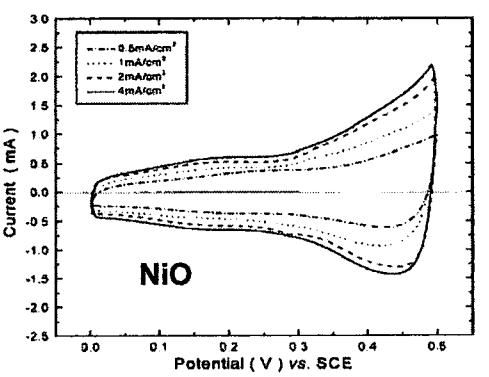

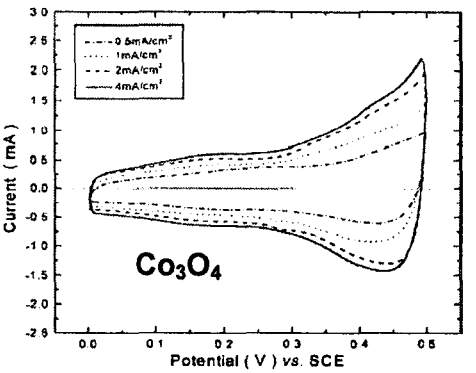

Figure 2-7 Cyclic voltammetry (CV) curves of manganese oxides, nickel oxides and cobalt oxides.

Capacitance is another key factor to optimize the energy density of a supercapacitor. Maximum capacitance of 700 F/g has been achieved for thin film of manganese oxide (~100Å) compared with 280 F/g for NiO_2 and 164 F/g for Co_3O_4. The high capacitance value of MnO_2 may be attributed to its microscopic intergrowth structure (Figure 2-7). The preferred manganese dioxide phase in alkaline electrolytes is γ–MnO_2. The basic building block for the structure is the $[MnO_6]$ octahedra manganese at the centre and oxygen at each of the vertices, which in various edge and corner sharing arrangements leads to different structural varieties of manganese dioxide[19]. The interior channels are beneficial for ion transport and energy storage.

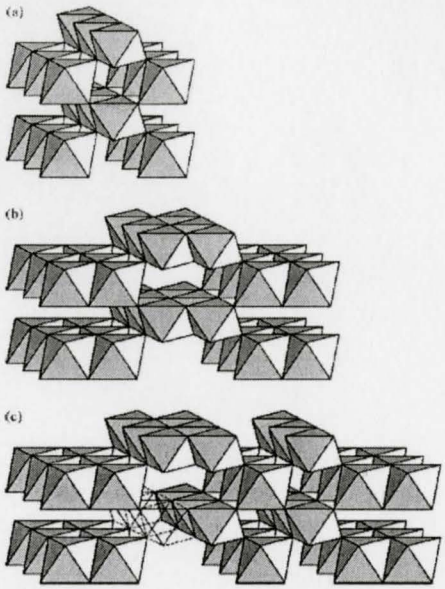

Figure 2-8 Structural components of (a) pyrolusite; (b) ramsdellite; and (c) γ–MnO_2

The charge storage mechanism of manganese oxide is based on the absorption of ions on the oxide surface. A possible redox reaction involving exchange of protons and/or cations has been proposed to explain the energy storage mechanism[20]

$$MnO_2 + H^+ + e^- \leftrightarrow MnOOH \qquad (2\text{-}6)$$

or

$$MnO_2 + C^+ + e^- \leftrightarrow MnOOC \qquad (2\text{-}7)$$

Reaction 2-6 and 2-7 indicate the intercalation of protons (H^+) or alkali metal cations (C^+) in the bulk material upon reduction followed by deintercalation upon oxidation[21] Equation 2-8 presents the adsorption of electrolyte cations (C^+) on the surface of electrode[22]

$$(MnO_2)_{surface} + C^+ + e^- \leftrightarrow (MnO_2^-C^+)_{surface} \qquad (2\text{-}8)$$

where C^+= Na^+, K^+, Li^+. The mechanism was proposed from the observations of cyclic voltammetry and capacitance of MnO_2 in electrolyte containing different metal alkali cations[22]. Since the charge/discharge process involves redox reaction and ion exchange, the capacitance of MnO_2 is strongly affected by the film thickness due to the ion diffusion. A very high capacitance of 1380 F/g has been achieved by Toupin et al.[20] which is close to the theoretic value of 1370 F/g excepted for a redox process involving one electron per manganese atom. Both the capacitance and Columbic efficiency decreased when the film thickness increased, demonstrating that not all the MnO_2 deposit was electrochemically active in thick films. This suggests that slower ionic transport is occurring within the active material or that protons can not diffuse freely across the thickness of the MnO_2 particles[20]. This is supported by the relatively low diffusion coefficient ($6x10^{-10}$ cm^2/s) for protons in manganese dioxide[23].

It has been reported that the specific capacitance of a supercapacitor is dependant on the deposition temperature and the current density[24, 25]. Higher deposition rate was obtained at lower temperature. The increase in the current density resulted in a film with greater hydration and higher capacitance[25].

Manganese oxides films have been prepared from different starting materials for application as electrode material in electrochemical capacitors utilizing different fabrication methods. Chin et al. have demonstrated that MnO_2 films can be deposited from colloidal solution, which showed a specific capacitance of 720 F/g[26]. Lee et al. [22] prepared MnO_2 by thermal decomposition of $KMnO_4$ at different temperatures and

proposed non-corrosive KCl as electrolyte. Jeong and Manthiram[27] prepared MnO_2 by reduction of $KMnO_4$ by aqueous solution of potassium borohydride (KBH_4), sodium dithionide ($Na_2S_2O_4$) and sodium hypohposphite ($NaH_2PO_2 \cdot H_2O$). Pang et al obtained homogenous, highly porous manganese oxide powders using sol-gel method, by reduction of $NaMnO_4$ and $KMnO_4$ with sodium fumarate[28]. Cheng have shown that amorphous hydrous manganese oxide can be deposited anodically onto a graphite substrate from a $MnSO_4 \cdot 5H_2O$ solution with pH of 6.4[29].

Other metal oxides

Ruthenium oxide has attracted much interest as the best electrode material for high power/energy density electrochemical capacitors due to its outstanding specific capacitance and long cycle life. High conductivity and good electrochemical reversibility are also advantages of ruthenium oxide over other electrode materials. High specific capacitance of ruthenium oxide is originated from the reaction between Ru ions and H ions in acidic electrolytes[30, 31]. High specific capacitance of 720 F/g has been reported for hydrous forms of ruthenium oxide ($RuO_2 \cdot xH_2O$) prepared by sol-gel process at a scan rate of 2 mV/s[32]. For anhydrous ruthenium oxide (RuO_2), maximum specific capacitance has been reported for 380 F/g at a scan rate of 100 mV/s[33]. However, hydrous ruthenium oxide prepared by sol-gel process does not exhibit capacitor-like behavior in its cyclic voltammogram at scan rates higher than 50 mV/s. Its specific capacitance drops to 250 F/g at scan rate of 50 mV/s while the

CV curves are deviate from the ideal shape. A better high rate performance has been obtained for the ruthenium oxide carbon composite electrodes compared with the hydrous ruthenium oxide prepared by sol-gel process[34]. Maximum specific capacitance of about 600 F/g was obtained for the composite electrode composed of 20 wt% activated carbon and 80 wt% hydrous ruthenium oxides at high scan rates over 50 mV/s. Sol-gel process is the most widely used among various preparation techniques for ruthenium oxide. Sol-gel process for hydrous ruthenium oxide, however, is a complicated multistep process and takes a relatively long process time as required in repeated washing and filtering steps of precipitated ruthenium oxide powders from precursor solution[32].

Nickel oxide is another potential candidate for supercapacitor electrodes. Porous films of NiO_x have been prepared by Liu et al. using sol-gel technique, which demonstrating specific capacitance of 200 to 256 F/g[35]. Srinivasan et al. developed an electrochemical precipitation technique followed by heat treatment to fabricate nickel oxide electrodes[36, 37]. A specific capacitance of 240 F/g was obtained and the effect of heating conditions, electrolyte environment, as well as the potential range of operation on the capacitance has been studied. It was found that the pseudocapacitance increased with the electrolyte concentration while holding the potential window constant. Higher deposition rate was observed with an increase in the deposition current density and with a decrease in the deposition solution concentration[38]. The surface morphology of the deposited film changed from a flat and dense structure to a

highly porous structure when the deposition rate increases. Maximum capacitance was obtained within the potential window of 0.0 to 0.45V which is five times larger than that obtained in the potential range of -0.5 to 0.0V vs. SCE, thus making nickel oxide best suited as a positive electrode in devices[38]. The energy storage mechanism has been reported based on the OH^- adsorption and desorption reaction as shown in Equation (2-9).

$$Ni(OH)_2 + OH^- \leftrightarrow NiOOH + +H_2O + e^- \qquad (2\text{-}9)$$

Nam et al. has suggested that at the initial stage of the oxidation, H^+ ions are released from the oxide surface and simultaneously combined with OH^- ions in the solution to form H_2O before the adsortption of OH^- ions to the oxide surface [38].

2.3.3 Polymer electrodes

Conducting polymers have been regarded as promising supercapacitor materials due to their fast charge-discharge kinetics, low cost, suitable morphology and fast doping-undoping process. Such materials can possess high capacitance since the charge processes pertain to the whole polymer mass and not only to the surface, as in the case of double layer supercapacitors. Among all the polymers, several polymers are attracting more interest in the application of supercapacitors because of its high capacitive characteristics, low cost and ease of synthesis, such as polymethyl methacrylate (PMMA)[39], p-phenylenevinylene (PPV)[40], polypyrrole (PPy)[41, 42],

polyaniline (PANI)[43, 44], poly-(ethylenedioxythiophene) (PEDOT)[45] and polyaniline[46]. Conducting polymer electrodes with nanostructure are beneficial for energy storage due to the high surface area and high porosity which can provide distinctive characteristics of conducting pathways, surface interactions and nanoscale dimensions. The structure is dependent on different factors including monomer concentration, electrolyte used and electrode potential[47]. Extensive research has been carried out in developing high surface area nanomaterials such as nanotubes, nanowires, etc[48, 49]. Polymer electrode has been fabricated using different indirect methods including template synthesis[47], self-assembly[50] and interfacial polymerization[51]. However, surfactants are required for these fabrication methods which will result in large contact resistance between the nano-structured polymer and the substrate. A direct deposition method has been reported by Gupta et al. using polyaniline nanowires on stainless steel plates[46]. A high capacitance of 775 F/g was obtained at a scan rate of 10mV/s in 1 M H_2SO_4 electrolyte while a capacitance of 562 F/g was obtained at the high scan rate of 200 mV/s. This decrease of 25% in specific capacitance is much lower then that obtained for the case of metal oxide, which is in the range of 50-80%[52]. The polyaniline electrode also demonstrated good stability after 1500 cycles.

2.4 Electrolytes

According to Equation (2-2) and (2-3), voltage window and resistance play very important roles in order to optimize the power density and energy density. The nature of electrolyte is greatly affecting the electrical properties of supercapacitors including the voltage window and equivalent series resistance (ESR).

2.4.1 Aqueous electrolytes

Aqueous electrolyte has a limited unit cell voltage of typically 1.23V[1], due to its decomposition voltage. The low operating voltage will result in a low energy density compared with organic electrolytes according to Equation (2-2). However this disadvantage can be compensated by the high conductivity of aqueous electrolyte, also purification and drying processes are no longer critical issues. In addition, the cost of aqueous electrolytes is much lower than for suitable organic electrolytes. Relatively concentrated electrolytes are required to minimize the ESR and also to avoid the electrolyte depletion problems during charging. Alkaline electrolytes, such as KOH and NaOH are favored than the acid electrolytes since they are less corrosive. However, both the acid and alkaline electrolytes have advantageously high conductivities in aqueous medium owing to the special mechanism of proton transport. In order to overcome the disadvantage of small voltage window, researches have implied asymmetric cell design by using two different electrochemical processes,

proceeding on different electrodes of one cell. A hybrid capacitor with a negative Fe_3O_4 composite electrode and a positive MnO_2 composite electrode exhibited voltage window of 1.8 V[53]. Hybrid electrode configurations, consisting of two different electrodes show considerable potential for the development of advanced ES.

2.4.2 Organic electrolytes

Organic electrolytes are favored for application of supercapacitors due to their high achievable voltage which results from the high decomposition potential limits. Since the stored energy increases with V^2 (Equation 2-2), higher voltage window can improve the energy density significantly. Organic electrolytes allow a cell voltage as high as 2.3 V, with the possible achievement of 2.7 V for a short time. The cell voltage is most probably limited by the water content of the electrolyte[2]. Extreme purification procedures of special electrolyte have been carried out by some companies in order to achieve higher voltage of 3.2 V. However, special protective coatings were required to reduce the corrosion of the carbon electrodes[54]. Tetraalkylammonium salts have been preferred electrolytes owing to their good solubility in nonaqueous solvents and moderately good conductivity[1]. Deposition of alkali-metal on the cathode electrode can be avoided by using such salts upon overcharge. However, if such electrolyte is not purified and dried enough, H_2 and O_2 may form on charge and subsequent recombination reactions, which will lead to self-

discharge. Also, it can easily decompose on strong overcharge, usually at the negative electrode. A drawback of organic electrolyte is its high resistance, which is about 20 to 50 times higher compared to a concentrated aqueous electrolyte. The higher electrolyte resistance will affect the ESR, thus reduce the maximum power density. Therefore, although organic electrolyte possess the advantage of high operating voltage window, it has to be balanced against higher cost, lower conductivity, smaller power capability, more complex production conditions to maintain dryness and greater potential for degradation than for the aqueous system types.

2.4.3 Ionic electrolytes

Ionic liquid is defined as the liquefied salts when a heat is provided to the system to counterbalance the salt lattice energy[55]. The electrolyte consists of ions and their combinations, but no solvent molecules, unlike the classical electrolyte which obtained by dissolution of salts in molecular solvents. The temperature range of the ionic liquid is determined by the melting point of the salts, which can be lowered with the addition of other salts forming eutectic. The first attempt of use ionic liquid as electrolyte in supercapacitor applications was brought up by Osteryoung et al.[56] which contained tetrachloroaluminate anion as well as Cl^-. However, the chloroaluminate anions limited the electrochemical window and may react with water and oxygen. To avoid these disadvantages of ionic liquid containing Cl^-, Lewandowski et al.

developed electrochemical capacitors based on activated carbon powders (ACP, specific surface area 870 and 2600 m^2/g) and Cl^- free ionic liquids as electrolytes[57]. It was reported that the electrochemical stability window of ionic liquids determined at a glassy carbon electrode was in the range of ca. 3.0-4.2 V while the obtained specific capacitance value is in the range of 45 F/g to 180 F/g. Lewandowski et al. also prepared a EC using polymer ionic liquid solid electrolytes by casting technique. The carbon based EC demonstrates a specific capacitance up to 200 F/g[58]. Although the literature on ionic liquid electrolyte is so far very limited, ionic liquids seem to be promising candidates for electrolytes in EC applications due to high specific capacitance at the activated carbon and electrolytes interface as well as broad operating voltage window.

2.5 Design of electrochemical supercapacitors

Efficiency is a critical issue for EC in electric vehicle applications. Part of the available energy is dissipated at the internal resistance ESR. At high power, i.e. high current, this loss becomes dominant[2]. It has been reported that a good capacitor can have a slight advantage over a good battery in terms of round trip efficiency. The efficiency of 92% has been obtained for capacitors while 85% for battery[59]. Therefore, reducing the ESR of capacitors is very important in order to make it more compatible. On the other hand, the choice of electrolyte, electrode materials, separator thickness

and porosity also plays a critical role in improving the supercapacitor performance. Porous structure of the electrode has to be tailored for the size and the properties of the respective electrolyte. Monopolar cell arrangement has been implied to supercapacitor applications expecting faster discharge rate and homogeneous current distribution. However, higher ERS may be introduced. The use of bipolar cell arrangement can reduce the internal resistance. Moreover, the bipolar cell design is an elegant way to connect many cells in series in order to obtain higher cell voltage, without introducing extra wiring and contact resistance. However, complicated sealing concept is required for each cell.

2.6 Fabrication methods

The current fabrication methods for electrode of supercapacitor include sol-gel, colloidal method, coprecipitation method and anodic deposition. Pang et.al[21] has developed a sol-gel-derived method to produce thin films of MnO_2. The colloidal MnO_2 was prepared by reducing Mn^{7+} with Mn^{2+} in alkaline aqueous medium (pH=10.5) and the thin films were then formed by either dip-coating or drop-coating colloidal MnO_2 directly onto substrates. Films of different thickness were prepared by repeating the dip-coating or drop-coating process before final heat treatment. However, sol-gel preparation involves the hydrolysis and condensation of metal ions. The problem in preparing MnO_2 using sol-gel method is lack of stable Mn (IV)

precursors. It has been reported that this problem can be circumvented by in-situ formation of Mn (IV) via reduction of $NaMnO_4$ with sodium fumarate[60]. Pellet ruthenium oxide electrode has been produced by cold pressing the powder filtered from colloidal solution of $RuCl_3 \cdot xH_2O$ and $NaHCO_3$[61]. Sputter deposition and electrostatic spray deposition techniques have also been utilized to fabricate manganese oxide electrodes[9,62]. Lee et.al has prepared amorphous hydrous manganese oxide by a coprecipitation method by mixing of $KMnO_4$ and manganese acetate aqueous solution to be coprecipitated in the reaction[63]. Nevertheless, this chemical coprecipitation method involves relatively complicated steps and processes of oxide preparation and electrode fabrication. Hu et. Al introduced an anodic deposition method by using $MnSO_4 \cdot 5H_2O$ solution[64]. Hydrous manganese oxide also has been observed by anodic deposition method from different deposition precursor including $Mn(CH_3COO)_2$, $MnSO_4 \cdot 5H_2O$, $MnCl_2 \cdot 4H_2O$ and $Mn(NO_3)_2 \cdot 4H_2O$[65]. However the anodic deposition method will involve anodic oxidation and dissolution of the high surface area metallic current collectors which limits its extensive applications. After all, it is more desirable to employ an alternative technique to replace the current fabrication method for preparing the electrodes with excellent capacitive characteristics for the application of ES.

Electrochemical deposition has attracted more interest for the preparation of thin films and coatings since it can offer rigid control of film thickness, uniformity and

deposition rate. As an electric field is used, electrodeposition is particularly suited for the formation of uniform films on substrates of complicated shapes, impregnation of porous substrates, and deposition on selected area of the substrates. Electrochemical deposition can be divided into two techniques: electrophoretic (EPD) and electrolytic (ELD) deposition (Figure 2-9)[66]. Electrophoretic deposition is achieved via motion of charged particles towards an electrode under an applied electric field. Electrolytic deposition produces colloidal particles in cathodic reactions for subsequent deposition. EPD is normally utilized to produce thick films while ELD enables the formation of nanostructured thin ceramic films (Figure 2-10)[66]. Both of the EPD and ELD can be performed by cathodic and anodic methods.

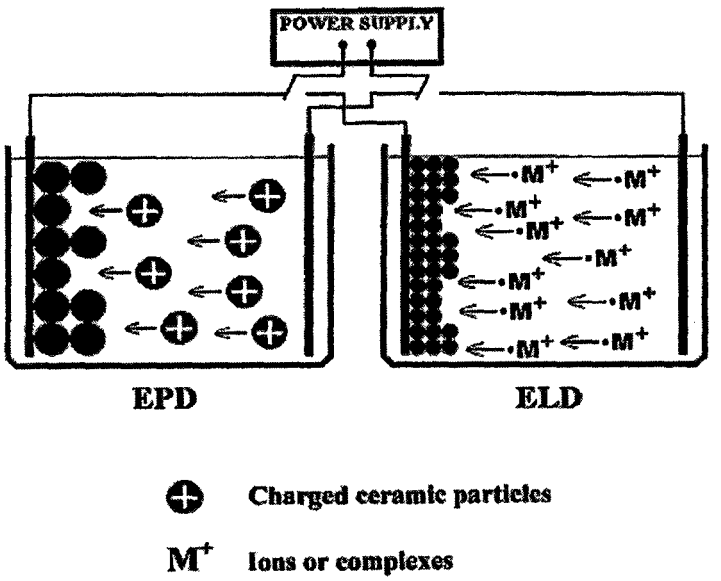

Figure 2-9 Schematic of cathodic electrophoretic deposition (EPD) and electrolytic deposition (ELD), showing electrophoretic motion of positively charged ceramic particles and ions (M^+), followed by hydrolysis of the ions to form colloidal nanoparticles and coagulation of the particles to form EPD and ELD deposits.

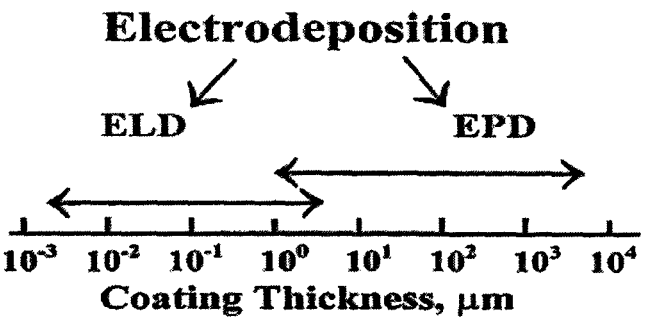

Figure 2-10 Thickness of coatings deposited using ELD and EPD.

Solvent plays a very important role for electrodeposition as it acts as a vehicle that carries the ceramic particles in suspensions (EPD) or ions in solutions (ELD). There are mainly two types of solvent used for electrodeposition, water and organic liquids. It has been reported that ELD requirse water for base generation in cathodic reactions[66]. The deposition rate for electrolytic zirconia films is shown in Figure 2-11[66]. It can be seen that as the water content increases to 2 wt%, there is a sharp increase in deposition rate. However, absorbed water in green deposits leads to shrinkage and cracking during drying.

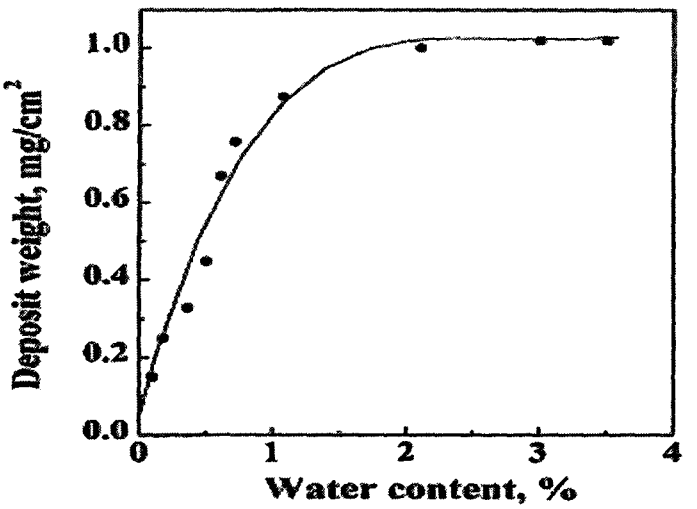

Figure 2-11 Deposit weight of ELD films versus water content in 0.005 M $ZrOCl_2$ solutions in mixed ethyl alcohol-water solvent, current density 5 mA/cm^2, deposition time 5 min.

The hydrating can be prevented by using non-aqueous solvents. By mixing methyl alcohol-water and ethyl alcohol-water solutions, cracking and porosity can be reduced in the electrolytic deposits[67]. Enhanced deposition rate has been found when performing the deposition in mixed methyl alcohol-water solutions[68]. This can be attributed to reduction of the thickness of the double layer which results in a reduction in dielectric constant of the solvent, hence promoting particle coagulation.

Organic liquids are preferred to water as a suspension medium for EPD. Gas will be formed from the hydrolysis of water if a water-based suspension is used, which will result in non-uniform films and pinholes. Also a mixture of solvents may be useful to achieve particle charging. Alcohols are well-known to behave as proton donors and are important for particle charging.

Binders are added to suspensions or solutions to increase the adherence and strength of the deposited material and prevent cracking. The optimal amount of binder depends on the particle size and particle surface area. Organic binders are preferred to water-soluble binders due to their high strength. Non-ionic-type polymers are the most commom binders used in electrophoretic deposition. The polymeric molecules adsorb onto the surfaces of ceramic particles. The positively charged ceramic particles will be attracted to the cathode with the polymeric molecules which results in film formation on the cathodic substrates (Figure 2-12a)[66]. Cationic polyelectrolytes with inherent binding properties, such as poly(dimethyldiallylammonium chloride) (PDDA) or polyethylenimine (PEI), could be used for particle charging and electrophoretic deposition (Figure 2-12b)[66].

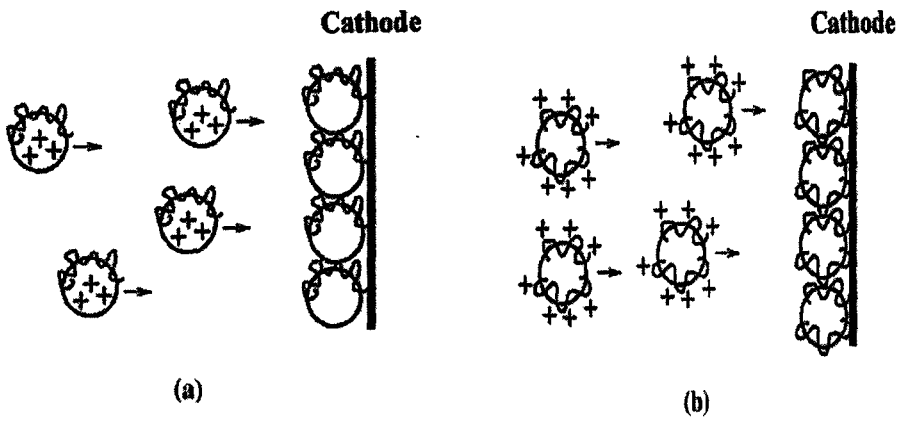

Figure 2-12 Cathodic electrophoretic deposition of ceramic particles with adsorbed (a) neutral and (b) charged polymers.

3 OBJECTIVES

Manganese oxides have become very promising materials for the application in supercapacitors. However there are certain disadvantages of the current fabrication methods for manganese oxides including sol-gel deposition method and anodic deposition. The sol-gel deposition method is only able to produce and stabilize very dilute suspensions and the MnO_2 is easily reduced to other oxides which are not electrochemically active. The anodic deposition method will introduce the anodic dissolution which prevents the utilization of high surface area electrode. Also the deposition solution may be contaminated by the ions dissolved from the anode.

The objective of this research is to develop a cathodic deposition technique for fabrication of MnO_2 and investigate the deposition mechanism, microstructure, composition, electrochemical properties and the influence of processing condition on the performance of the MnO_2 electrodes.

4 EXPERIMENT PROCEDURES

Cathodic deposition was performed from $KMnO_4$ and $NaMnO_4$ (Aldrich) aqueous solutions with the concentration of 20 mM to 100 mM at ambient temperature. Deposits were obtained on different substrates, including stainless steel, nickel plate and nickel foam, at a current density of $2mA/cm^2$. The deposition time varied in the range of up to 9 min. Electrochemical cell for deposition included a cathodic substrate and two platinum counter electrodes. Deposit weight was studied by weighing the substrates before and after deposition followed by drying at room temperature for 24 hours.

The deposited films were scraped from the substrates and characterized using X-ray diffraction (XRD), thermogravimetric analysis (TGA) and differential thermal analysis (DTA) techniques. The composition of the deposited films was studied by XRD with a diffractometer (NicoletI2) using monochromatic Cu Kα radiation at a scanning speed of 0.5^o/min. TGA and DTA tests were carried out in air between room temperature and 1200°C at a heating rate of $5^oC\ min^{-1}$ using a thermoanalyzer (Netzsch STA-409). The surface morphology of the deposited coatings was investigated using a JEOL JSM-7000F scanning electron microscope (SEM) equipped with energy dispersive spectroscopy (EDS).

The capacitive behavior of the deposited and annealed films was studied using a potentiostat (PARSTAT 2273), Princeton Applied Research) controlled by a computer

using a PowerSuite electrochemical software package. The electrochemical characterization of the films was performed using a standard three-electrode cell configuration with 0.1 M Na_2SO_4 aqueous solution as an electrolyte. Purified nitrogen gas was implied to degas the electrolyte solution before measurements. The surface area of the working electrode was $1cm^2$. The counter electrode was platinum gauze while the reference electrode was a standard calomel reference electrode (SCE). Cyclic voltammetry (CV) tests were carried out within a potential range of 0-1.0 V versus SCE at scan rates of 2-100 mV/s. The SC was calculated using half the integrated area of the CV curve to obtain the charge (Q), and subsequently dividing the charge by the mass of the electrode (m) and the width of the potential window (Δ V):

$$C = Q / (m\Delta V) \qquad (4\text{-}1)$$

Galvanostatic charge and discharge testing was performed at constant current density of 0.1-1.0 mA/cm^2. SC can be calculated from the obtained chronopotentiograms as well as the specific power density and specific energy density.

$$C = I /(\Delta E / \Delta t)m \qquad (4\text{-}2)$$

$$E_{power} = (I \cdot \Delta E) /(2m) \qquad (4\text{-}3)$$

$$E_{energy} = E_{power} \cdot \Delta t \qquad (4\text{-}4)$$

I = current

ΔE = potential difference

Δt = discharging time

m = sample mass

E_{power} = power density

E_{energy} = energy density

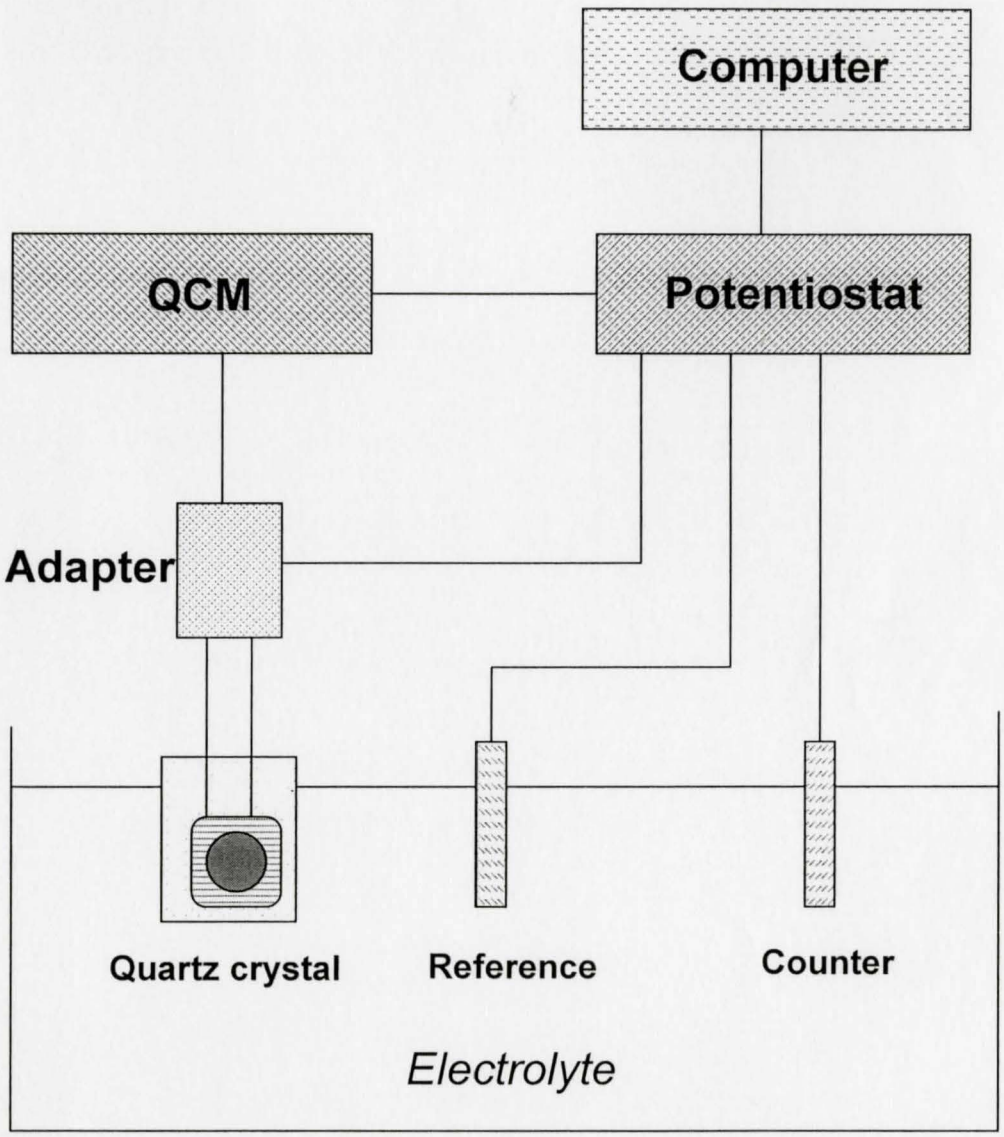

Figure 4-1 Instrumental set-up for the linear sweep voltammetry and QCM studies.

The deposition process has also been studied using a quartz crystal microbalance (QCM 922, Princeton Applied Research) controlled by a computer using a PowerSuite electrochemical software package. Figure 4-1 shows an instrumental set-up for the investigation of the deposition process using the linear sweep voltammetry and QCM studies. A three-electrode cell contained a quartz crystal working electrode, a platinum gauze counter electrode and a standard calomel reference electrode (SCE). The aqueous solution of the $NaMnO_4$ electrolyte was degassed with purified nitrogen gas before the deposition experiments.

The deposit mass Δm was calculated using Sauerbrey's equation[69]:

$$-\Delta F = \frac{2F_0^2}{A\sqrt{\rho_q \mu_q}} \cdot \Delta m \qquad (4\text{-}5)$$

where ΔF is frequency decrease of the QCM, F_0 is the parent frequency of QCM (9 MHz), A is the area of gold electrode (0.2 cm^2), ρ_q is the density of the quartz (2.65 g/cm^3) and μ_q is the shear modulus of quartz (2.95×10^{11} $dyne/cm^2$).

Cathodic deposits were also obtained galvanostatically on stainless steel and nickel foils (50×50×0.1 mm) at a current density of 2 mA/cm^2. The deposition time was varied in the range of up to 8 min. The electrochemical cell for deposition included a cathodic substrate and a platinum counter-electrode.

5 EXPERIMENTAL RESULTS

Cathodic deposition was successfully developed by using aqueous permanganate solutions. The experiment results can be divided into two parts based on the deposition precursor, 1) $KMnO_4$ aqueous solution and 2) $NaMnO_4$ aqueous solution. The influence of deposition conditions, heat treatment and testing conditions on the performance of the electrode was investigated.

5.1 Electrodeposition from $KMnO_4$ solutions

Cathodic deposits were obtained from 20mM $KMnO_4$ aqueous solutions on stainless steel foil substrates. The deposition yield increased with increasing deposition time at a constant current density of 2 mA/cm^2 (Figure 5-1), which indicates a possibility of easy control of the film thickness. The deposition mechanism was studied by the linear sweep voltammogram (Figure 5-2). The reduction peak was obtained at -0.75V vs. SCE. at a scan rate of 10 mV/s and shifted to higher potentials at higher scan rate within the range of 10 to 100 mV/s. The surface of the electrode turned dark due to the formation of manganese oxide when the potential approached the potential range of the peaks.

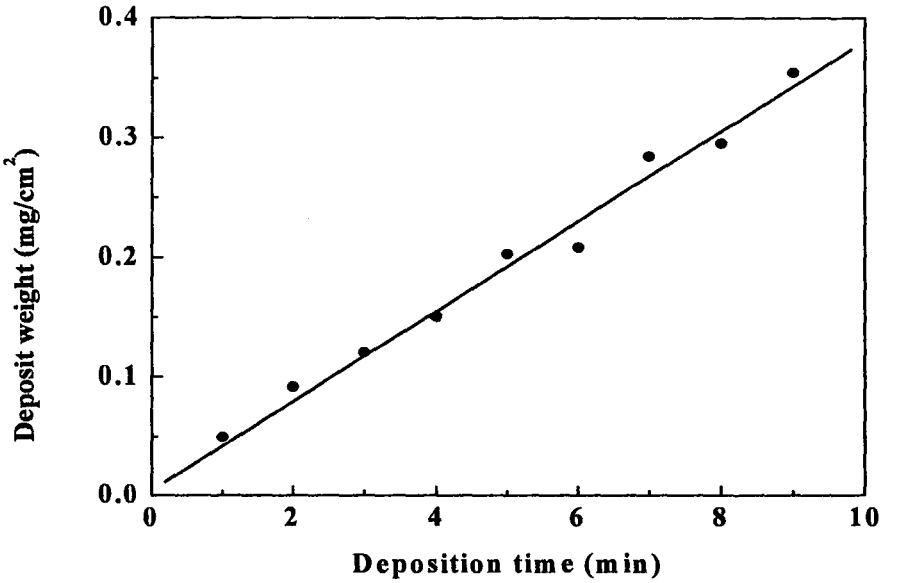

Figure 5-1 Deposit weight versus deposition time for deposits prepared at a current density of 2 mA/cm^2

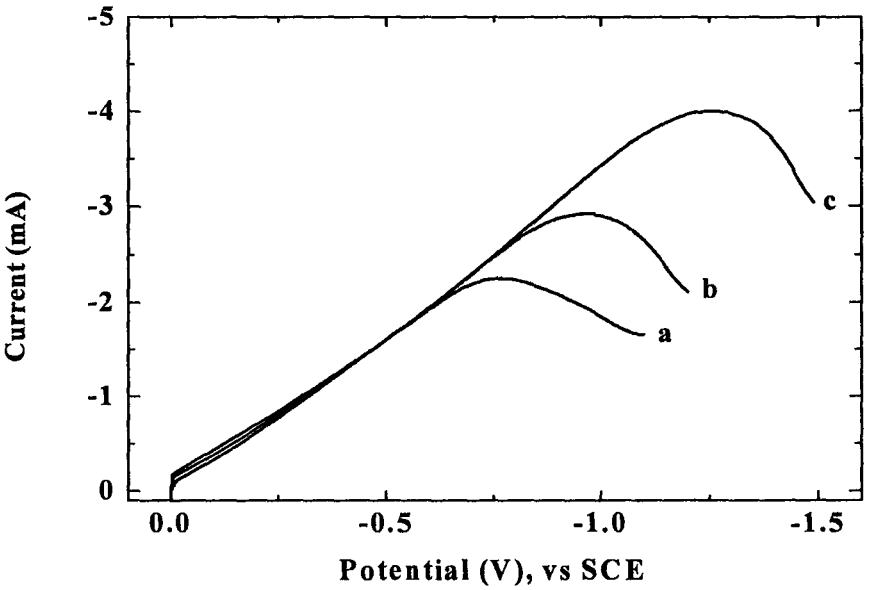

Figure 5-2 1 Linear sweep voltammograms for a stainless steel electrode in the 20 mM $KMnO_4$ aqueous solution at scan rates of (a) 10, (b) 50, and (c) 100 mV/s.

The deposited films were scratched off the substrates for XRD characterization as well as TGA and DTA.

Figure 5-3 shows that the as-prepared deposit was poorly crystalline at room temperature. After heat treatment at 200°C for 1 hour, the XRD spectrum exhibited broad peaks which can be attributed to rancieite structure (JCPDS file 22-0718). More distinct and sharp peaks were obtained at higher temperatures in the range up to 600°C.

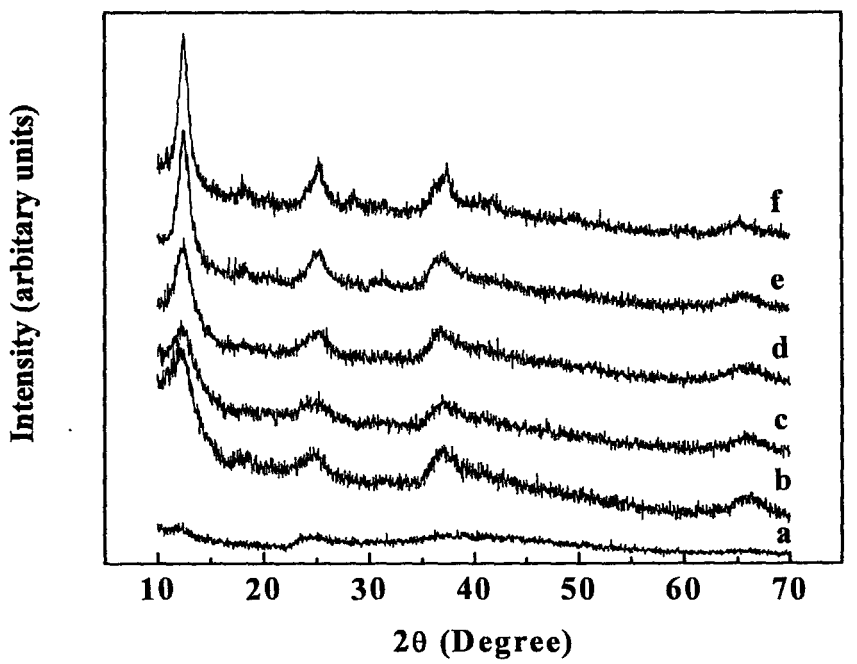

Figure 5-3 X-ray diffraction patterns for the deposits obtained from the 20 mM $KMnO_4$ aqueous solution at 2 mA/cm^2: (a) as prepared and after heat treatment at (b) 200°C, (c) 300°C, (d) 400°C, (e) 500°C, (f) 600°C.

The obtained deposits were studied by TGA and DTA in the temperature range from 20°C to 1200°C. The TGA data showed a sharp decrease in sample mass below 200°C,

followed by gradual weight loss up to 600°C (Figure 5-4). Additional step in weight loss was observed around 900°C. Small endotherms were observed in the DTA data at 100°C and 900°C. It is suggested that observed endotherms correspond to the steps in weight loss. The reduction in sample weight below 600°C can be mainly attributed to deposit dehydration. At temperatures exceeding 500°C the weight loss may be caused by the reduction of Mn^{4+} species and the formation of Mn_2O_3[70, 71]. The weight loss at ~900°C can be related to the formation of Mn_3O_4[70]. The EDS data has further supported the results from XRD analysis by showing the presence of K and Mn in the deposits with a K/Mn atomic ratio of x=0.35±0.04 (Figure 5-5).

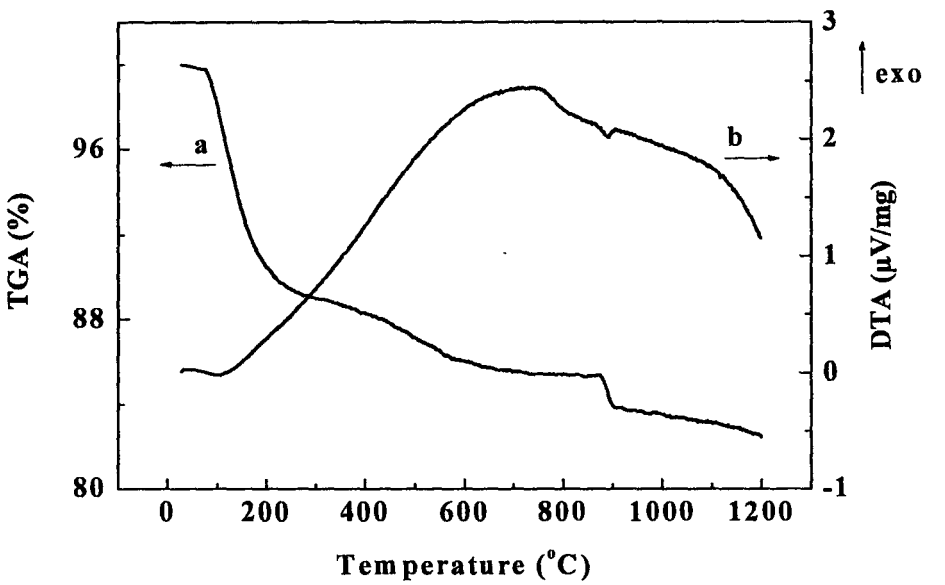

Figure 5-4 (a) TGA and (b) DTA data for the as-prepared film prepared from 20 mM $KMnO_4$ aqueous solution.

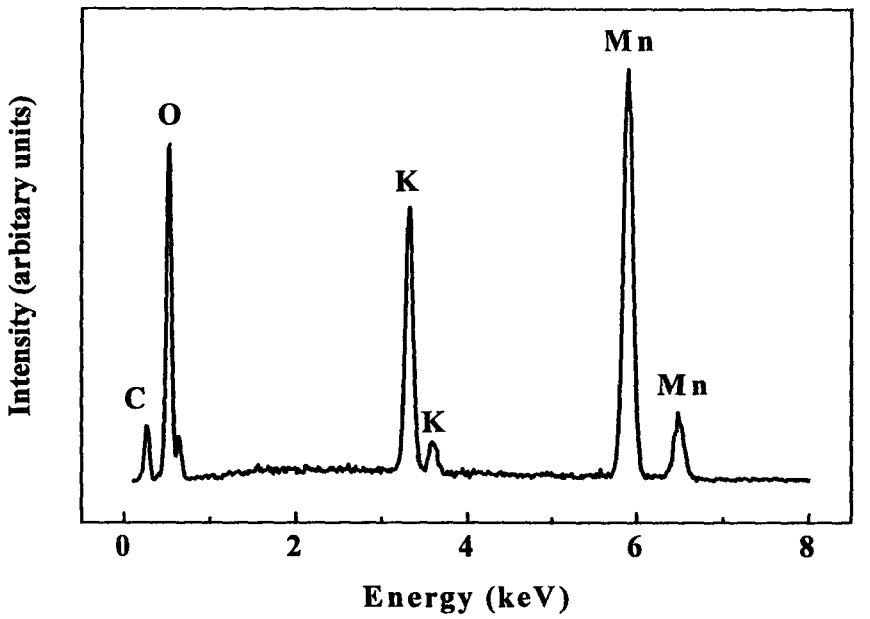

Figure 5-5 EDS data for films prepared from 20 mM $KMnO_4$ aqueous solution at 2 mA/cm^2.

The surface morphology of the deposit films was studied by SEM which revealed highly porous structure containing nano-whiskers at high magnification for the 90 $\mu g/cm^2$ film (Figure 5-6). This porous structure is believed to be beneficial for ion exchange and redox reactions which underlie the energy storage mechanism since it provides large surface area. The effect of heat treatment was investigated by heating the sample in air in the temperature range up to 600°C for 1 hour. No significant change in surface morphology was obtained for the $90mg/cm^2$ sample after heat treatment up to 300°C.

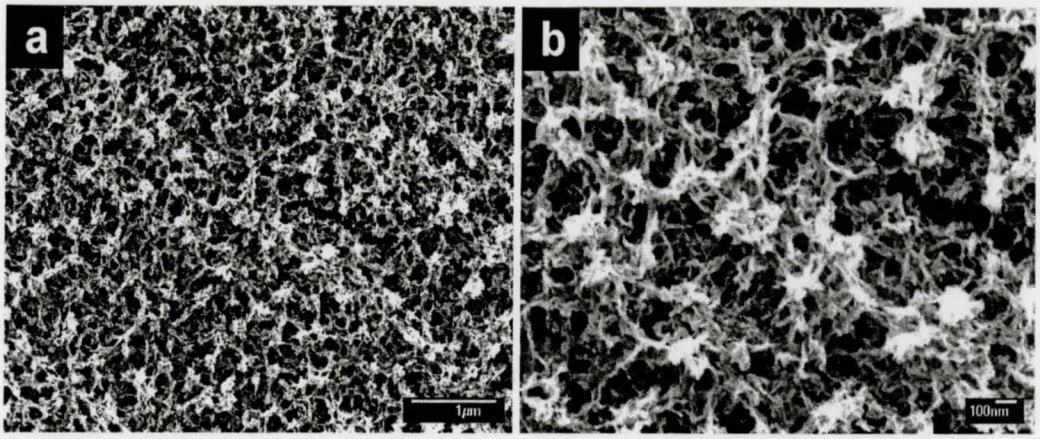

Figure 5-6 SEM picture of as-prepared 90 μg/cm^2 film at different magnifications

Cyclic voltammetry is an important tool to investigate the capacitive behavior of materials. Figure 5-7 shows typical CVs for the 90mg/cm^2 films within the potential range of 0 – 1.0V vs. SCE. No redox peak was obtained within the corresponding potential range and the rectangular shape of the CV window indicated ideal capacitive behavior of deposited films. Maximum specific capacitance of 222 F/g was obtained at the lowest scan rate of 2 mV/s (Figure 5-8). This is because that longer diffusion time into pores was allowed at low scan rate resulting in better ion exchange, hence higher capacitance. The decrease in SC was obtained with increasing scan rate due to the low electronic and ionic conductivity of manganese oxide. Similar dependencies were observed for other manganese oxides prepared by different methods[21, 72, 73, 74]

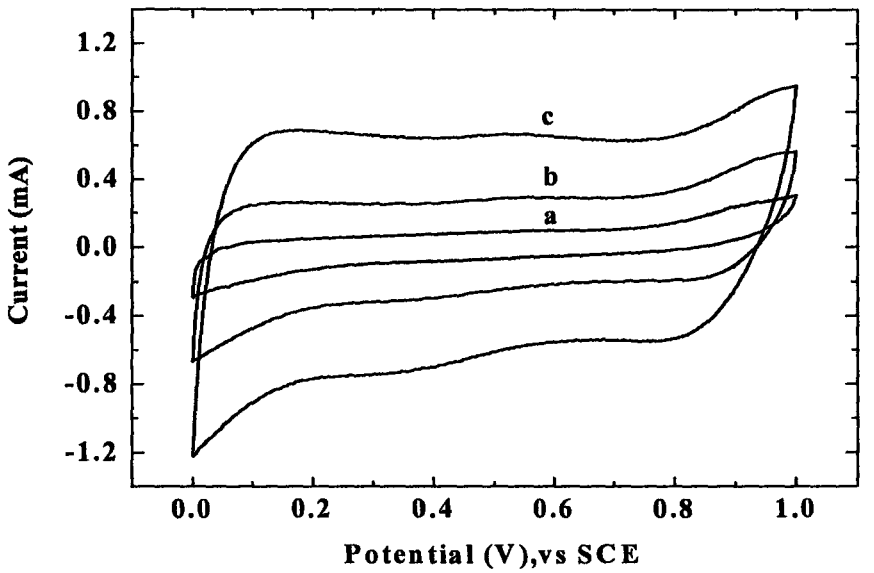

Figure 5-7 Cyclic voltammetry of as-prepared 90 μg/cm^2 film deposited from 20 mM $KMnO_4$ solution at the scan rates of (a) 5 mV/s, (b) 20 mV/s, and (c) 50 mV/s.

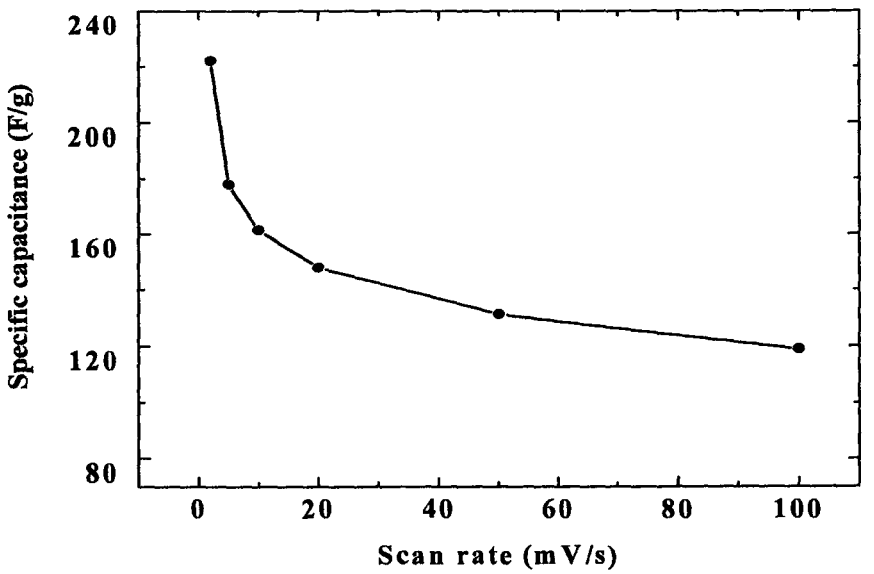

Figure 5-8 SC versus scan rate for the 90 μg/cm^2 film deposited from 20 mM $KMnO_4$ solution.

The charge-discharge behavior of the manganese oxide films was examined by chronopotentiometry. The galvanostatic charge-discharge cycling was performed between 0 and 1.0 V versus SCE at different current densities. Figure 5-9 shows galvanostatic charge-discharge curves for the 90 μg/cm^2 film. The average SCs for the manganese oxide films calculated from the chronopotentiometry data were found to be 156, 135 and 120 F/g for current densities of 0.2, 0.5 and 1 mA/cm^2, respectively. The SCs obtained from the chronopotentiometry data were close to the SCs calculated from the CVs. The symmetric charge and discharge curves further proved that the deposited films exhibited ideal capacitive behavior. The Ragone plot presented in Figure 5-10 indicates relatively high power-energy characteristics of as-prepared films. Maximum energy density of 28 Wh/kg was obtained at room temperature.

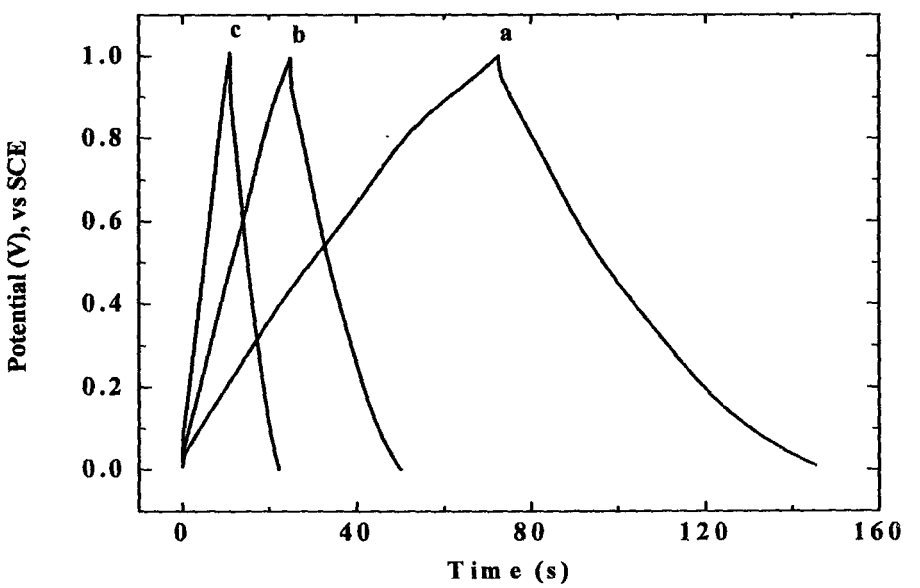

Figure 5-9 Galvanostatic charge/discharge curves for 90 μg/cm^2 as-prepared film at current densities of (a) 0.2, (b) 0.5 and (c) 1 mA/cm^2.

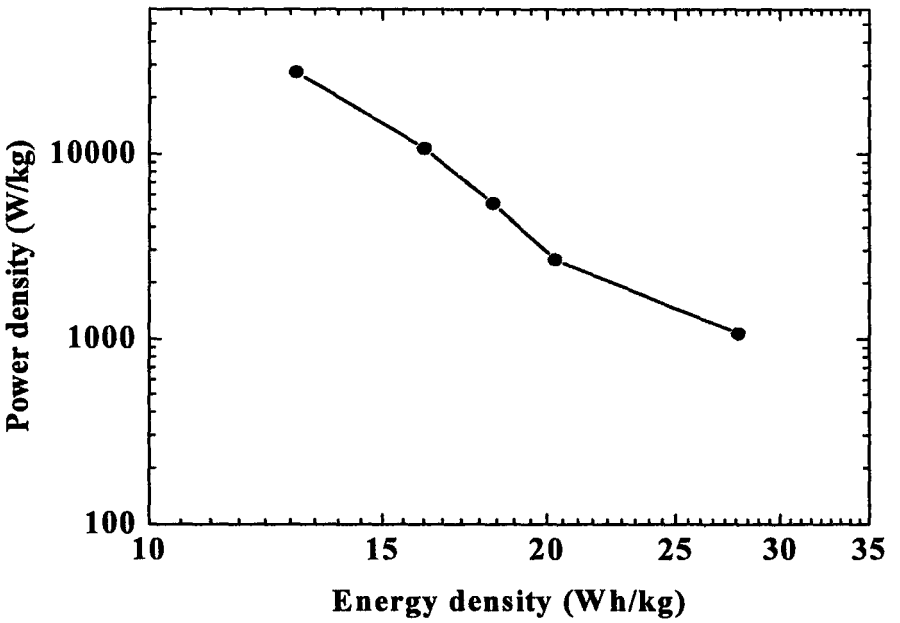

Figure 5-10 Ragone plot obtained for as-prepared 90 μg/cm² film on stainless steel

Figure 5-11 shows the equivalent circuits for a pseudocapacitance and involves the following circuit elements: the double-layer capacitance C_{dl}, a Faradaic reaction resistance R_F, corresponding to the reciprocal of the potential-dependent charge-transfer rate, a pseudocapacitance C_p, and the resistance of electrolyte R_S. At low frequency, the real part of the impedance approximately equals to the sum of R_F and R_S while at high frequency, the real part of the impedance equals to R_S.

Impedance testing was carried out to study the conductivity of deposited films (Figure 5-12). Electrolyte resistance of 14 ohm and charge-transfer resistance of 7 ohm were obtained for the as-prepared films at room temperature. T he curve of imaginary

impedance in Figure 5-13 shows capacitive behavior of the as-prepared films within the frequency range. The real part of impedance revealed relatively large equivalent series resistance (ESR).

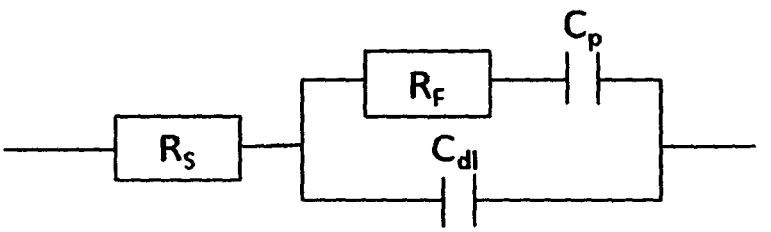

Figure 5-11 Schematic graph of an equivalent circuit of one electrode of a supercapacitor

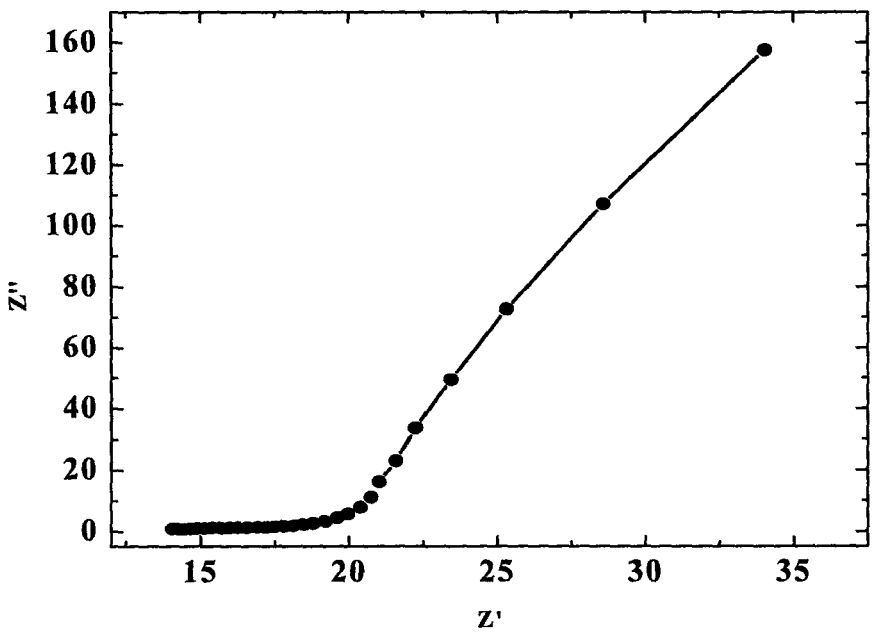

Figure 5-12 Nyquist plot of the impedance for the as-prepared 90 μg/cm^2 film obtained as a function of frequency with Z' as the real part and Z'' as the imaginary part of impedance.

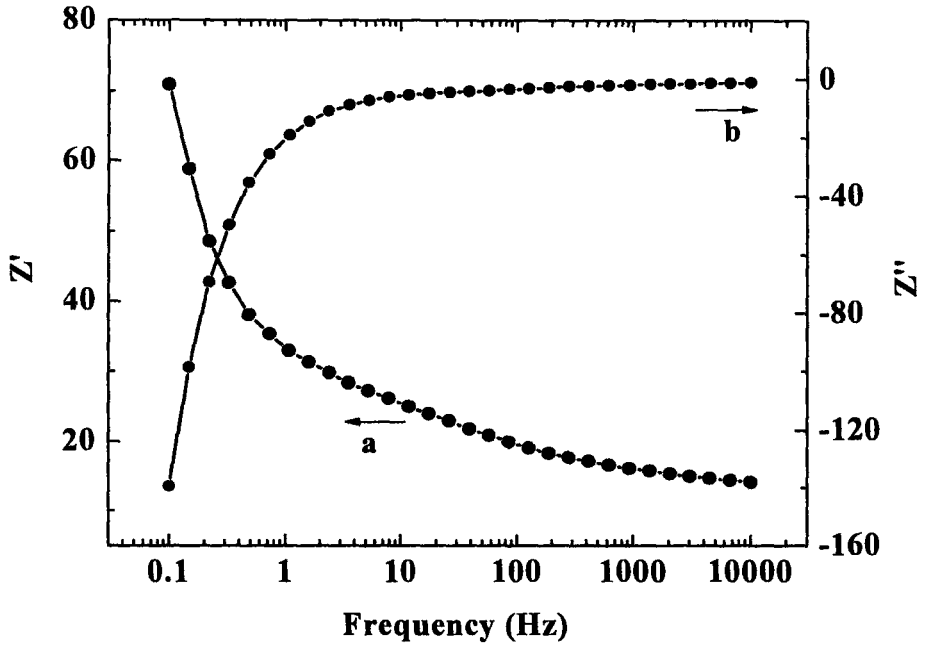

Figure 5-13 The (a) real and (b) imaginary part of impedance as a function of frequency at room temperature.

The cycling stability of the films has been investigated using CV cycling at a scan rate of 50 mV/s for 1000 cycles (Figure 5-14). A slight drop in the SC has been observed within the first 50 cycles. Then the SC remained unchanged which indicates good stability of the as-prepared electrode. The film exhibited change from their characteristic rectangular shape and showed a minor net decrease in the area of their respective CVs after 1000 cycles (Figure 5-15). No change in surface morphology was obtained in the SEM pictures after cycling (Figure 5-16), which further supported the evidence of good stability of the as-prepared electrode. The substantial change in

SC value and CV shape could be attributed to chemical degradation and partial dissolution of the films upon cycling.

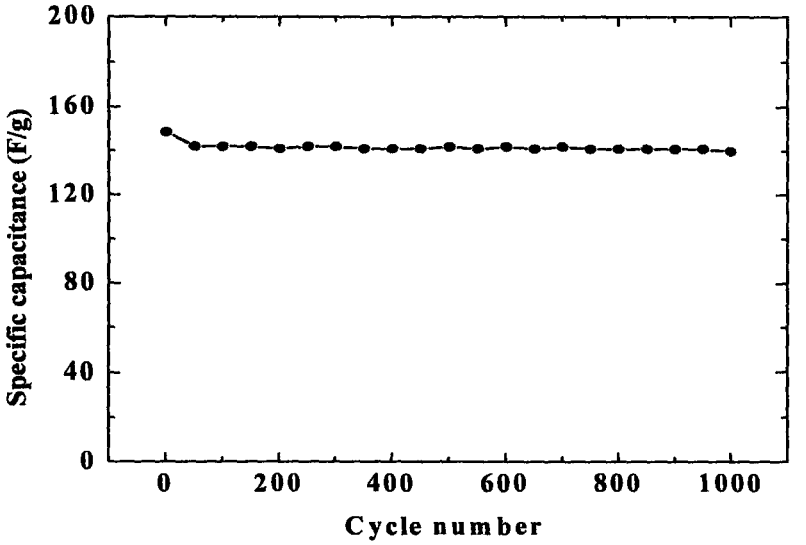

Figure 5-14 Cyclic voltammetry for the as-prepared 90 μg/cm² film up to 1000 cycles at a scan rate of 50 mV/s.

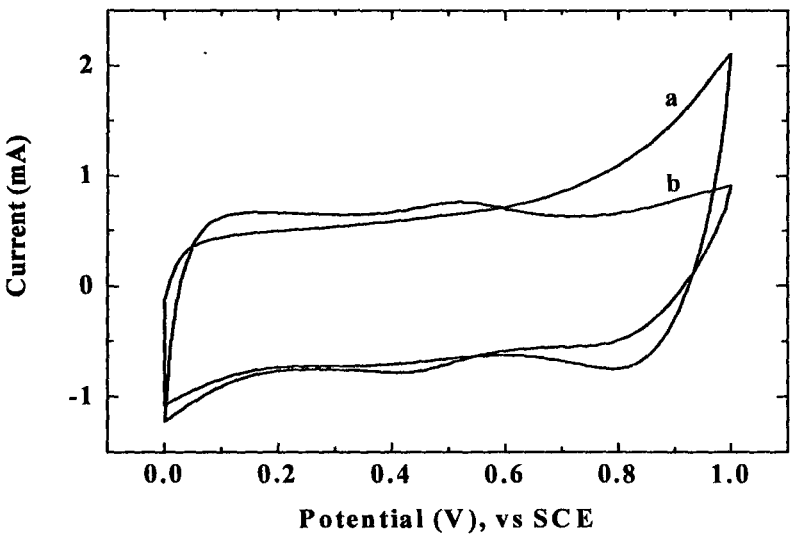

Figure 5-15 The CV window for as-prepared 90 μg/cm² film at 50 mV/s after (a) 1 and (b) 1000 cycles.

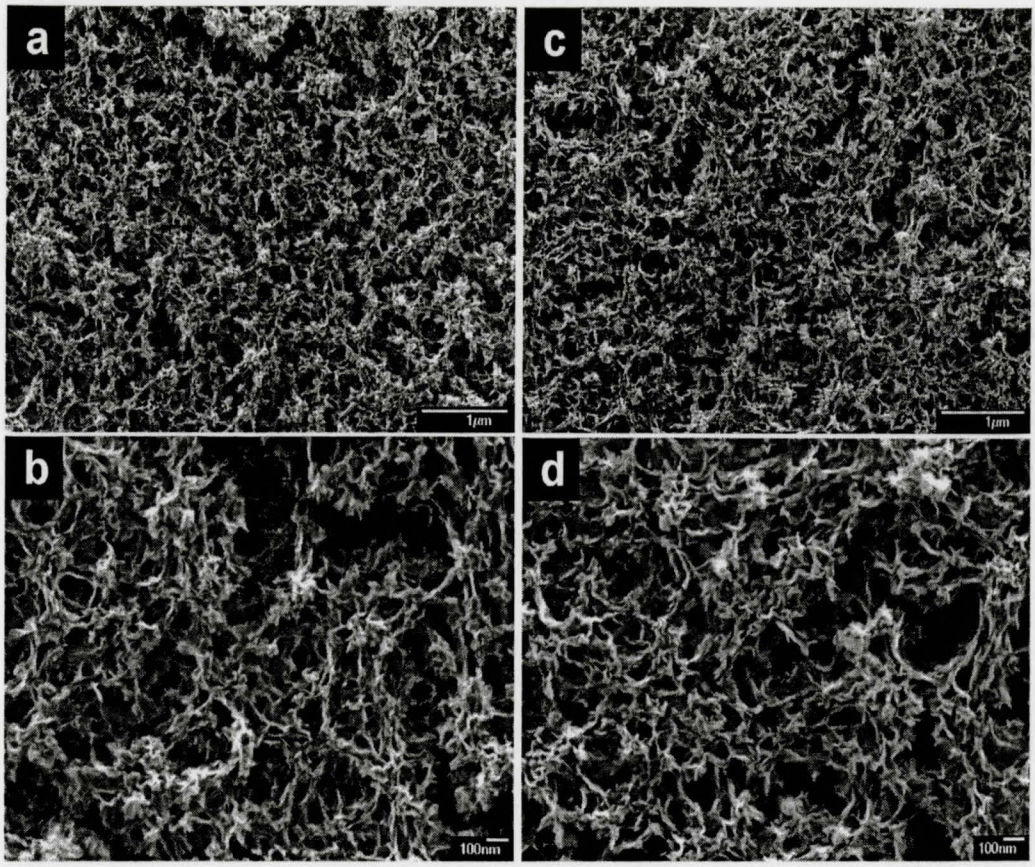

Figure 5-16 SEM pictures at different magnifications for the as-prepared 90 μg/cm^2 film (a, b) before and (c, d) after cycling.

5.1.1 Effect of film thickness

Since the deposit weight increases linearly with the deposition time, the film thickness can be easily controlled by varying the deposition time. Figure 5-17 reveals the surface morphology of the 65 μg/cm^2 films which is not as porous as the thicker films (Figure 5-6). Figure 5-18 shows CVs for 66 and 135 μg/cm^2 samples obtained at a scan rate of 10 mV/s. The calculated SCs were found to be 188 and 127 F/g for 66 and 135 μg/cm^2, respectively Figure 5-19 shows SC versus scan rate dependencies

for films of different mass. The 45 μg/cm^2 film exhibited a SC of 353 F/g at a scan rate of 2 mV/s. However, at a scan rate of 100 mV/s the SC was only 135 F/g. The difference in SC of films with different thickness may be explained in the term of conductivity Thinner film possesses higher conductivity which results in higher SC due to ion transfer This phenomenon has been further supported by the results from cycling test. Figure 5-20 shows that both the films with different thickness exhibit good stability up to 1000 cycles while higher SC was obtained for thinner film.

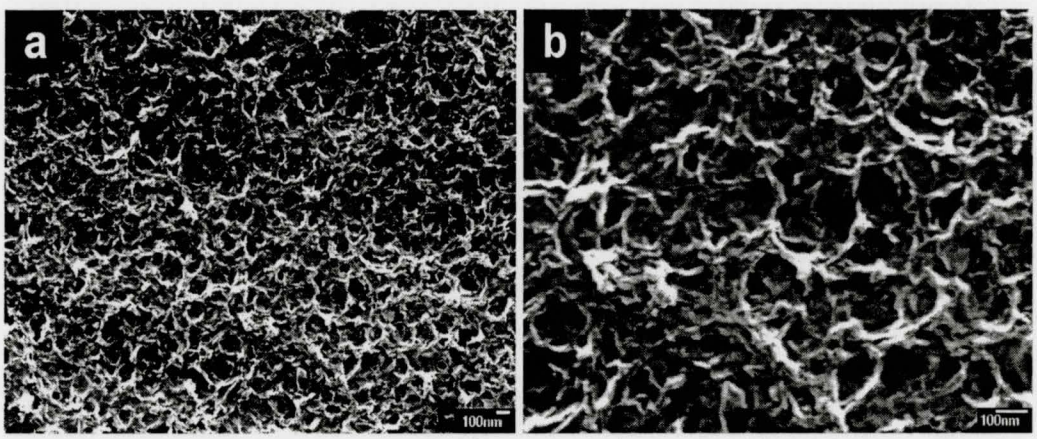

Figure 5-17 SEM pictures for the 65 μg/cm^2 samples prepared from 20 mM $KMnO_4$ solution on stainless steel.

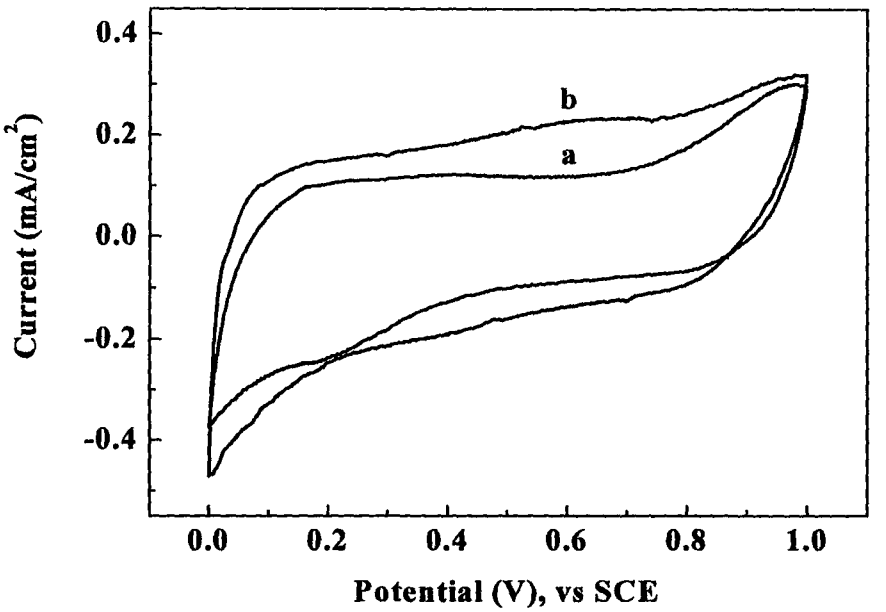

Figure 5-18 Cyclic voltammetry data for as-prepared (a) 65 and (b) 135 μg/cm² films at a scan rate of 10 mV/s.

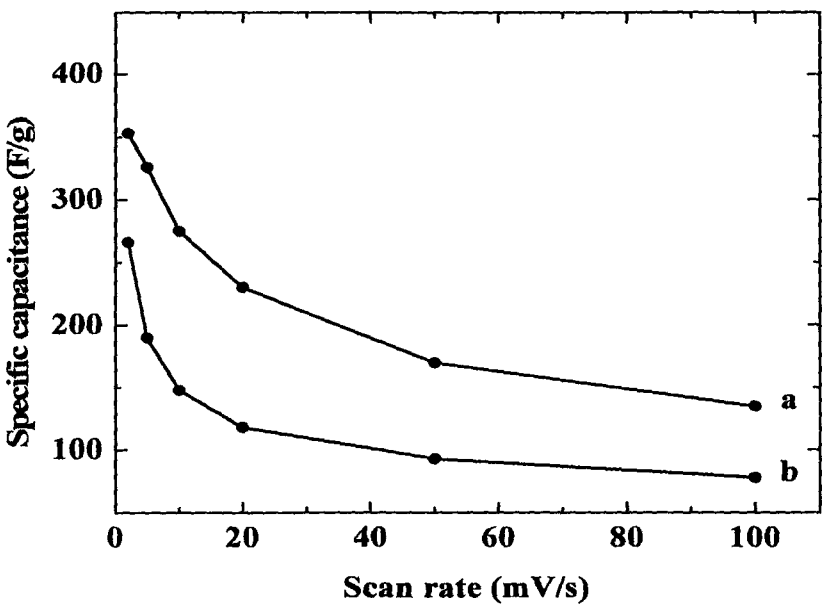

Figure 5-19 SC versus scan rate for as-prepared (a) 45 and (b) 97 μg/cm² films

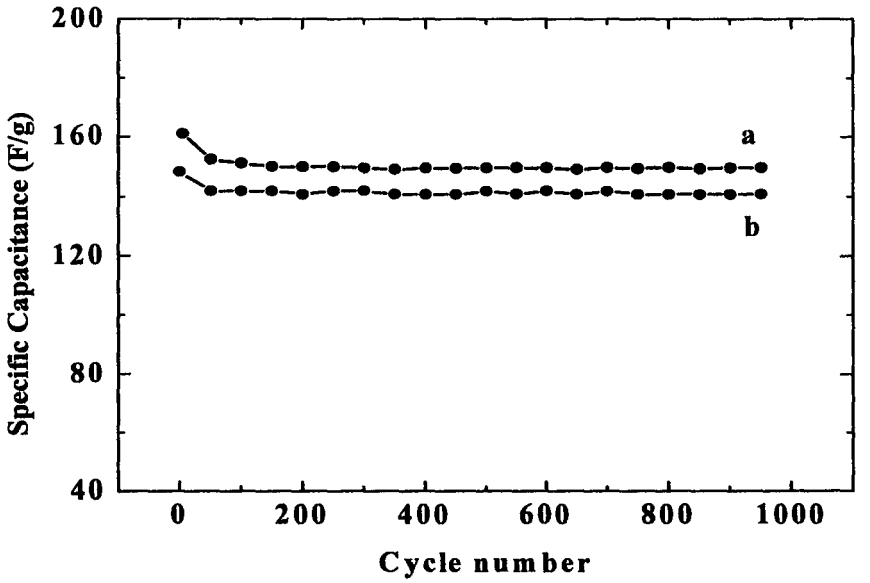

Figure 5-20 Cyclic voltammetry for the (a) 65 μ g/cm^2 and (b) 90 μg/cm^2 films at 50 mV/s prepared from 20 mM $KMnO_4$ solution on stainless steel.

5.1.2 Effect of heat treatment

Effect of heat treatment on the performance of the as-prepared electrode was investigated by carrying out cyclic voltammetry test and chronopotentiometry test on the samples after different heat treatments. Figure 5-21 and Figure 5-22 demonstrate the SC dependencies on temperatures calculated from CV and CD tests respectively. Both of the two tests showed consistent SC values and no significant influence of heat treatment was observed. There is a slight increase in SC after heat treatment which may be attributed to the weight loss due to dehydration according to Figure 5-4.

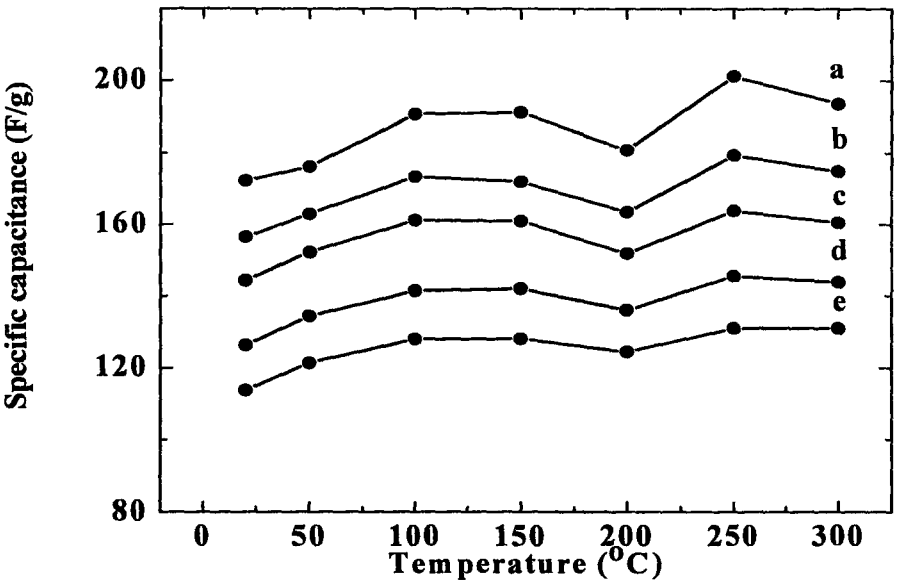

Figure 5-21 Specific capacitance versus temperature for the 90μg/cm² films at scan rates of (a) 5 mV/s, (b) 10 mV/s, (c) 20 mV/s, (d) 50 mV/s and (e) 100 mV/s.

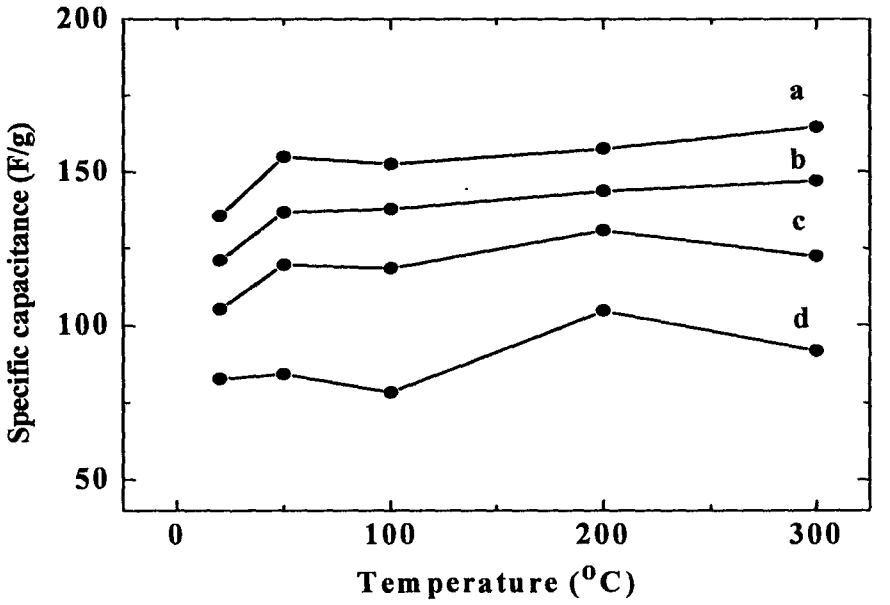

Figure 5-22 SC versus temperature for the 90 μg/cm² films calculated from CD at the current densities of (a) 0.5 mA/cm², (b) 1 mA/cm², (c) 2 mA/cm² and (d) 5 mA/cm².

SEM pictures showed no changes in surface morphology of the as-prepared samples after heat treatment up to 300°C (Figure 5-23), which is in agreement with the CV and CD results.

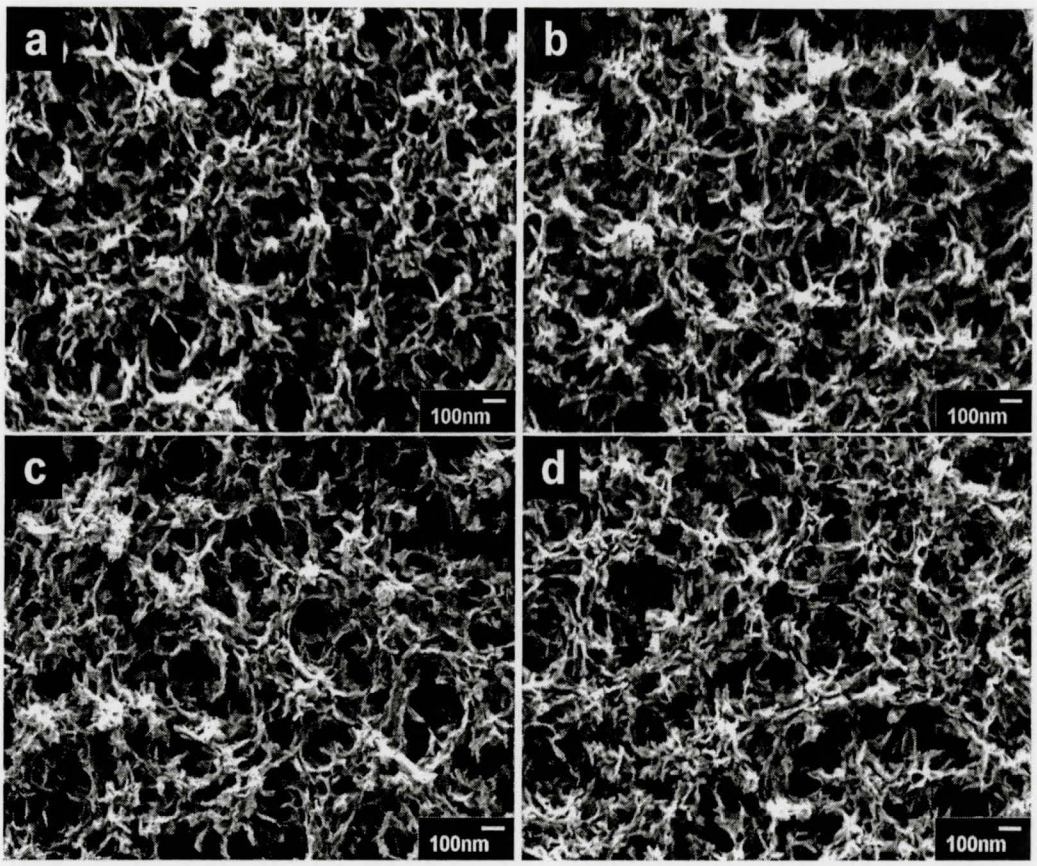

Figure 5-23 SEM pictures of 90 μg/cm^2 films (a) before and after heat treatment at (b) 100°C, (c) 200°C and (d) 300°C.

5.1.3 Effect of electrolyte

As-prepared 90 μg/cm^2 films were tested in K_2SO_4 and Na_2SO_4 aqueous solution of different concentrations in order to investigate the effect of electrolyte. No significant

difference in SC was obtained between K_2SO_4 and Na_2SO_4 electrolyte. SC values increased with the concentration of the electrolyte since more ions available for ion exchange and redox reaction.

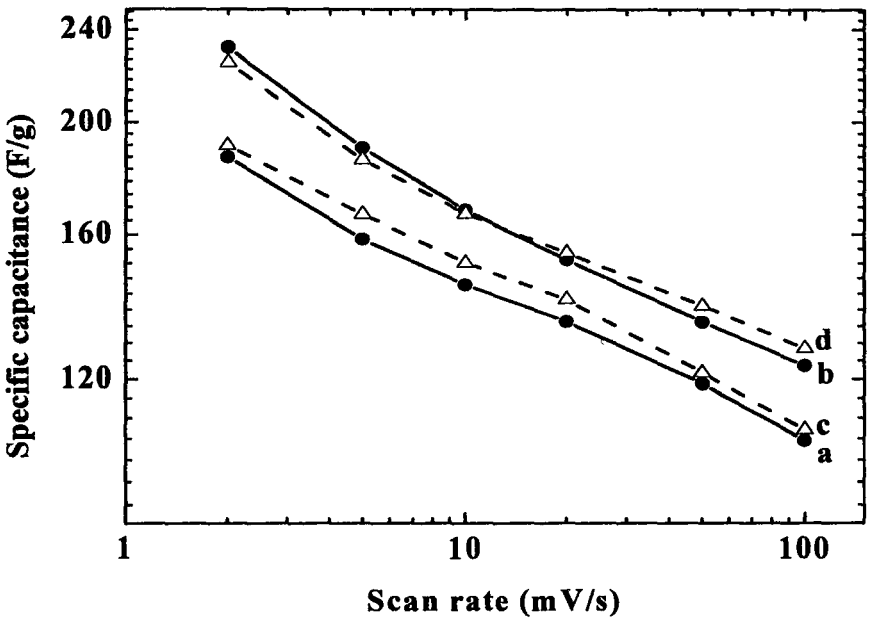

Figure 5-24 SC versus scan rate of the as-prepared 90 μg/cm² films in different electrolytes of (a) 100 mM K_2SO_4, (b) 500 mM K_2SO_4, (c) 100 mM Na_2SO_4 and (d) 500 mM Na_2SO_4 a queous solutions.

5.1.4 Effect of the concentration of deposition precursor

Different concentrations of $KMnO_4$ solution were used to prepare the manganese oxide electrode. At a constant concentration of deposition precursor, the deposit weight increases almost linearly with the deposition time (Figure 5-25). However,

higher deposition yield was obtained for the deposition solution with lower $KMnO_4$ concentration.

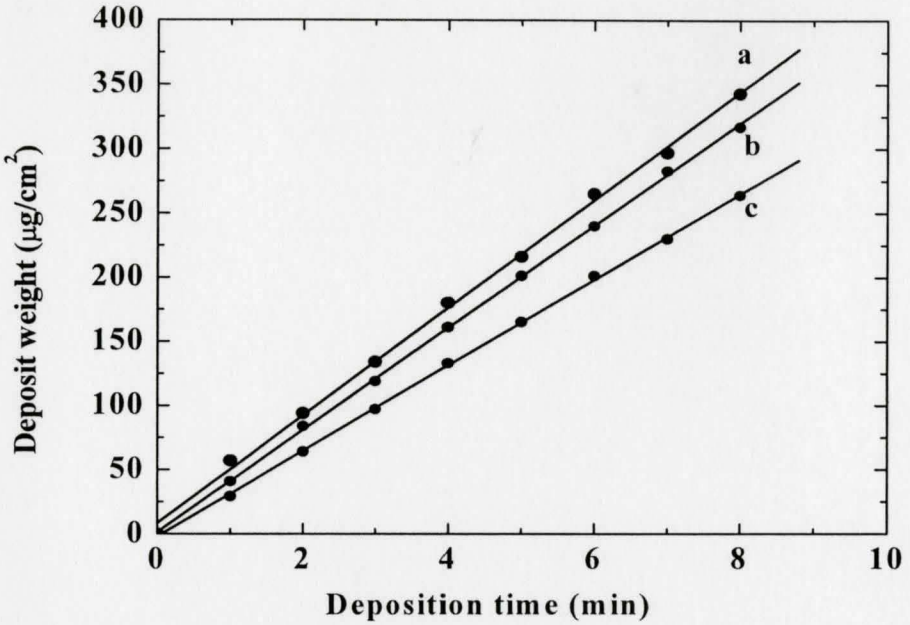

Figure 5-25 Deposit weight versus deposition time for the deposits prepared on Ni foil from (a) 20 mM, (b) 50 mM and (c) 100 mM $KMnO_4$ aqueous solution at a current density of 2 mA/cm^2

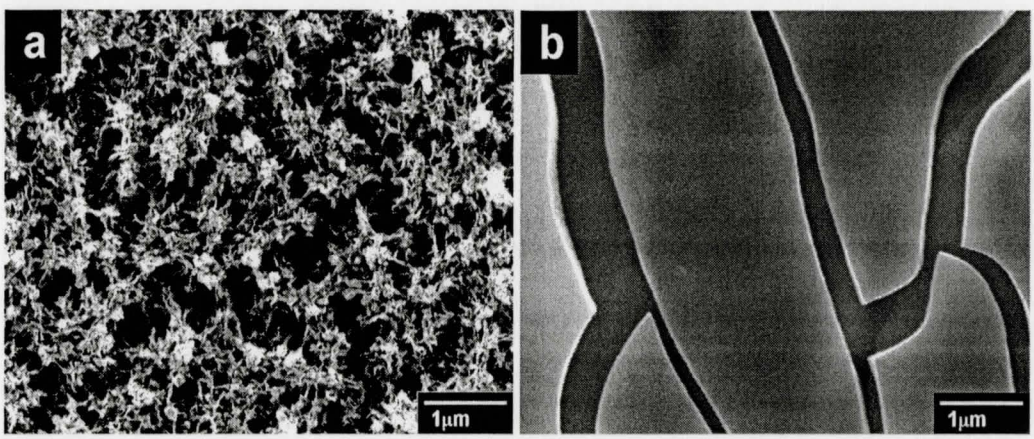

Figure 5-26 SEM pictures of films prepared on nickel foil from (a) 20 mM and (b) 100 mM $KMnO_4$ solutions.

SEM pictures in Figure 5-26 reveal highly porous structure of the electrode prepared from 20 mM $KMnO_4$. The film deposited from 100 mM $KMnO_4$ demonstrates dense microstructure with cracks. However, no significant difference was obtained in the SC values, energy density and power density between the deposits prepared from 20 mM and 100 mM $KMnO_4$ (Figure 5-27 and Figure 5-28). It will be shown below that such coatings consist of two layers: dense layer at the metal-film interface and porous or cracked top layer. Such structure can explain similar capacitive behavior of porous and cracked films.

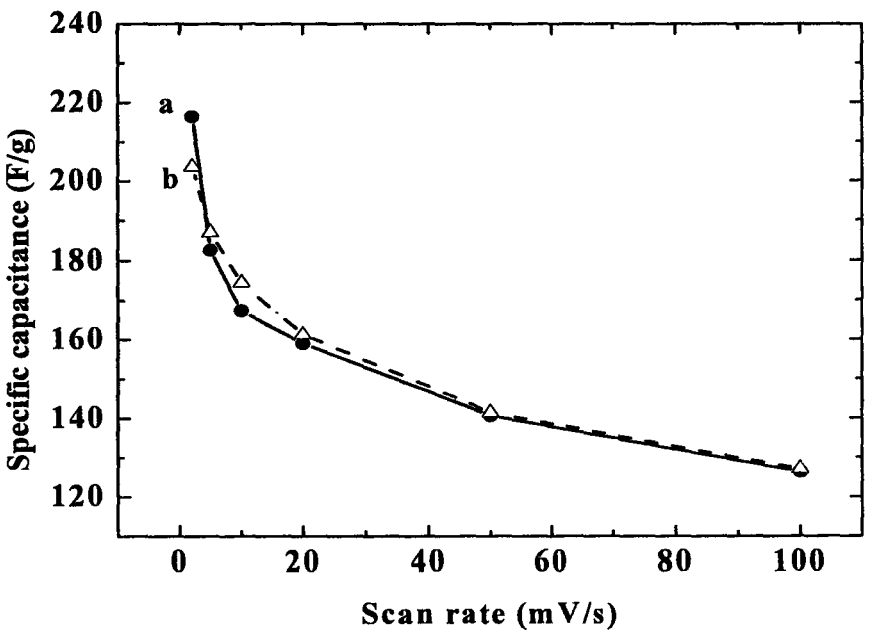

Figure 5-27 SC versus scan rate of the 90 μg/cm^2 films prepared on nickel foil from (a) 20 mM and (b) 100 mM $KMnO_4$ solution.

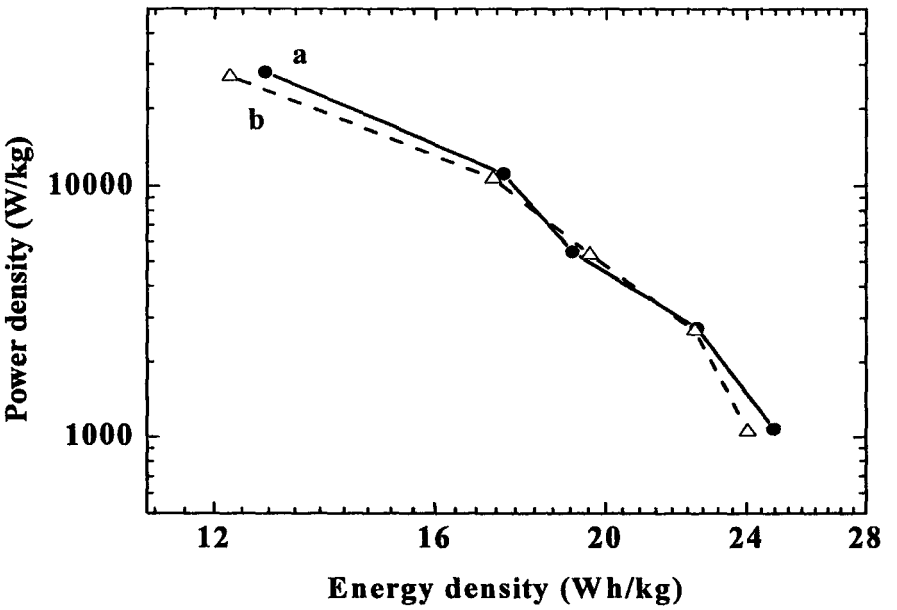

Figure 5-28 Ragone plot of the 90 μg/cm² films prepared on nickel foil from (a) 20 mM and (b) 100 mM $KMnO_4$ solution.

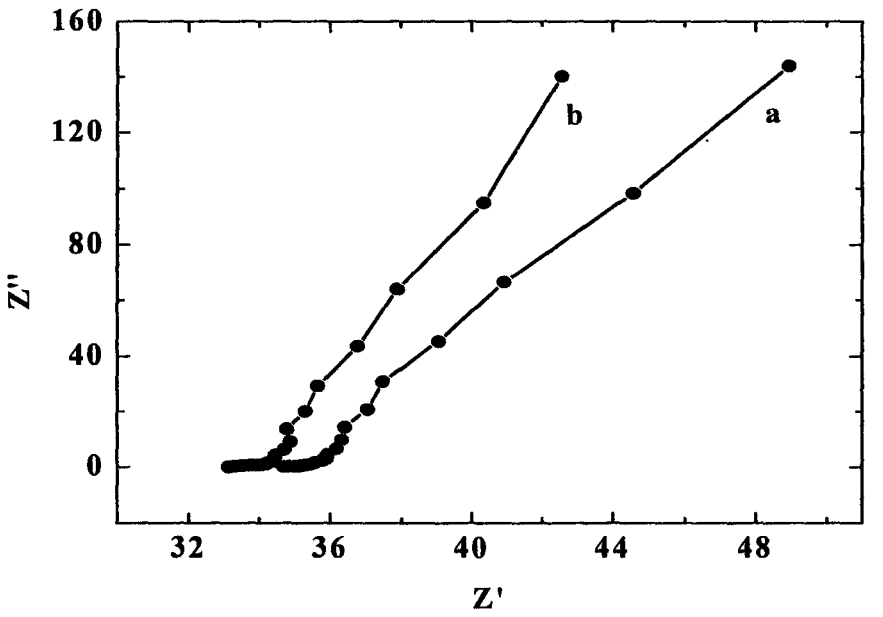

Figure 5-29 Impedance data with Z' as the real part and Z'' as the imaginary part of the 90 μg/cm² films prepared on nickel foil from (a) 20 mM and (b) 100 mM $KMnO_4$ solutions.

5.1.5 Effect of substrates

Manganese oxide films were successfully cathodically deposited and tested on different substrates, including stainless steel foil and nickel foil. Higher SC values were obtained for the films deposited on nickel foil for both of the two concentrations of deposition solution. More ideal capacitive behavior was obtained on nickel substrate with a rectangular shape of the CV window (Figure 5-32). Figure 5-33 shows the surface morphology of the films deposited on different substrates including stainless steel meshes and nickel foam which possess a much higher surface area compared to foils.

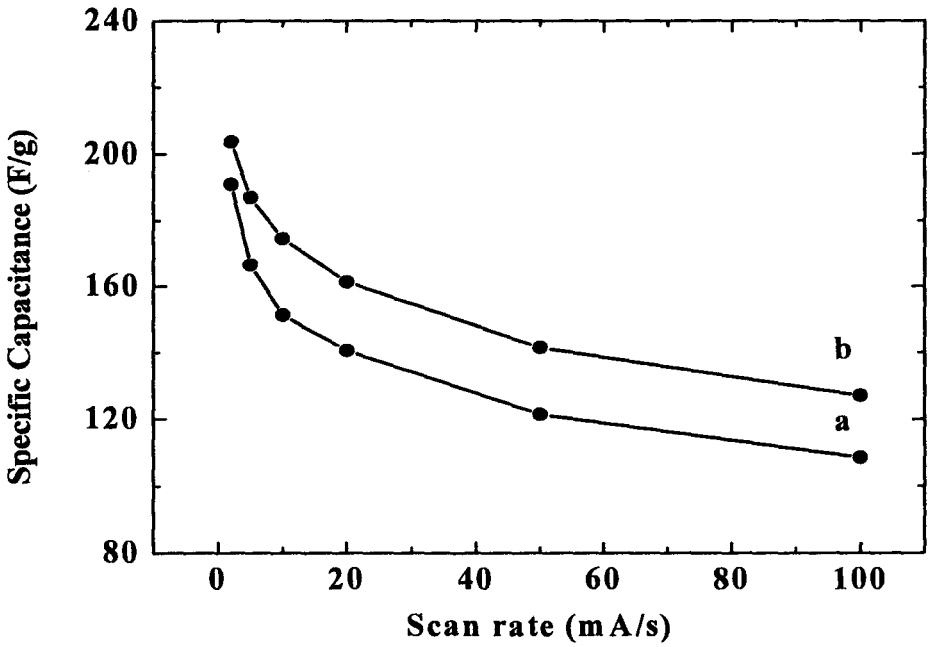

Figure 5-30 SC versus scan rate of the 90 μg/cm² films prepared from 100 mM $KMnO_4$ solution on (a) stainless steel foil and (b) nickel foil.

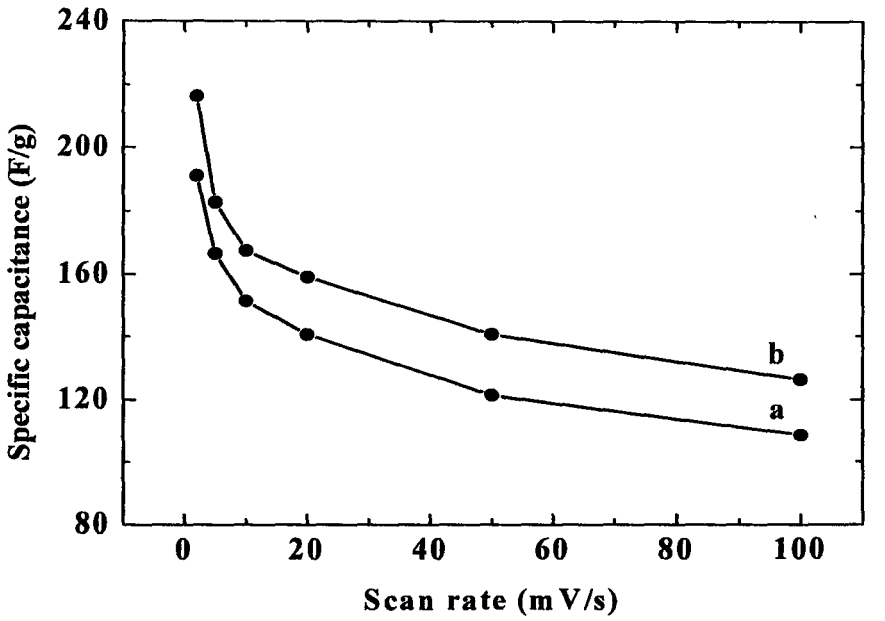

Figure 5-31 SC versus scan rate of the 90 μg/cm^2 films prepared from 20 mM $KMnO_4$ solution on (a) stainless steel foil and (b) nickel foil.

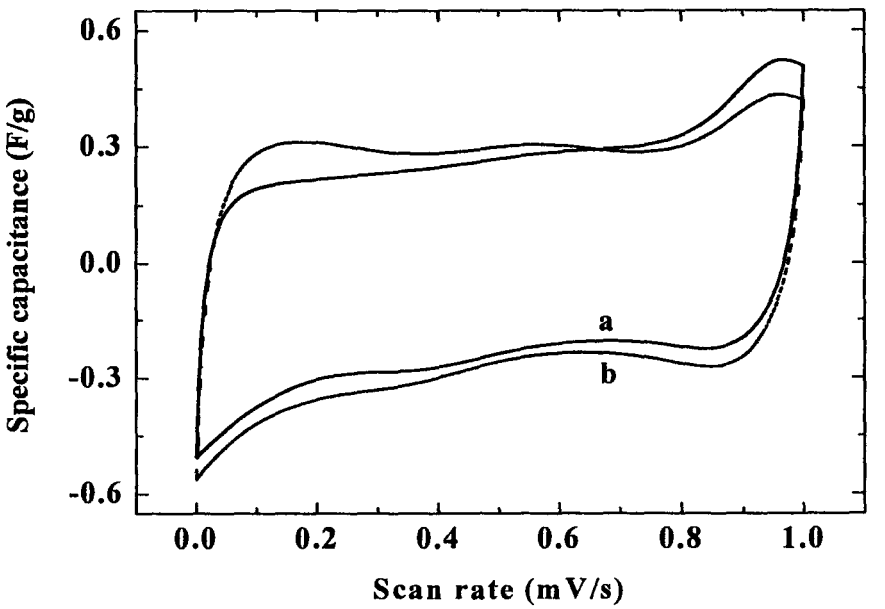

Figure 5-32 Typical CVs of the MnO_2 films deposited from 20 mM $KMnO_4$ solution on (a) stainless steel and (b) nickel foil.

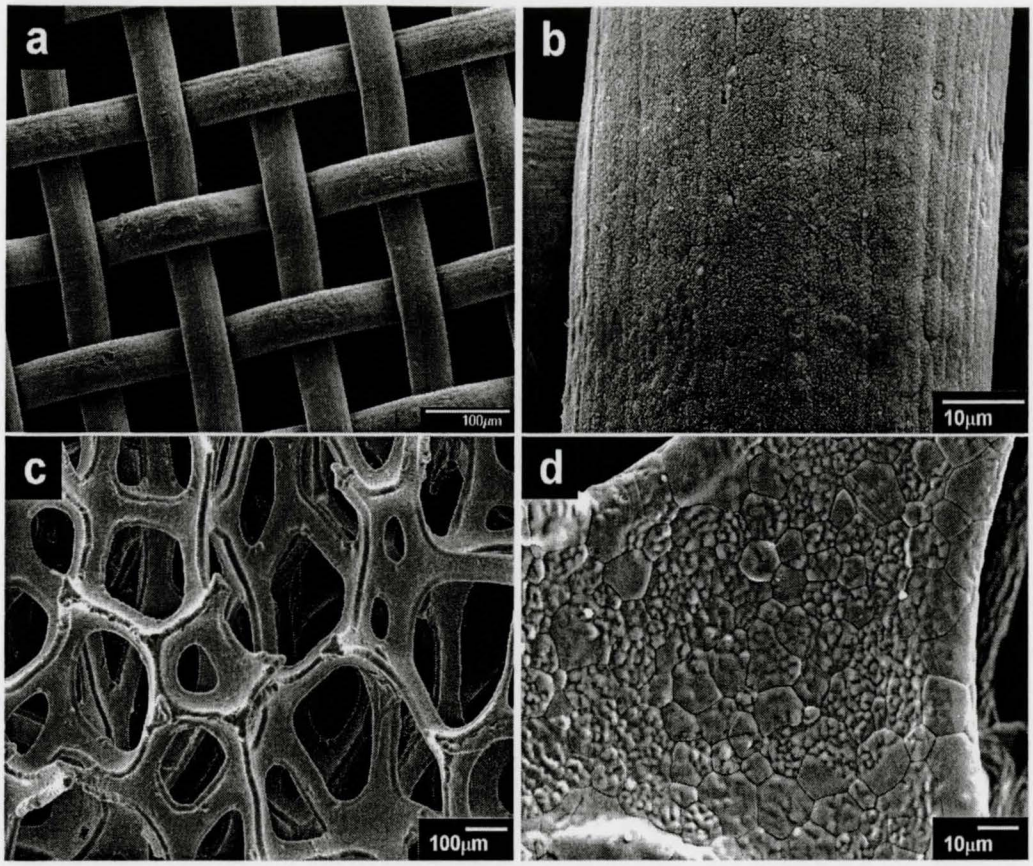

Figure 5-33 SEM pictures at different magnifications for the deposits obtained from the 20 mM $KMnO_4$ aqueous solutions (a, b) on the stainless steel meshes and (c, d) nickel foam at a current density of 2 mA/cm^2

5.2 Electrodeposition from $NaMnO_4$ solutions

The experimental data presented in Figure 5-34 indicates that the deposit weight increases linearly with the deposition time and higher deposition yield was obtained using 20 mM $NaMnO_4$ solutions compared to the 100 mM $NaMnO_4$ solutions. This is in good agreement with the results obtained for $KMnO_4$ solutions. Figure 5-34 shows a linear sweep voltammogram for a gold coated quartz crystal electrode in the 20 mM $NaMnO_4$ solution. The observed broad maximum in the current versus potential curve

can be attributed to the reduction of $NaMnO_4$. As the electrode potential approached the potential region of the maximum, the surface of the electrode turned black due to the deposition of manganese oxide. QCM studies showed mass increase related to the formation of a cathodic deposit.

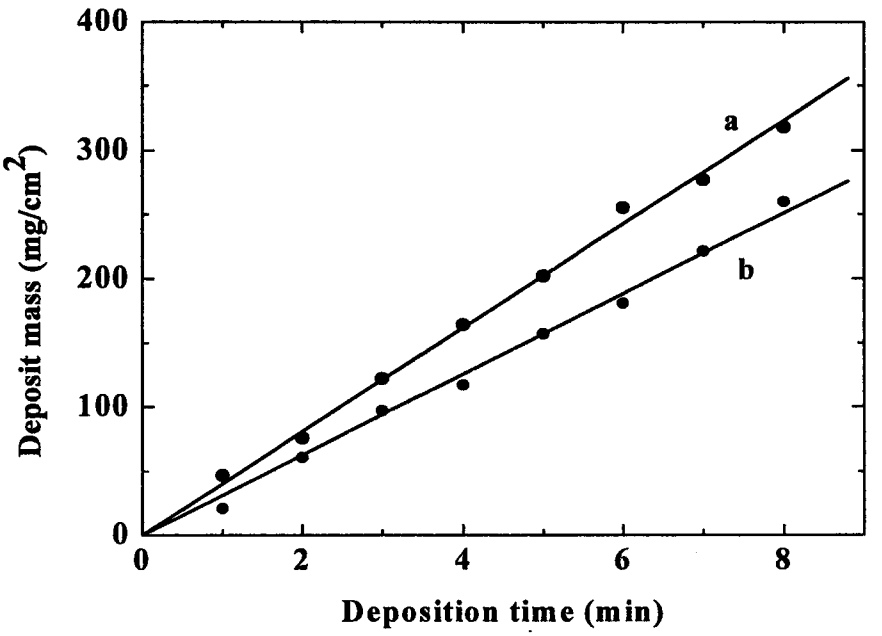

Figure 5-34 Deposit weight versus deposition time for deposits prepared on Ni foil from (a) 20 mM, and (b) 100 mM $NaMnO_4$ aqueous solution at a current density of 2 mA/cm^2.

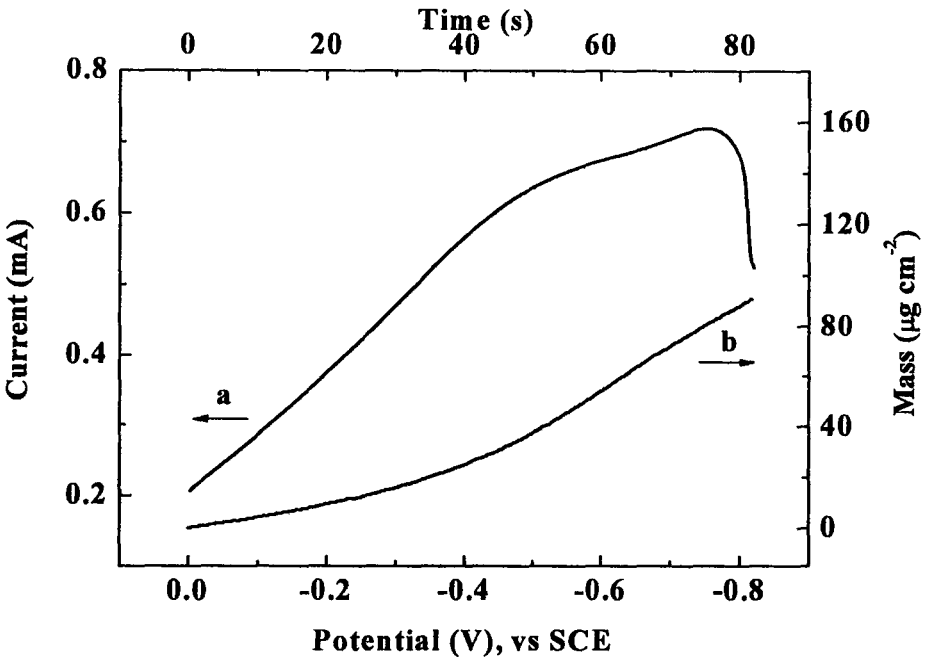

Figure 5-35 (a) Linear sweep voltammogram for a gold coated quartz crystal electrode in the 20 mM $NaMnO_4$ aqueous solution at a scan rate of 10 mVs^{-1} and (b) the corresponding deposit mass versus deposition time dependence obtained using QCM.

X-ray studies revealed different crystallization behavior of the deposits prepared from the 20 mM and 100 mM $NaMnO_4$ solutions. The XRD studies of the films prepared from the 20 mM $NaMnO_4$ solutions (

Figure 5-36) indicate the formation of a birnessite phase at room temperature (JCPDS file 43-1456) and dehydrated birnessite after heat treatment at 200°C for 1 hour. At higher temperatures the transformation from birnessite to the cryptomelane phase (JCPDS file 44-1386) was observed. In contrast, the X-ray studies of the deposits prepared from the 100 mM $NaMnO_4$ solutions (

Figure 5-37) showed their amorphous nature at temperatures below 400 °C. At higher temperatures the formation of the cryptomelane phase was observed.

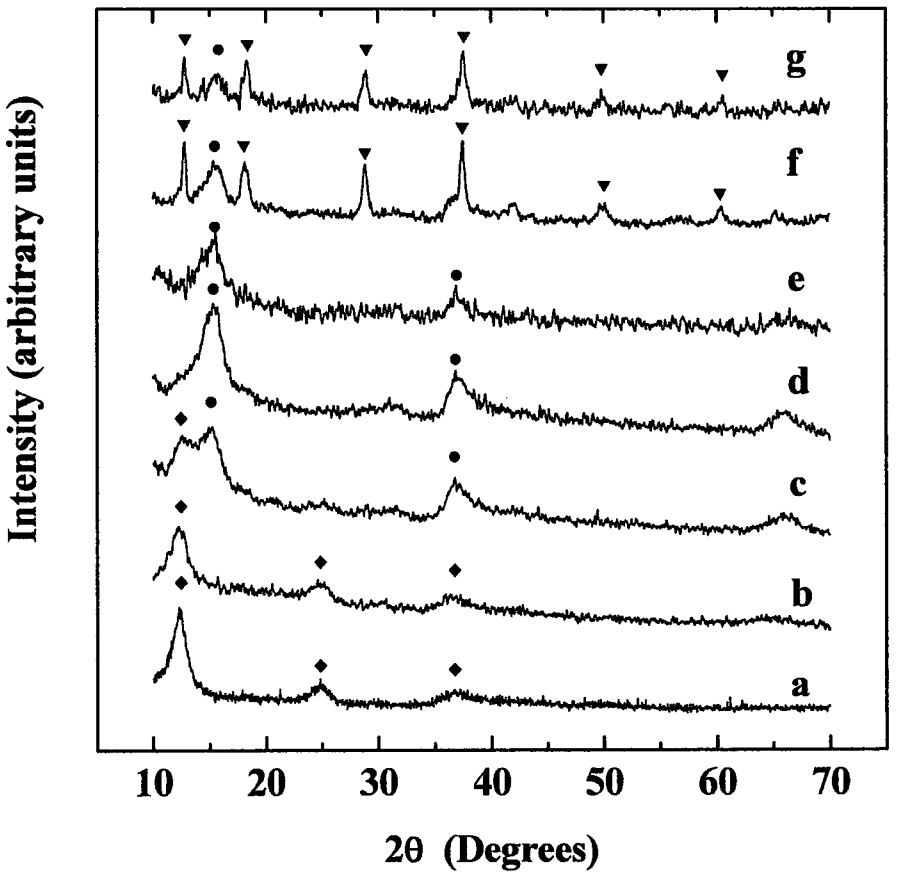

Figure 5-36 X-ray diffraction patterns for the deposits obtained from the 20 mM $NaMnO_4$ aqueous solution: (a) as prepared and after heat treatment at (b) 100°C, (c) 200°C, (d) 300°C, (e) 400°C, (f) 500°C, (g) 600°C (♦- birnessite, • – dehydrated form of birnessite, ▼– cryptomelane)

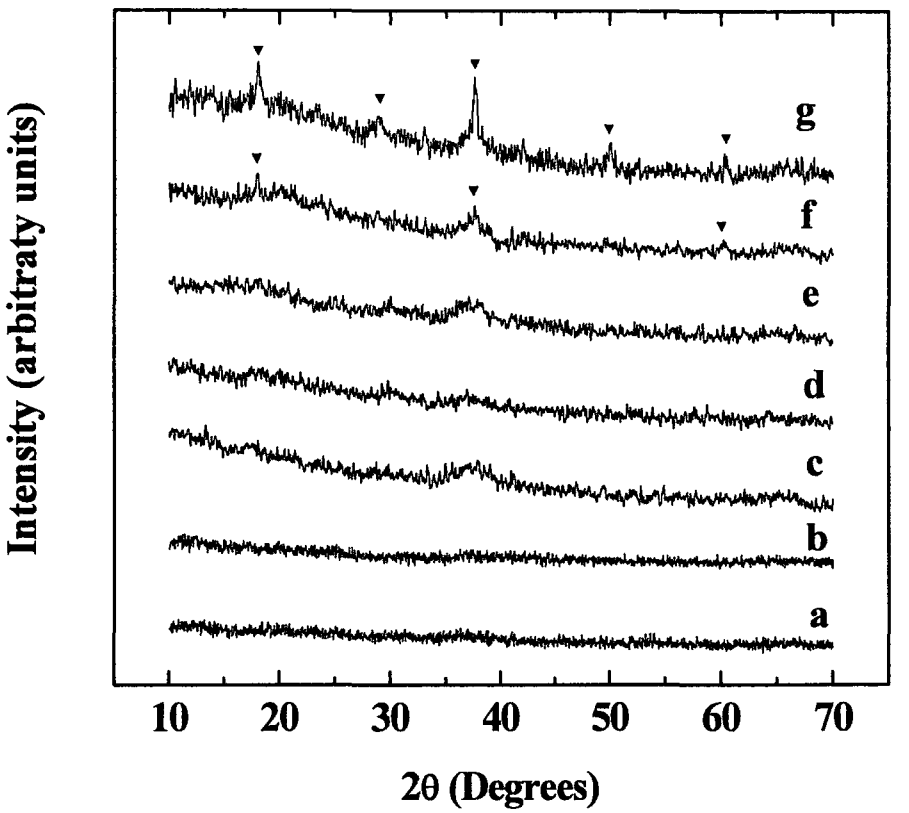

Figure 5-37 X-ray diffraction patterns for the deposits obtained from the 100 mM $NaMnO_4$ aqueous solution: (a) as prepared and after heat treatment at (b) 100°C, (c) 200°C, (d) 300°C, (e) 400°C, (f) 500°C, (g) 600°C (▼– cryptomelane).

EDS studies showed that the deposits contained Na and Mn species. Typical EDS data for as-prepared deposits are presented in Figure 5-38. Numerous EDS analyses showed a Mn/Na atomic ratio of 4.14±0.04 and 7.40±0.05 for the films prepared from the 20 mM $NaMnO_4$ and 100 mM $NaMnO_4$ solutions, respectively.

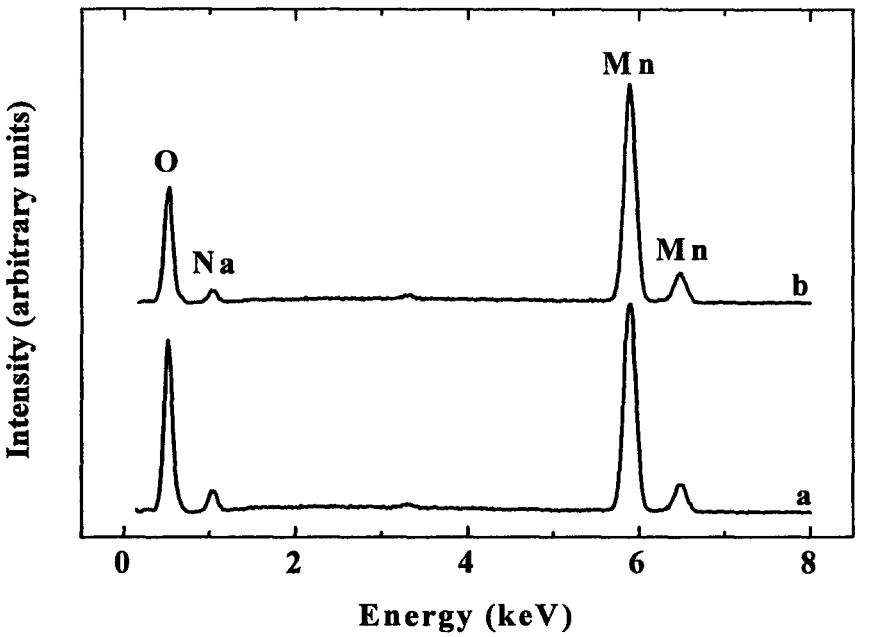

Figure 5-38 EDS data for the deposits prepared from (a) 20 mM $NaMnO_4$ solution (b) 100 mM $NaMnO_4$ solution.

Obtained deposits were studied by TGA and DTA. TGA data showed a sharp reduction in sample weight below ~ 200 °C, which can be attributed to deposit dehydration (Figure 5-39). The DTA data showed corresponding endotherms in the range of ~100-150 °C (Figure 5-39). The weight loss at higher temperatures can be attributed to the thermal dehydration of the deposits and partial reduction of Mn species. The total weight loss at 1200 °C was found to be 21.9 and 23.7 wt% for deposits prepared from 20 mM and 100 mM $NaMnO_4$, respectively.

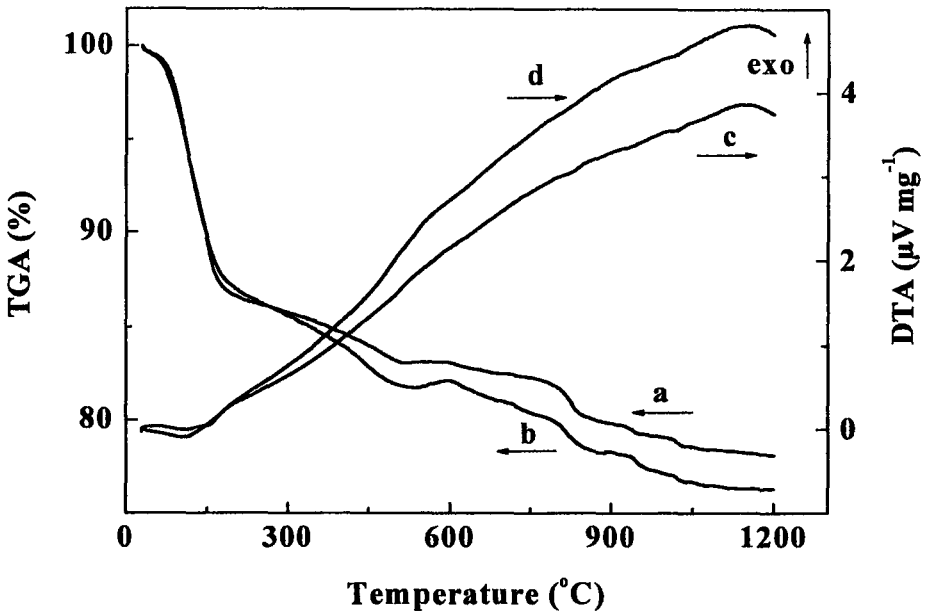

Figure 5-39 (a, b) TGA and (c, d) DTA data for deposits prepared from (a, c) the 20 mM $NaMnO_4$ solution and (b, d) the 100 mM $NaMnO_4$ solution.

Figure 5-40 compares the SEM images of the deposits prepared from the 20 mM and 100 mM $NaMnO_4$ solutions. The deposits prepared from the 20 mM $NaMnO_4$ solutions exhibited a porous microstructure with typical pore size of about 100-200 nm. Under high magnification (Figure 5-40c), the surface structure is composed of nanowhiskers with typical length of ~100 nm. In contrast, the films prepared from the 100 mM $NaMnO_4$ solutions showed a "cracked-mud" morphology[75], which consisted of dense islands separated by cracks. Again, this phenomenon is in good agreement with the results obtained from $KMnO_4$ aqueous solutions.

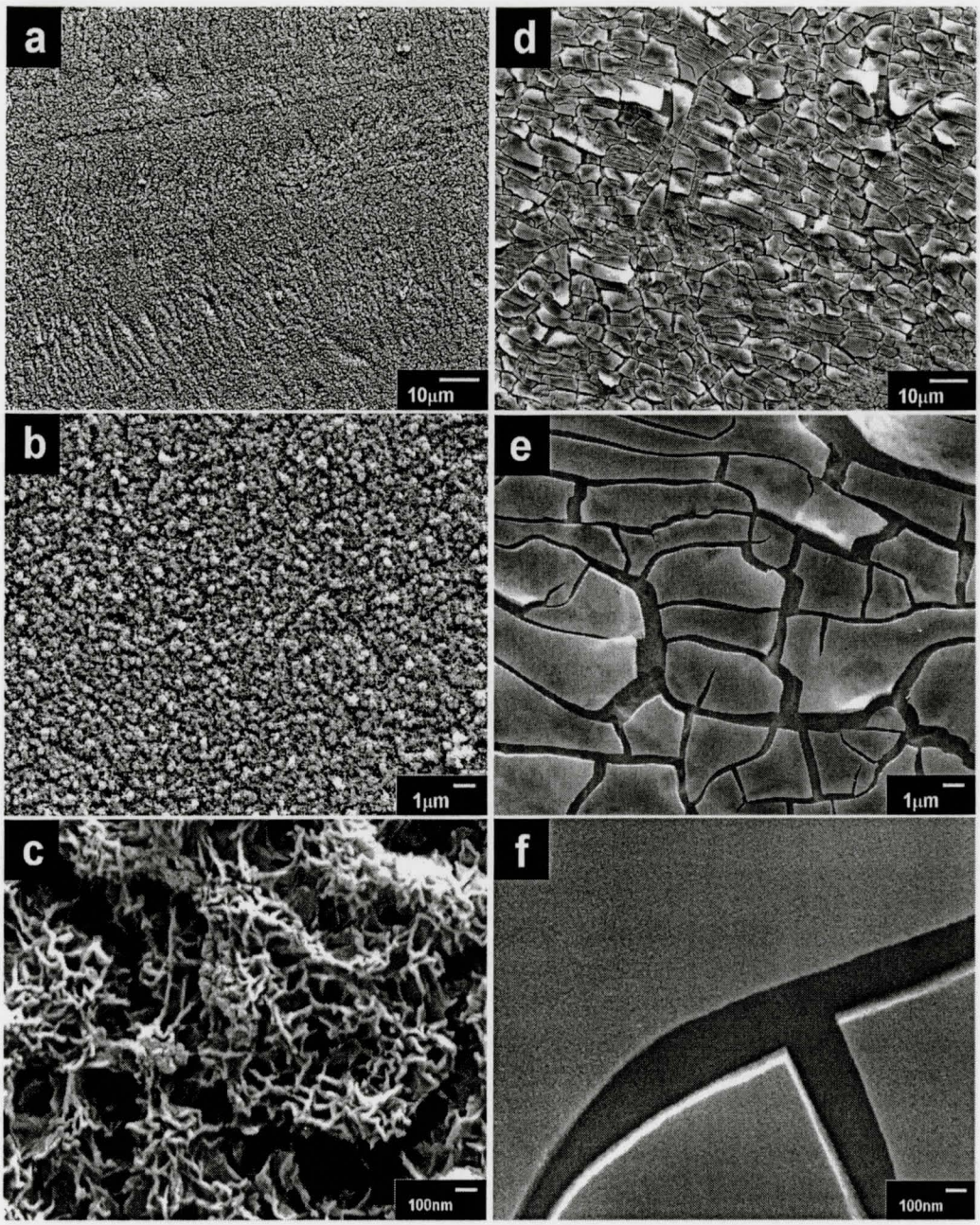

Figure 5-40 SEM pictures of films at different magnifications prepared from (a, b, c) the 20 mM $NaMnO_4$ solution and (d, e, f) the 100 mM $NaMnO_4$ solution at a current density of 2 mA/cm^2 and deposition time of 2 min.

The investigations of the films prepared from the 20 mM $NaMnO_4$ solutions showed changes in microstructure with increasing film thickness. Figure 5-41 compares microstructures of films of different mass prepared from the 20 mM $NaMnO_4$ solutions. The SEM observations of the surface of the 50 $\mu g/cm^2$ film showed denser microstructure compared to that of the 90 $\mu g/cm^2$ film. This is in a good agreement with the results of SEM investigations of the film cross sections. The result indicates that deposits consist of relatively dense bottom layer and porous top layer. Film growth resulted in an increasing thickness of the both layers. As an example, Figure 5-42 shows a cross section of a 400 $\mu g/cm^2$ film removed from the Ni substrate. The thickness of the layers is about 2 μm. It is important to note that two layer microstructure of the deposits prepared by cathodic electrosynthesis has been also reported in the literature for the zirconia films[75]. However, both layers exhibited cracking and contained islands of dense nanostructured zirconia.

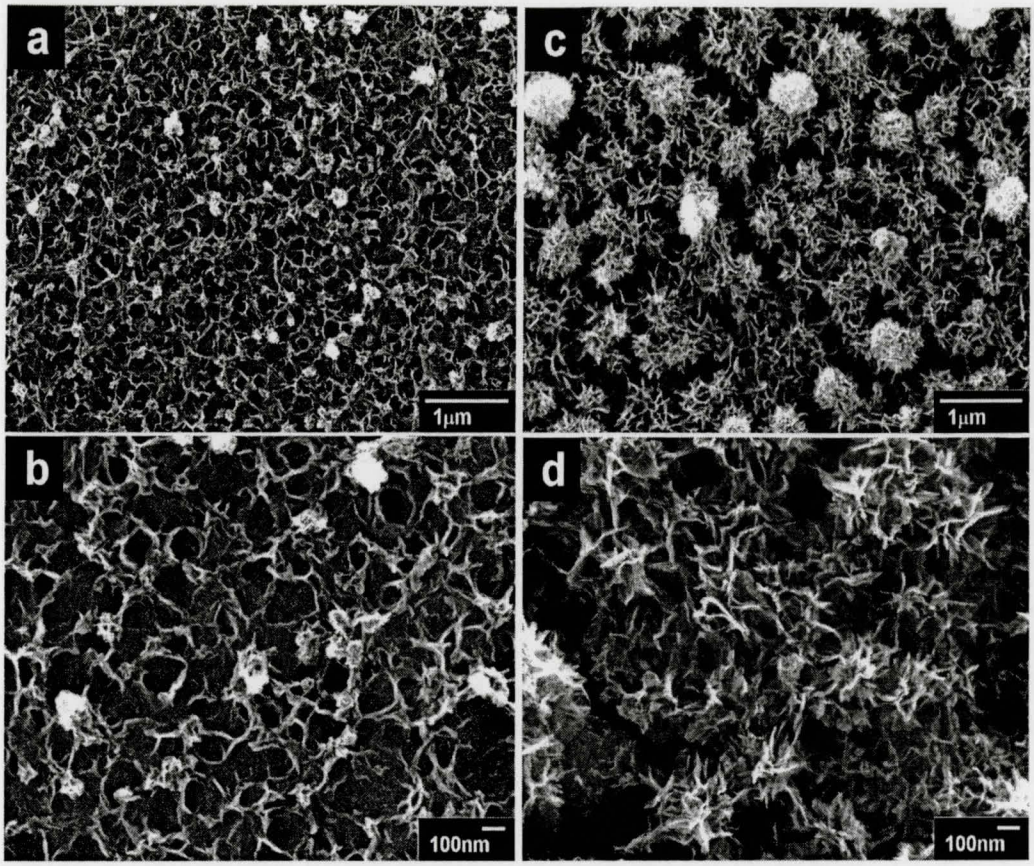

Figure 5-41 SEM pictures at different magnifications for films of different mass: (a, b) 50 μg/cm^2 and (c, d) 90 μg/cm^2, prepared from the 20 mM $NaMnO_4$ aqueous solutions.

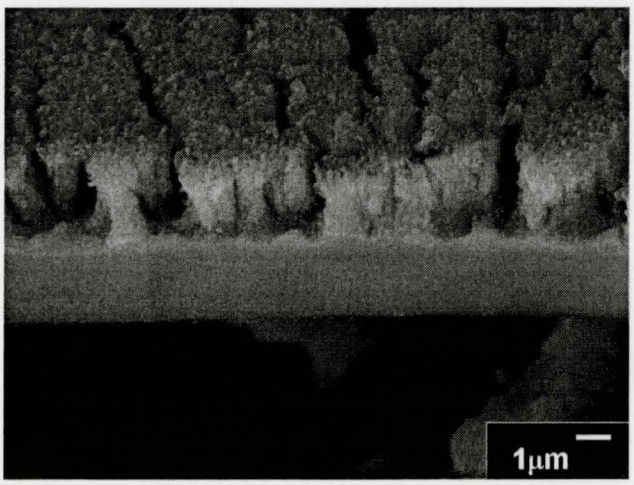

Figure 5-42 SEM picture of a cross section of a film prepared from the 20 mM $NaMnO_4$ aqueous solution at a current density of 2 mA/cm^2

The capacitive behavior of the films prepared from the 20 mM $NaMnO_4$ solutions was investigated in the potential range of 0-1.0 V versus SCE. Figure 5-43 shows typical CVs for the 90 $\mu g/cm^2$ sample in the 100 mM Na_2SO_4 solutions. Within the potential range of 0-1.0 V versus SCE the manganese oxide electrodes exhibited capacitive-like current-potential responses. It is clear from Figure 5-43 that there are no redox peaks in the range between 0 and 1.0 V. More ideal behavior was obtained for the films deposited from 100 mM $NaMnO_4$ than that from 20 mM $NaMnO_4$ solution (Figure 5-44).

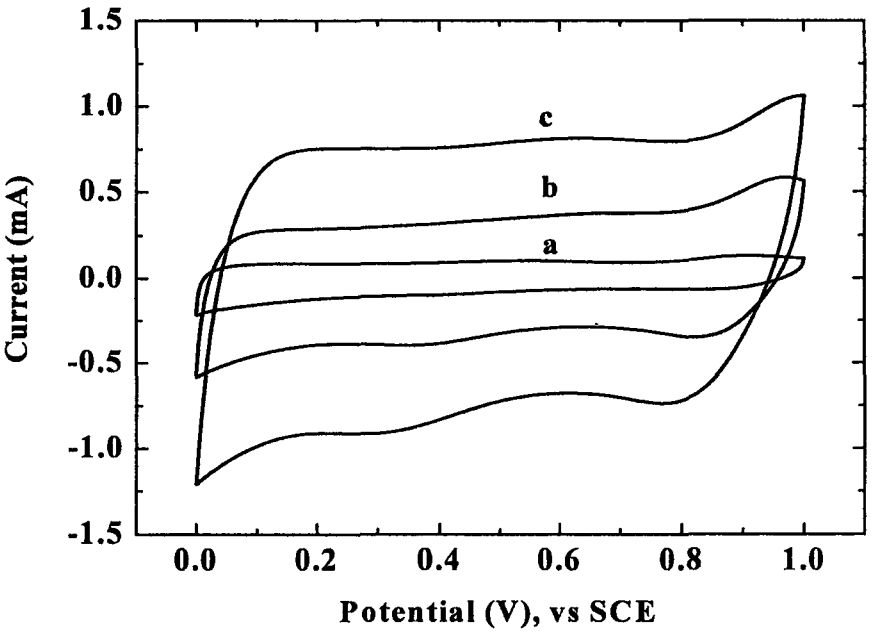

Figure 5-43 Cyclic voltammetry of as-prepared 95 $\mu g/cm^2$ film deposited on nickel from 20 mM $NaMnO_4$ solution at the scan rate of (a) 5 mV/s, (b) 20 mV/s, and (c) 50 mV/s.

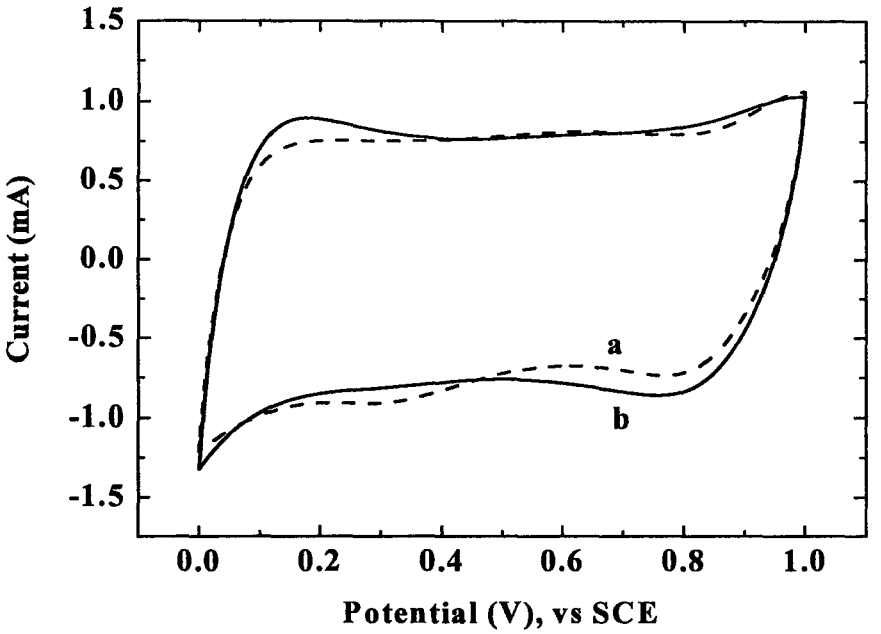

Figure 5-44 Cyclic voltammetry of as-prepared 95 μg/cm^2 film deposited on nickel from (a) 20 mM and (b) 100 mM $NaMnO_4$ solutions.

5.2.1 Effect of substrates

The effect of substrates was investigated by comparing the film performance on stainless steel and nickel foil. Higher SC was obtained on nickel substrates as shown in Figure 5-45, which can be attributed to the higher conductivity at the interface between the films and substrates on nickel foil (Figure 5-46). The impedance data at high frequency shows a semicircular arc for the films deposited on stainless steel which demonstrates the presence of the parallel arrangement of a charge-transfer resistance and a double-layer capacitance.

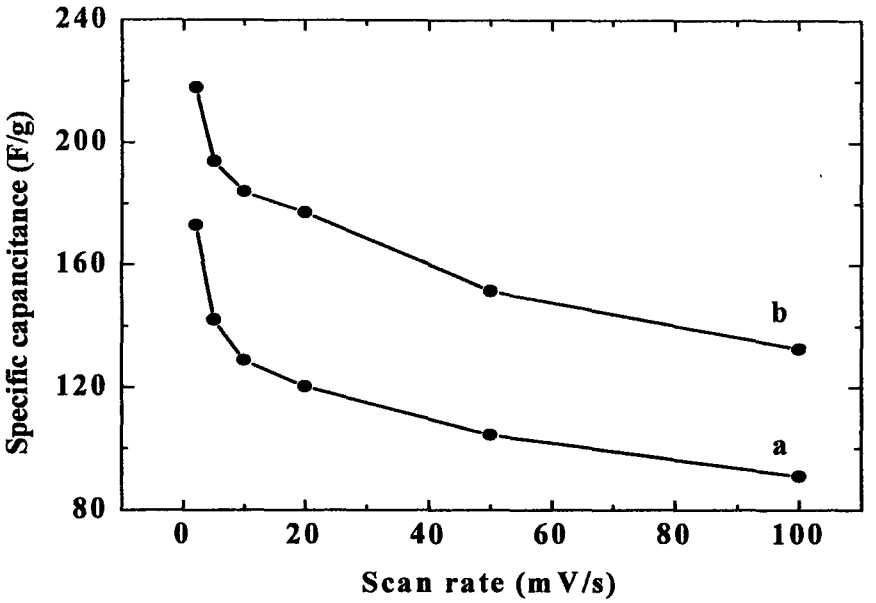

Figure 5-45 SC vs. scan rate for as-prepared 90 μg/cm^2 films deposited from 20 mM $NaMnO_4$ on (a) stainless steel and (b) nickel foil .

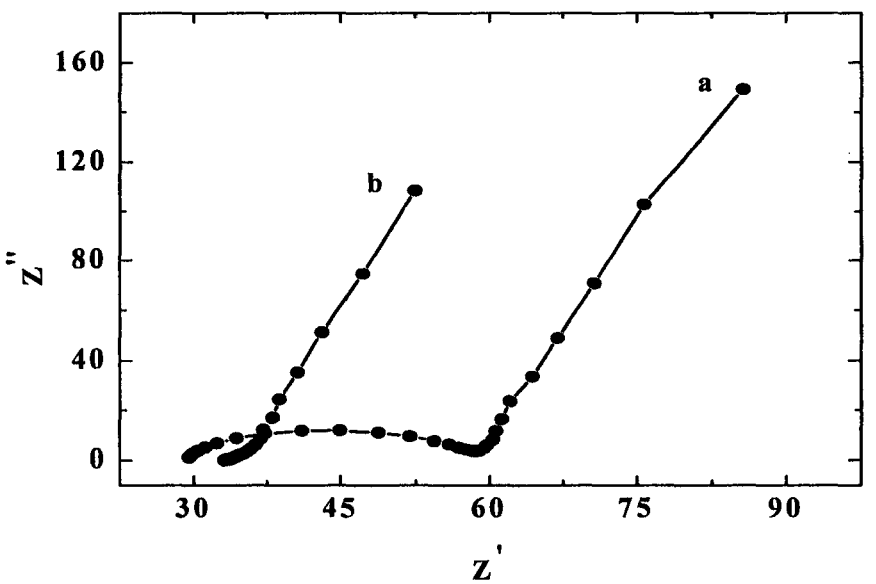

Figure 5-46 Impedance data with Z' as the real part and Z'' as the imaginary part for the 90 μg/cm^2 films prepared from 20mM $NaMnO_4$ solution on (a) stainless steel and (b) nickel foil.

5.2.2 Effect of deposition precursor

After investigating the influence of substrates on electrochemical supercapacitors, the performance of electrodes prepared from different deposition precursor was also studied. Higher SCs were obtained on stainless steel for the films deposited from $KMnO_4$ aqueous solution (Figure 5-47) and on nickel for the films deposited from $NaMnO_4$ solutions (Figure 5-49) which are attributed to the corresponding lower resistance at the interface as shown in Figure 5-48 and Figure 5-50.

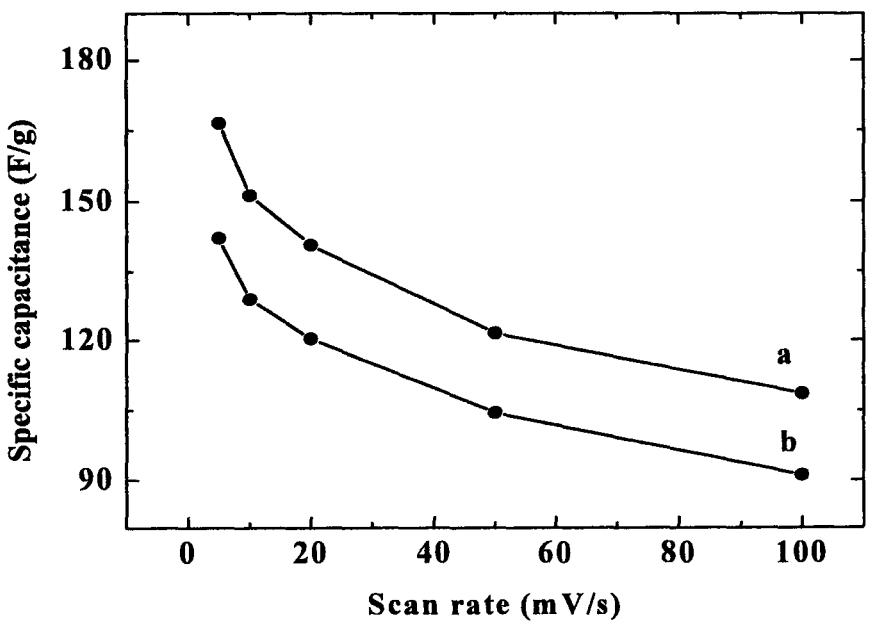

Figure 5-47 SC versus scan rate of the 90 μg/cm^2 films prepared on stainless steel from 20 mM (a) $KMnO_4$ and (b) $NaMnO_4$ aqueous solution.

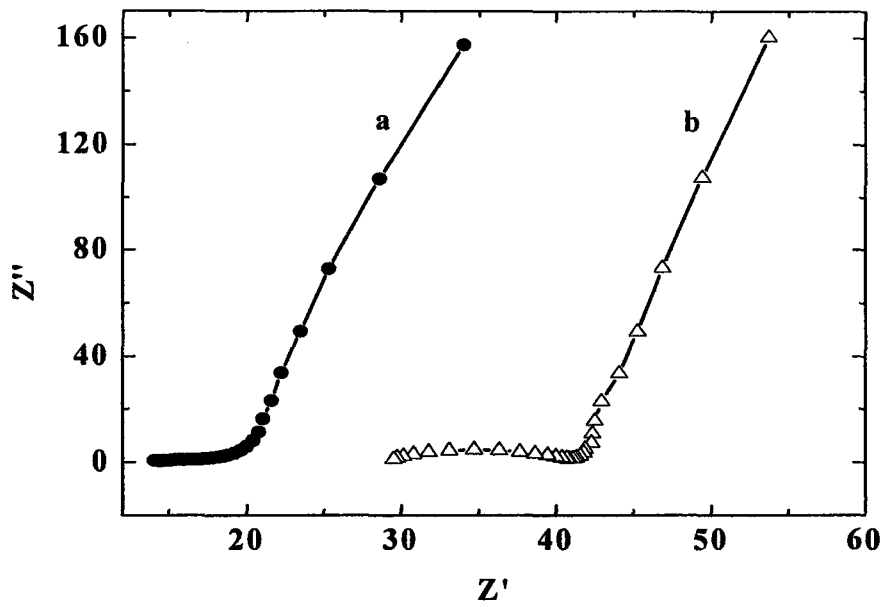

Figure 5-48 Impedance data with Z' as the real part and Z'' as the imaginary part of the 90 μg/cm^2 films prepared from 20 mM (a) $KMnO_4$ and (b) $NaMnO_4$ solution on stainless steel.

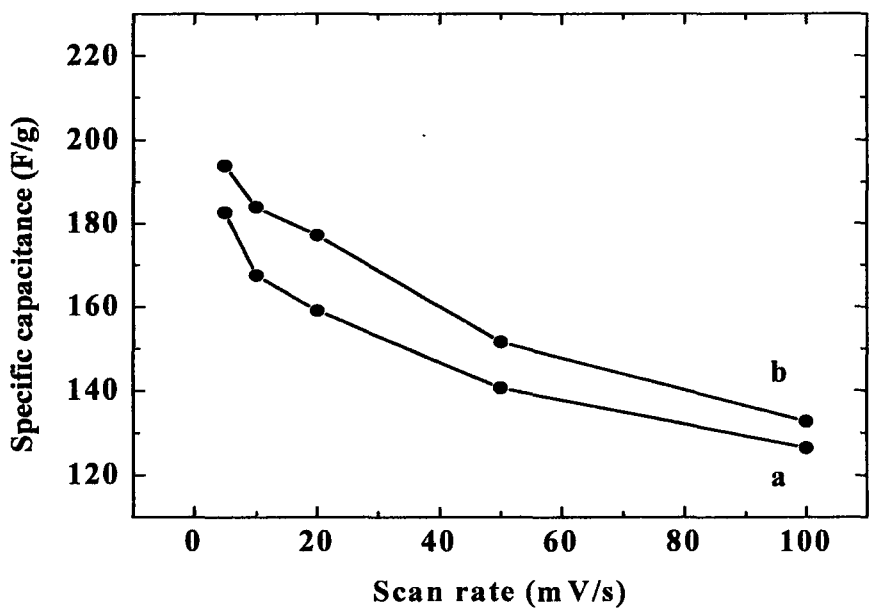

Figure 5-49 SC versus scan rate of the 90 μg/cm^2 films prepared on nickel from 20 mM (a) $KMnO_4$ and (b) $NaMnO_4$ aqueous solution.

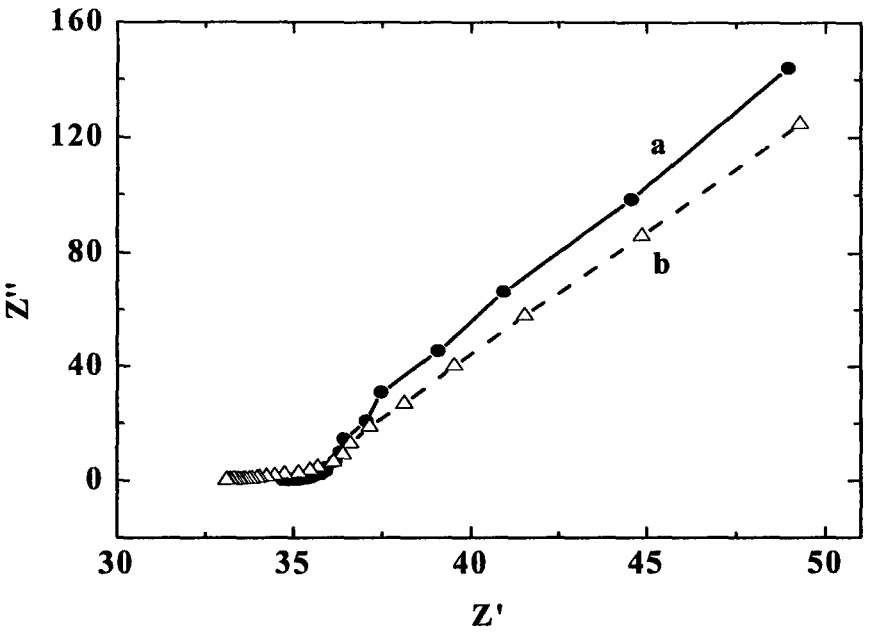

Figure 5-50 Impedance data with Z' as the real part and Z'' as the imaginary part of the 95 μg/cm^2 films prepared from 20 mM (a) $KMnO_4$ and (b) $NaMnO_4$ solution on Ni.

6 DISCUSSION

Deposition mechanism

Manganese oxide films were successfully prepared by cathodic deposition from $KMnO_4$ or $NaMnO_4$ aqueous solution on different substrates. The cathodic reduction of MnO_4^- species and precipitation of manganese oxide is in agreement with the Pourbaix diagram for Mn[76]. However, only limited information is available in the literature related to the complex chemistry of the reduction of $KMnO_4$. Kinetic pathway of reducing Mn^{7+} to Mn^{4+} depends on electrode potential, pH, concentration of MnO_4^- and other species in the solutions. In neutral aqueous solutions the following reaction can result in the reduction of MnO_4^- species[76]:

$$MnO_4^- + 2\,H_2O + 3\,e^- \rightarrow MnO_2 + 4\,OH^- \qquad (6\text{-}1)$$

However, the reduction of Mn^{7+} to lower oxidation states such as Mn^{3+} is also possible with the increasing negative potential[76].This reaction results of accumulation of MnO_2 particles at the electrode surface. Various forms of colloidal particles of oxides, hydroxides or peroxides are possible to compose the deposits[66]. It has been reported that the formation of a deposit is caused by flocculation introduced by the electrolyte[1,77]. The coagulation of colloidal particles could be enhanced by the electric field and electrohydrodynamic flows, resulting from the cathodic reactions[78-80]. Moreover, particles coagulation could also be enhanced by coulombic attraction resulting from ion correlation and depletion forces[78-80].

For both the deposition precursor, almost linear relationship was obtained between the deposit weight and deposition time. Higher deposition yield was obtained using deposition precursor with lower concentration compared to that of higher concentration. It is suggested that the deposition process includes the diffusion of anionic MnO_4^- species towards the cathode and electrosynthesis of manganese oxide nanoparticles in reaction (14). The difference in the deposition yield in deposition precursor with different concentrations (Figure 5-25 and Figure 5-33) can be attributed to various factors, such as changes in diffusion-electromigration kinetics, surface pH, and kinetics of other cathodic reactions[66,81], which can reduce the efficiency of manganese oxide formation. Moreover, the experimental data indicated that the composition and microstructure of the deposits depend on concentration of the deposition precursor.

Charge and discharge mechanism

The mechanism of charge storage in manganese oxides is based on the adsorption of ions on the oxide surface. Both the charge-transfer reaction at the electrode and electrolyte interface as well as the metal or hydrogen ion diffusion in the electrode are important in terms of the charge and discharging process for supercapacitors. Recent studies showed that the pseudocapacitance of hydrous a-$MnO_2 \cdot nH_2O$ is attributed to reversible redox transitions involving exchange of protons and/or cations with the electrolyte[20] :

$$MnO_{\alpha}(OH)_{\beta} + \delta H^{+} + \delta e^{-} \leftrightarrow MnO_{\alpha-\delta}(OH)_{\beta+\delta} \quad (6\text{-}2)$$

where $MnO_{\alpha}(OH)_{\beta}$ and $MnO_{\alpha-\delta}(OH)_{\beta+\delta}$ indicate interfacial a-$MnO_2 \cdot nH_2O$ at high and low oxidation states, respectively. Similar charging mechanism can be proposed for the hydrous manganese oxide films obtained in this work.

Effect of film thickness and scan rate

It was observed that thinner manganese oxide films possess higher specific capacitance values. This can be explained by the considerable lower resistivity for electron conduction of thinner films across the film onto the current collector. Also thinner films provide a shorter diffusion path length, with enhanced proton diffusion kinetics into and out of bulk materials[21,82]. Moreover, it is well known that the Faradaic reaction in a supercapacitor is limited to the surface layer of the electrode. As the film thickness increases, the content of active materials compared to the total sample weight decreases which results in lower capacitance value.

The maximum capacitance was obtained at the lowest scan rate because the ions have the time to reach the electrode surface which is hidden deep in the pores. As the scan rate increases, the ions can not reach the depth of the electrode pores anymore resulting in lower capacitance. To improve the ion dynamic the manufactures try to optimize the ion access to the pores with particular activation process[83].

Effect of heat treatment

The XRD data of films prepared from either $KMnO_4$ or $NaMnO_4$ aqueous solution exhibited poorly crystalline or amorphous structure at room temperature which is beneficial for dilation of MnO_2 lattice during protonation thereby enhancing the integrity and stability of these films.

The films prepared from $KMnO_4$ solution showed a rancieite structure after heat treatment at 200°C which has the hexagonal structure with a general formula $A_xMnO_{2+y}(H_2O)_z$ where A = K, Li, Ca or other cations[84]. The peak broadening could be related to the small particle size.

The films deposited from $NaMnO_4$ solution demonstrated a birnessite structure at low temperature which is a layered structure with alternately stacked sheets of MnO_6 octahedra linked through oxygen atoms and the water molecules occupy the interlayers[85] (Figure 6-1(a)). The interlayer spacing of this layered type manganese oxide material is nearly 7 Å. The water molecules at the interlayers can be easily desorbed by heat treatment forming dehydrated birnessite at 300°C. Further heat treatment resulted in the formation of cryptomelane-type manganese oxides which consisted of (2×2) matrices of tunnel structures with pore size of 4.6Å with a general composition of $A_{0.8\text{-}1.5}Mn_8O_{16}$ where A = K, Na, Ca or other cations[85] (Figure 6-1(b)). Inside the tunnel structure of manganese oxide materials, oxygen or potassium ions are present as exchangeable cations which are beneficial for conductivity and energy

storage. The capacitance of the different materials depends strongly on the crystalline structure, especially when the size of the tunnels limits the intercalation of cations[85].

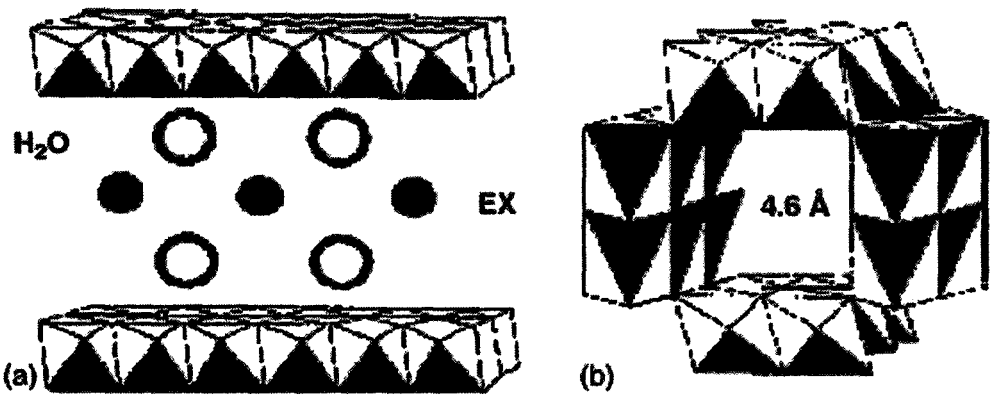

Figure 6-1 (a) Birnessite (Ex = K, Na, etc.) and (b) Cryptomelane type manganese oxide

The thermogravimetric behavior of the films deposited from different deposition precursors was investigated and the results showed weight loss by heating up to 200°C in air which can be attributed to the successive removal of both surface and structural water from the solid phase. MnO_2 undergoes rapid decomposition to form Mn_2O_3 at around 530°C and then be further reduced to Mn_3O_4 at 900°C. It has been reported that only a small portion of water in the electrodeposited manganese oxide films would be volatile at 120°C, while an effective portion of water can be absorbed up to 350°C in a relatively smooth manner[85].

Water content in manganese oxide is believed to play an important role in the electrochemical reactivity and thermodynamic stability of various phases of MnO_2 due to the variation in electrical conductivity and electrode potential caused by the

difference in crystal lattice[85, 86]. The hydrates can result in increase of the pseudocapacitance and the improvement of reversibility of the redox reaction as they provide the kinetically facile sites for the charge-transfer reaction and cation diffusion[1, 87, 88]. The charge-transfer resistance is also influenced by the oxidation states of manganese for the dehydrated electrode since the oxidation states are associated with the orbitals of Mn-cation available for the electron transfer[89]. Both the amount of hydrates and the oxidation states of manganese in the electrode can be effectively controlled by heat treatment temperature[90]. It has been reported that as the amount of hydrates decreases after heat treatment, the electrochemical active region becomes markedly narrower within the electrode specimen because less hopping sites are provided for the cation diffusion in the electrode. The reduced diffusion depth will result in lower capacitance value[88]. Higher electronic conductivity was obtained with increasing oxidation states of manganese due to the reduced activation energy. Overall, a lower capacitance value was expected after heat treatment. However, this reduction may be compensated by the increase in SC resulted from weight loss. Therefore, no significant change was obtained for the films after heat treatment in our work.

The effect of heat treatment in charge and discharge mechanism for amorphous manganese oxide electrode also has been investigated by Chun et al. It was proposed that the charging and discharging is purely limited by cation diffusion for electrode with the most hydrates. A transition occurs from pure diffusion control to a mixed

diffusion and charge-transfer reaction control when the amount of hydrates decreases after heat treatment within the range of 50-150°C. Then the charge-transfer reaction at the interface becomes predominant for the dehydrated electrodes heated at 200-400°C[88].

Impedance spectroscopy

Conductivity is one of the most important factors affecting the performance of electrochemical supercapacitors. Electrochemical impedance spectroscopy (EIS) is a typical analytical tool for investigation of electrical conductivity. For an ideal capacitor, the Nyquist plot would show a vertical line only coinciding with the vertical axis with the real part of Z being 0. For an ideal capacitor connected in series with a resistor (with resistance R), the vertical line in the Nyquist plot is shifted on the vertical axis by the amount of R. The equivalent RC circuit for an ideal capacitor can be described as below.

Circuit 1

For which, $Z = R + 1/j\omega C = R - j/\omega C$

As $\omega \to \infty$, $Z \to R$

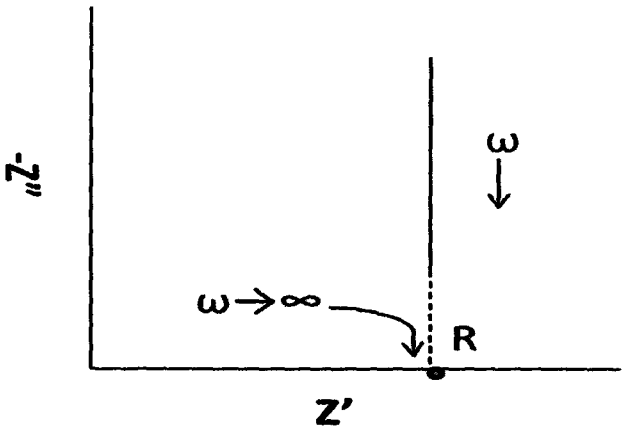

Figure 6-2 Complex-plane impedance plot for the series RC circuit 1 with Z' as the real part and Z'' as the imaginary part of impedance

The equivalent circuit for a pseudocapacitance has been shown earlier in Figure 5-11. The corresponding impedance curve intersects the real axis (ImZ=0) at about R_S towards high frequencies. At such high frequencies, the supercapacitor behaves almost like a simple resistor. For low frequencies, the spectrum approaches a vertical line with a real part equals to the sum of R_S and R_F as shown in Figure 6-3.

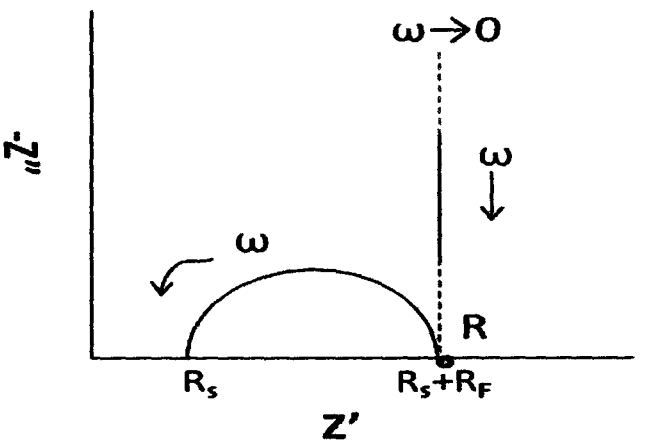

Figure 6-3 Complex-plane impedance plots for a Faradaic pseudocapacitance with no desorption resistance with Z' as the real part and Z'' as the imaginary part of impedance.

In practical, the charge and discharge process always involves Faradaic charge transfer resulted from interfacial redox reactions of impurities or surface functionalities at the electrode surfaces. Hence the kinetic representation of frequency-response behavior is important in interpreting the impedance spectroscopy of various types of electrochemical capacitors that do not behave in an ideally polarizable way. Therefore, the impedance involving ion diffusion is introduced as 'Warburg impedance element', represented by the symbol W. for a simple charge transfer reaction under diffusion control; the following equivalent circuit represents the impedance behavior. The as-prepared films in our work demonstrated similar behavior as the films in Figure 6-4 indicating the involvement of diffusion control ion exchange process during charge and discharge.

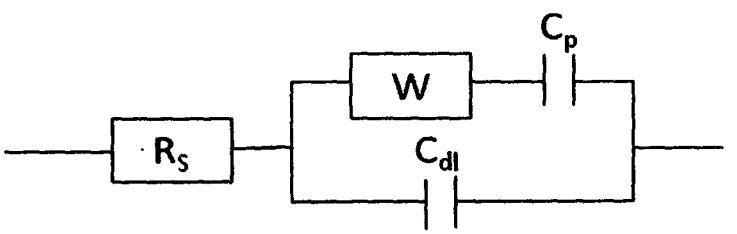

Circuit 2

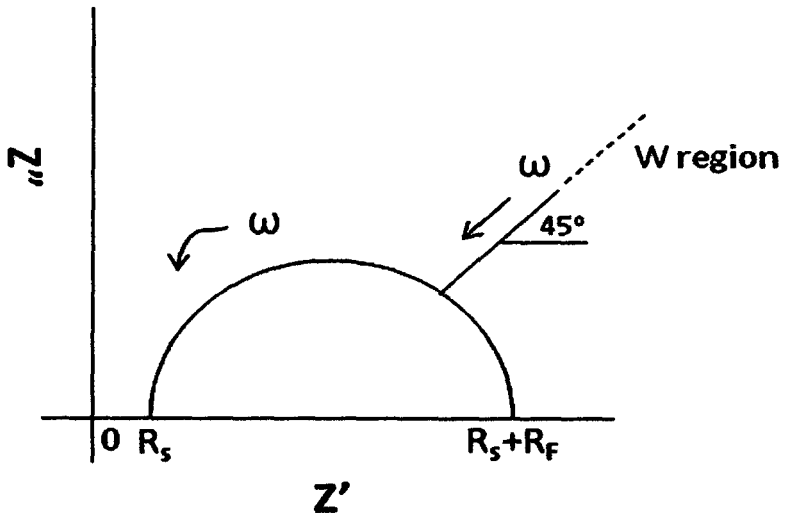

Figure 6-4 Complex-plane impedance plot for a Faradaic process involving transition to diffusion control at low frequency, ω, associated with the presence of the Warburg impedance element, W, exhibiting a 45° phase angle.

Effect of substrates

The effect of substrates was investigated by studying the performance of manganese oxide films deposited on stainless steel and nickel foil. Mismatch in thermal expansion coefficient can lead to poor adhesion of the deposited films and current collectors after heat treatment. Also the contact resistance at the interface between current collectors and electro-active materials plays an important role in determining the capacitive performance of the electrodes. Both the mechanical properties and the capacitive behavior can be improved by choosing the suitable substrates for metal oxide films. Favorable adhesion, good interface behavior between current collector and active materials, as well as the extra pseudo-capacitance has been obtained on graphite electrodes compared to nickel foils[91]. In our study, to compare the capacitive

behaviors of the resulting MnO_2 films on different substrates, the MnO_2 films from corresponding deposition precursors with identical deposit weight were evaluated by CV running in 0.1 M Na_2SO_4 solution. Higher capacitance values and more ideal CV windows were observed on nickel substrates compared to stainless steel foil. To further confirm the advantage of nickel over stainless steel foil, electrochemical impedance analysis was performed. Higher conductivity was obtained on nickel foil demonstrating better contact between the substrates and MnO_2 films.

Effect of electrolyte

In electrochemical supercapacitors, the capacitance arises from the intercalation of alkali ions into the electrode materials causing redox transitions. Conductivity and mobility of the alkali ions may be the determining factor for behavior in different electrolytes. Aqueous electrolyte was utilized due to its advantage in view of power because it can provide higher ion conductivity than a non-aqueous electrolyte. The parameters including ionic radius, radius of water of hydration, free energy formation of water of hydration and conductivity of different ions are critical to the performance of a supercapacitor. Na_2SO_4 solution was chosen due to the small ionic size of sodium ions. However, in aqueous electrolyte, the radius of hydration sphere also plays an important role. Therefore, similar capacitance values of the deposited films in K_2SO_4 and Na_2SO_4 solution were obtained since potassium ions possess smaller hydration sphere and higher conductivity as reported in Table 1[28]. Wen et al. has obtained

similar results that the capacitance of manganese oxide electrode do not change by changing the cation from K^+ to Na^+ or Li^+ ion[92, 93]. The concentration of the alkaline ions is the only important factor for determining the capacitance of the electrodes. It has also been reported that the charge storage mechanism of the MnO_2 electrode involves the redox reactions through both the proton exchange, $MnO_2 + \delta H^+ + \delta e^- \leftrightarrow MnO_{2-\delta}(OH)_\delta$ and the K^+ exchange $MnO_2 + \delta H^+ + \delta e^- \leftrightarrow MnO_{2-\delta}(OK)_\delta$.

Table 1 Crystal radius, radius of hydration sphere, free energy of hydration, conductivity of alkali ions.

Alkali ion	Crystal radius (Å)	Radius of hydration sphere (Å)	Gibbs energy (kcal/mol)	Conductivity (cm2/Ωmol)
Na^+	0.95	3.58	162.3	50.1
K^+	1.33	3.31	179.9	73.5

Effect of deposition precursor

The influence of deposition precursor on the deposition rate of hydrous manganese oxide in amorphous form was investigated by Chen et at[65]. Higher deposition rate at lower potentials was obtained using $Mn(CH_3COO)_2 \cdot 4H_2O$. However, the capacitive characteristics of α-$MnO_2 \cdot nH_2O$ were found to be independent of precursors as long as the mean oxidation state of Mn remained the same. In our work, different crystal structures were obtained for the films prepared from different deposition precursors. The films prepared from $KMnO_4$ solution on stainless steel showed higher

capacitance which can be attributed to its much higher conductivity compared to the films deposited from $NaMnO_4$ solution (Figure 5-48). For nickel substrate, better capacitive behavior was obtained on the films prepared from $NaMnO_4$ which also can be explained as the corresponding lower resistance of the films. Also the porous surface morphology with higher surface area may be responsible for higher capacitance value compared to the films deposited from $KMnO_4$ solution. From the above, it can be concluded that conductivity of the films plays a very important role in determining the capacitive performance of the electrodes.

7 CONCLUSIONS

Cathodic electrosynthesis has been utilized for the fabrication of manganese oxide films from the $KMnO_4$ and $NaMnO_4$ solutions. The results of linear sweep voltammetry and QCM studies indicate that cathodic reduction of MnO_4^- resulted in the formation of manganese oxide films. The deposition yield can be controlled by variation of deposition time at a constant current density. Higher deposition rate was obtained in the deposition solution with higher concentration.

For the films prepared from $KMnO_4$ solution, the results of XRD, TGA/DTA and EDX indicate the formation of rancieite-type manganese oxide films $K_xMnO_{2+y}(H_2O)_z$ ($x=0.35\pm0.04$). SEM investigations showed the formation of nanostructured porous films with typical pore size of about 100-200 nm. Heat treatment resulted in reduced porosity and improved crystallinity of the films. The rancieite-type manganese oxide films electrochemically tested in the 0.1 M Na_2SO_4 solutions showed the pseudocapacitive behavior in a potential window of 0-1.0V versus SCE with good stability up to 1000 cycles. The highest specific capacitance of ~ 353 F/g was obtained for 45 $\mu g/cm^2$ film at a scan rate of 2 mV/s. The capacitance decreased with increasing scan rate and film thickness. No significant effect was obtained by using different electrolyte of Na_2SO_4 and K_2SO_4 aqueous solution. The deposited films exhibited slightly higher capacitance after heat treatment due to

dehydration. Better capacitive behavior was observed on nickel substrates compared to stainless steel foil.

For the films prepared from $NaMnO_4$ solution, the results of XRD, TGA/DTA and EDS indicate that the film composition can be expressed as $Na_xMnO_{2+y}(H_2O)_z$ with $x=0.24\pm0.002$ and $x=0.14\pm0.001$ for the films prepared from 20 mM and 100 mM $NaMnO_4$ solution respectively. The deposition rate, composition and microstructure of the deposits depend on the concentration of $NaMnO_4$ in the solutions used for electrosynthesis. Electrosynthesis from 0.02 M $NaMnO_4$ solutions resulted in the formation of crystalline films with a birnessite structure. Amorphous films were obtained using 0.1 M $NaMnO_4$ solutions. The formation of a cryptomelane phase was observed after annealing at temperatures exceeding 400°C. The films obtained from the 0.1 M $NaMnO_4$ solutions showed low porosity and exhibited cracking, attributed to drying shrinkage. Crack-free porous films with typical pore size of about 100-200 nm were obtained from the 0.02 M $NaMnO_4$ solutions. The microstructure of the films obtained from the 0.02 M $NaMnO_4$ solutions changed from relatively dense to porous with increasing film thickness. The films electrochemically tested in the 0.1 M Na_2SO_4 solutions showed the pseudocapacitive behavior in a potential window of 0-1.0V versus SCE. The highest specific capacitance of ~ 250 Fg^{-1} was obtained for a 90 μgcm^{-2} sample at a scan rate of 2 mVs^{-1}. The capacitance decreased with increasing scan rate. Better capacitive behavior was obtained on stainless steel from $KMnO_4$ aqueous solution due to its high conductivity, while in contrast higher

capacitance was obtained for the films deposited from $NaMnO_4$ solution on nickel. The films prepared by cathodic electrosynthesis from both deposition precursors can be considered as possible electrode materials for ES. Obtained results paved the way for the fabrication of advanced electrodes for electrochemical supercapacitors.

8 FUTURE WORK

Low conductivity is the main disadvantage of the as-prepared manganese oxide films for the application of electrochemical supercapacitors. Improvement of conductivity can be carried out for further investigation including possible co-deposition such as carbon nanotube or other metals. The capacitive behavior of the films deposited on substrates with higher surface area, such as nickel foam and nickel plaques, may also be interested to investigate.

9 REFERENCES

1. B.E. Conway, *'Electrochemical Supercapacitors – Scientific Fundamentals and Technological Applications'*. 1999: Kluwer, New York.
2. R. Kotz and M. Carlen, *'Principles and applications of electrochemical capacitors'*, Electrochimica Acta. **45** (2000): p2483.
3. H.E. Becker, U.S., Patent 2 800 616, General Electric, (1957).
4. D.I. Boss, U.S., Patent 3 536 963, Standard Oil, SOHIO, (1970).
5. S. Hadzi-Jordanov, H. Angerstein-Kozlowska, M. Vukovic, and B.E. Conway, *'Reversibility and growth behavior of surface oxide films at ruthenium electrodes'*, Journal of the Electrochemical Society. **125** (1978): p1471.
6. S. Trasatti and G. Buzzanca, *'Ruthenium dioxide: A new interesting electrode material. Solid state structure and electrochemical behaviour'*, Journal of Electroanalytical Chemistry. **29** (1971): pA1.
7. S. Hadzi-Jordanov, H. Angerstein-Kozlowska, and B.E. Conway, *'Surface oxidation and H deposition at ruthenium electrodes: Resolution of component processes in potential-sweep experiments'*, Journal of Electroanalytical Chemistry. **60** (1975): p359.
8. D. Galizzioli, F. Tantardini, and S. Trasatti, *'Ruthenium dioxide: A new electrode material em dash 2. non-stoichiometry and energetics of electrode reactions in acid solutions,,*Journal of Applied Electrochemistry. **5** (1975): p203.

9. R.J. Brodd, K.R. Bullock, R.A. Leising, R.L. Middaugh, J.R. Miller, and E. Takeuchi, *'Batteries, 1977 to 2002'*, Journal of the Electrochemical Society. **151** (2004): pK1.

10. B.E.Conway, J.O.M. Bockris, and I.A.Ammar, *'The dielectric constant of the solution in the diffuse and Helmholtz double layers at a charged interface in aqueous solution'*, Transactions of the Faraday Society, (1951): p756.

11. A.F.Burke. and T.C.Murphy. *'Materials for Electrochemical Energy Storage and Conversion - Batteries, Capacitors and Fuel Cells'*. in *Materials Research Society Symposium*. 1995. San Francisco,CA.

12. H. Probstle, C. Schmitt, and J. Fricke, *'Button cell supercapacitors with monolithic carbon aerogels'*, Journal of Power Sources. **105** (2002): p189.

13. A.F. Burke and T.C. Murphy. *'Materials for Electrochemical Energy Storage and Conversion – Batteries, Capacitors and Fuel Cells: Symposium '*. 1995. San Francisco, CA.

14. M.F. Rose, In *Proceedings of 33rd International Power Sources Symposium*. 1988. Pennington, NJ.

15. Biniak.S, Swiatkowski.A., P. M, and R.L. R., *'Chemistry and Physics of Carbon'*. Vol. 27. 2001, New York: Marcel Dekker. 125.

16. M. Endo, T. Maeda, T. Takeda, Y.J. Kim, K. Koshiba, H. Hara, and M.S. Dresselhaus, *'Capacitance and pore-size distribution in aqueous and nonaqueous electrolytes using various activated carbon electrodes'*, Journal of the Electrochemical Society. **148** (2001): pA910.

17. K.S.W. Sing, D.H. Everett, R.A.W. Haul, L. Moscou, R.A. Pierotti, J. Rouquerol, and T. Siemieniewska, *'Reporting physisorption data for gas/solid systems with special reference to the determination of surface area and porosity'*, Pure Applied Chemistry. **57** (1985): p603.

18. A.G. Pandolfo and A.F. Hollenkamp, *'Carbon properties and their role in supercapacitors'*, Journal of Power Sources. **157** (2006): p11.

19. M.P. Owen, G.A. Lawrance, and S.W. Donne, *'An electrochemical quartz crystal microbalance study into the deposition of manganese dioxide'*, Electrochimica Acta. **52** (2007): p4630.

20. M. Toupin, T. Brousse, and D. Belanger, *'Charge Storage Mechanism of MnO_2 Electrode Used in Aqueous Electrochemical Capacitor'*, Chem. Mater. **16** (2004): p3184.

21. P. Sub-Cem, M.A. Anderson, and T.W. Chapman, *'Novel electrode materials for thin-film ultracapacitors: comparison of electrochemical properties of sol-gel-derived and electrodeposited manganese dioxide'*, Journal of the Electrochemical Society. **147** (2000): p444.

22. H.Y. Lee and J.B. Goodenough, *'Supercapacitor Behavior with KCl Electrolyte'*, Journal of Solid State Chemistry. **144** (1999): p220.

23. P. Ruetschi, *'Cation-Vacancy Model for MnO_2'*, Journal of The Electrochemical Society. **131** (1984): p2737.

24. L. Chih-Hsiang, N. Chiao-Lin, H. Hsien-Chun, and H. Chii-Shyang, *'Charging/discharging behavior of manganese oxide electrodes in aqueous*

electrolyte prepared by galvanostatic electrodeposition', Journal of the Ceramic Society of Japan. **115** (2007): p319.

25. B. Djurfors, J.N. Broughton, M.J. Brett, and D.G. Ivey, *'Production of capacitive films from Mn thin films: effects of current density and film thickness'*, Journal of Power Sources. **156** (2006): p741.

26. S.-F. Chin, S.-C. Pang, and M.A. Anderson, *'Material and Electrochemical Characterization of Tetrapropylammonium Manganese Oxide Thin Films as Novel Electrode Materials for Electrochemical Capacitors'*, Journal of The Electrochemical Society. **149** (2002): pA379.

27. Y.U. Jeong and A. Manthiram, *'Nanocrystalline manganese oxides for electrochemical capacitors with neutral electrolytes'*, Journal of the Electrochemical Society. **149** (2002): p1419.

28. R.N. Reddy and R.G. Reddy, *'Sol-gel MnO_2 as an electrode material for electrochemical capacitors'*, Journal of Power Sources. **124** (2003): p330.

29. H. Chi-Chang and T. Ta-Wang, *'Ideal capacitive behavior of hydrous manganese oxide prepared by anodic deposition'*, Electrochemistry Communications. **4** (2002): p105.

30. S. Trasatti and G. Lodi, *'Electrodes of conductive metallic oxides part A'*, ed. S. Trasatti. 1980, New York: Elsevier. 301.

31. D. Michell, D.A.J. Rand, and R. Woods, *'A study of ruthenium electrodes by cyclic voltammetry and X-ray emission spectroscopy'*, Journal of Electroanalytical Chemistry. **89** (1978): p11.

32. J.P. Zheng, P.J. Cygan, and T.R. Jow, *'Hydrous Ruthenium Oxide as an Electrode Material for Electrochemical Capacitors'*, Journal of The Electrochemical Society. **142** (1995): p2699.

33. I.D. Raistrick, *'The Electrochemistry of Semiconductors and Electronics-Process and Devices'*, ed. J. Mchardy and F. Luduig. 1992, Park Ridge: Noyes. 297.

34. J.P. Zheng, *'Ruthenium Oxide-Carbon Composite Electrodes for Electrochemical Capacitors'*, Electrochemical and Solid-State Letters. **2** (1999): p359.

35. K.-C. Liu and M.A. Anderson, *'Porous Nickel Oxide/Nickel Films for Electrochemical Capacitors'*, Journal of The Electrochemical Society. **143** (1996): p124.

36. V. Srinivasan and J.W. Weidner, *'Studies on the Capacitance of Nickel Oxide Films: Effect of Heating Temperature and Electrolyte Concentration'*, Journal of The Electrochemical Society. **147** (2000): p880.

37. E.E. Kalu, T.T. Nwoga, V. Srinivasan, and J.W. Weidner, *'Cyclic voltammetric studies of the effects of time and temperature on the capacitance of electrochemically deposited nickel hydroxide'*, Journal of Power Sources. **92** (2001): p163.

38. K.-W. Nam and K.-B. Kim, *'A Study of the Preparation of NiO_x Electrode via Electrochemical Route for Supercapacitor Applications and Their Charge Storage Mechanism'*, Journal of The Electrochemical Society. **149** (2002): pA346.

39. Y. Sun, S.R. Wilson, and D.I. Schuster, *'High Dissolution and Strong Light Emission of Carbon Nanotubes in Aromatic Amine Solvents'*, J. Am. Chem. Soc. **123** (2001): p5348.

40. J. Deng, X. Ding, W. Zhang, Y. Peng, J. Wang, X. Long, P. Li, and A.S.C. Chan, *'Carbon nanotube-polyaniline hybrid materials'*, European Polymer Journal. **38** (2002): p2497.

41. K.H. An, K.K. Jeon, J.K. Heo, S.C. Lim, D.J. Bae, and Y.H. Lee, *'High-Capacitance Supercapacitor Using a Nanocomposite Electrode of Single-Walled Carbon Nanotube and Polypyrrole'*, Journal of The Electrochemical Society. **149** (2002): pA1058.

42. Q.W. Li, H. Yan, Y. Cheng, J. Zhang, and Z.F. Liu, *'A scalable CVD synthesis of high-purity single-walled carbon nanotubes with porous MgO as support material'*, Journal of Materials Chemistry. **12** (2002): p1179.

43. Y.-k. Zhou, B.-l. He, W.-j. Zhou, J. Huang, X.-h. Li, B. Wu, and H.-l. Li, *'Electrochemical capacitance of well-coated single-walled carbon nanotube with polyaniline composites'*, Electrochimica Acta. **49** (2004): p257.

44. Y.-k. Zhou, B.-l. He, W.-j. Zhou, and H.-l. Li, *'Preparation and Electrochemistry of SWNT/PANI Composite Films for Electrochemical Capacitors'*, Journal of The Electrochemical Society. **151** (2004): pA1052.

45. M. Mastragostino, C. Arbizzani, and F. Soavi, *'Conducting polymers as electrode materials in supercapacitors'*, Solid State Ionics. **148** (2002): p493.

46. V. Gupta and N. Miura, *'High performance electrochemical supercapacitor from electrochemically synthesized nanostructured polyaniline'*, Materials Letters. **60** (2006): p1466.

47. A. Malinauskas, J. Malinauskiene, and A. Ramanavicius, *'Conducting polymer-based nanostructurized materials: electrochemical aspects'*, Nanotechnology. **16** (2005): pR51.

48. V. Gupta and N. Miura, *'Large-area network of polyaniline nanowires prepared by potentiostatic deposition process'*, Electrochemistry Communications. **7** (2005): p995.

49. K. Jurewicz, S. Delpeux, V. Bertagna, F. Beguin, and E. Frackowiak, *'Supercapacitors from nanotubes/polypyrrole composites'*, Chemical Physics Letters. **347** (2001): p36.

50. H. Qiu, M. Wan, B. Matthews, and L. Dai, *'Conducting Polyaniline Nanotubes by Template-Free Polymerization'*, Macromolecules. **34** (2001): p675.

51. J. Huang and R.B. Kaner, *'A General Chemical Route to Polyaniline Nanofibers'*, J. Am. Chem. Soc. **126** (2004): p851.

52. K.R. Prasad and N. Miura, *'Potentiodynamically deposited nanostructured manganese dioxide as electrode material for electrochemical redox supercapacitors'*, Journal of Power Sources. **135** (2004): p354.

53. T. Brousse and D. Belanger, *'A Hybrid Fe_3O_4-MnO_2 Capacitor in Mild Aqueous Electrolyte'*, Electrochemical and Solid-State Letters. **6** (2003): pA244.

54. M.S. Michael and S.R.S. Prabaharan, *'High voltage electrochemical double layer capacitors using conductive carbons as additives'*, Journal of Power Sources. **136** (2004): p250.

55. M. Galinski, A. Lewandowski, and I. Stepniak, *'Ionic liquids as electrolytes'*, Electrochimica Acta. **51** (2006): p5567.

56. J. Robinson and R.A. Osteryoung, *'Electrochemical and Spectroscopic Study of Some Aromatic-Hydrocarbons in the Room-Temperature Molten-Salt System Aluminum Chloride-N-Butylpyridinium Chloride'*, Journal of the American Chemical Society. **101** (1979): p323.

57. A. Lewandowski and M. Galinski, *'Carbon-ionic liquid double-layer capacitors'*, Journal of Physics and Chemistry of Solids. **65** (2004): p281.

58. A. Lewandowski and A. Swiderska, *'Electrochemical capacitors with polymer electrolytes based on ionic liquids'*, Solid State Ionics. **161** (2003): p243.

59. A.F. Burke and M. Miller. in *Proceedings of the 8th international seminar on double layer capacitors and similarly energy storage devices*. 1998. Florida Educational Seminar.

60. S. Bach, M. Henry, N. Baffier, and J. Livage, *'Sol-gel synthesis of manganese oxides'*, Journal of Solid State Chemistry. **88** (1990): p325.

61. H. Kim and B.N. Popov, *'Characterization of hydrous ruthenium oxide/carbon nanocomposite supercapacitors prepared by a colloidal method'*, Journal of Power Sources. **104** (2002): p52.

62. K.-W. Nam and K.-B. Kim, *'Manganese Oxide Film Electrodes Prepared by Electrostatic Spray Deposition for Electrochemical Capacitors'*, Journal of The Electrochemical Society. **153** (2006): pA81.

63. H.Y. Lee, S.W. Kim, and H.Y. Lee, *'Expansion of Active Site Area and Improvement of Kinetic Reversibility in Electrochemical Pseudocapacitor Electrode'*, Electrochemical and Solid-State Letters. **4** (2001): pA19.

64. C.-C. Hu and T.-W. Tsou, *'Ideal capacitive behavior of hydrous manganese oxide prepared by anodic deposition'*, Electrochemistry Communications. **4** (2002): p105.

65. Y.S. Chen, C.C. Hu, and Y.T. Wu, *'Capacitive and textural characteristics of manganese oxide prepared by anodic deposition: effects of manganese precursors and oxide thickness'*, Journal of Solid State Electrochemistry. **8** (2004): p467.

66. I. Zhitomirsky, *'Cathodic electrodeposition of ceramic and organoceramic materials. Fundamental aspects'*, Advances in Colloid and Interface Science. **97** (2002): p279.

67. I. Zhitomirsky, *'Cathodic electrosynthesis of titanium and ruthenium oxides'*, Materials Letters. **33** (1998): p305.

68. I. Zhitomirsky, *'Cathodic electrosynthesis of titania films and powders'*, Nanostructured Materials. **8** (1997): p521.

69. B.D. Vogt, E.K. Lin, W.L. Wu, and C.C. White, *'Effect of film thickness on the validity of the Sauerbrey equation for hydrated polyelectrolyte films'*, Journal of Physical Chemistry B. **108** (2004): p12685.

70. A.P. Malloy, G.J. Browning, and S.W. Donne, *'Surface characterization of heat-treated electrolytic manganese dioxide'*, Journal of Colloid and Interface Science. **285** (2005): p653.

71. J. Moon, M. Awano, H. Takagi, and Y. Fujishiro, *'Synthesis of nanocrystalline manganese oxide powders: Influence of hydrogen peroxide on particle characteristics'*, Journal of Materials Research. **14** (1999): p4594.

72. S. Devaraj and N. Munichandraiah, *'High capacitance of electrodeposited MnO_2 by the effect of a surface-active agent'*, Electrochemical and Solid State Letters. **8** (2005): pA373.

73. J.-K. Chang and W.-T. Tsai, *'Material Characterization and Electrochemical Performance of Hydrous Manganese Oxide Electrodes for Use in Electrochemical Pseudocapacitors'*, Journal of The Electrochemical Society. **150** (2003): pA1333.

74. J.N. Broughton and M.J. Brett, *'Variations in MnO_2 electrodeposition for electrochemical capacitors'*, Electrochimica Acta. **50** (2005): p4814.

75. R. Chaim, I. Silberman, and L. Galor, *'Electrolytic ZrO_2 Coatings.2. Microstructural Aspects'*, Journal of the Electrochemical Society. **138** (1991): p1942.

76. A. Moussard, J. Brenet, F. Jolas, M. Pourbaix, and J. Van Muylder, *'Atlas of electrochemical equilibria in aqueous solutions'*, ed. M. Pourbaix. 1974, Oxford: Pergamon Press. 286.

77. I. Zhitomirsky, *'New developments in electrolytic deposition of ceramic films'*, American Ceramic Society Bulletin. **79** (2000): p57.

78. M.R. Bohmer, *'In Situ Observation of 2-Dimensional Clustering during Electrophoretic Deposition'*, Langmuir. **12** (1996): p5747.

79. M. Trau, D.A. Saville, and I.A. Aksay, *'Field-induced layering of colloidal crystals'*, Science. **272** (1996): p706.

80. I. Zhitomirsky and L. Gal-Or, *'Electrophoretic deposition of hydroxyapatite'*, Journal of Materials Science: Materials in Medicine. **8** (1997): p213.

81. L. Gal-Or, I. Silberman, and R. Chaim, *'Electrolytic ZrO_2 Coatings'*, Journal of The Electrochemical Society. **138** (1991): p1939.

82. J.H. Jiang and A. Kucernak, *'Electrochemical supercapacitor material based on manganese oxide: preparation and characterization'*, Electrochimica Acta. **47** (2002): p2381.

83. F. Rafik, H. Gualous, R. Gallay, A. Crausaz, and A. Berthon, *'Frequency, thermal and voltage supercapacitor characterization and modeling'*, Journal of Power Sources. **165** (2007): p928.

84. F. Leroux, D. Guyomard, and Y. Piffard, *'The 2D Rancieite-Type Manganic Acid and Its Alkali-Exchanged Derivatives.1. Chemical Characterization and Thermal-Behavior'*, Solid State Ionics. **80** (1995): p299.

85. R. Jothiramalingam, B. Viswanathan, and T.K. Varadarajan, *'Synthesis and structural characterization of copper incorporated manganese oxide OMS-2*

materials synthesized via potassium birnessite', Materials Chemistry and Physics. **100** (2006): p257.

86. A. Era, Z. Takehara, and S. Yoshizawa, *'Discharge mechanism of the manganese dioxide electrode'*, Electrochimica Acta. **12** (1967): p1199.

87. G.W. Jang, E.W. Tsai, and K. Rajeshwar, *'Charge Storage and Transport in Thermal Ruthenium Oxide Thin-Films - Insitu Detection of Local pH Changes and Asymmetries in Charge Discharge Cycles at the Oxide Aqueous-Electrolyte Interphase'*, Journal of Electroanalytical Chemistry. **263** (1989): p383.

88. M. Vukovic, T. Valla, and M. Milun, *'Electron spectroscopy characterization of an activated ruthenium electrode'*, Journal of Electroanalytical Chemistry. **356** (1993): p81.

89. S.E. Chun, S.I. Pyun, and G.J. Lee, *'A study on mechanism of charging/discharging at amorphous manganese oxide electrode in 0.1 M Na_2SO_4 solution'*, Electrochimica Acta. **51** (2006): p6479.

90. M. Chigane and M. Ishikawa, *'Manganese oxide thin film preparation by potentiostatic electrolyses and electrochromism'*, Journal of the Electrochemical Society. **147** (2000): p2246.

91. M. Wu, J. Gao, S. Zhang, and A. Chen, *'Comparative studies of nickel oxide films on different substrates for electrochemical supercapacitors'*, Journal of Power Sources. **159** (2006): p365.

92. S. Wen, J.W. Lee, I.H. Yeo, J. Park, and S. Mho, *'The role of cations of the electrolyte for the pseudocapacitive behavior of metal oxide electrodes, MnO_2 and RuO_2'*, Electrochimica Acta. **50** (2004): p849.

93. S. Wen, J.-W. Lee, I.-H. Yeo, J. Park, and S.-I. Mho, *'The role of cations of the electrolyte for the pseudocapacitive behavior of metal oxide electrodes, MnO_2 and RuO_2'*, Electrochimica Acta. **50** (2004): p849.